UNIVERSITY OF CALIFORNIA SAN DIEGO

SAN DIEGO STATE UNIVERSITY

Climate-Driven Coastal Morphodynamics along Southeast Queensland, Australia

A dissertation submitted in partial satisfaction of the
requirements for the degree Doctor of Philosophy

in

Geophysics

by

Joshua Terence Kelly

Committee in charge:

San Diego State University

Professor Allen Gontz, Chair
Professor Douglas Stow
Professor Isaac Ullah

University of California San Diego

Professor Falko Kuester
Professor David Sandwell
Professor James Shulmeister

2020

The Dissertation of Joshua Terence Kelly is approved, and it is acceptable in quality and form for publication on microfilm and electronically:

_____

_____

_____

_____

_____

_____

Chair

University of California San Diego

San Diego State University

2020

DEDICATION

To: My parents, Noel and Patricia, for their unwavering support throughout this journey and for instilling in me the values of hard work, commitment, and patience.

TABLE OF CONTENTS

LIST OF FIGURES

LIST OF TABLES

ACKNOWLEDGEMENTS

This dissertation would have been nonexistent if it weren't for the unyielding support of my advisor, Professor Allen Gontz. At the beginning, Allen showed me a great cartoon that illustrates "The Doctoral Journey", whereby the student's plan is to ride a bike on a flat surface from the start to finish line. The "Reality" panel shows that path being interrupted by various obstacles such as cliff faces, vast ocean expanses, and heavy forest. Replace those barriers with a cross country move to San Diego after the first year, squandered field campaign in Brazil due to Brazilian customs, and miles of red tape that had to be cut as the first transfer into the JDP program, and that cartoon is VERY representative of my PhD journey. I would not have made it to this point without Allen's willingness to argue on my behalf to university administrators, encouragement to pursue independent research topics, funding to attend a plethora of national and international conferences, and most importantly, mentoring on how to become a more productive and affable scientist and teacher.

I would also like to thank Professor Jamie Shulmeister for his generosity in hosting me in Australia and willingness to let me participate in his research group's field campaign on Fraser Island. Dr. Sarah McSweeney was also instrumental in the development of this dissertation and her willingness to participate in Zoom meetings at odd hours of the day to talk about wave climate and Matlab techniques was appreciated. Finally, I would like to thank all of the students and faculty members I have worked with at SDSU, Universidade Tiradentes, and UQ as well as Drake Singleton and Yuval Levy for their friendship and guidance.

Words cannot describe my gratitude to my wife, Megan, for her support, in many ways, throughout this journey. Intentional or not, our relationship flourished throughout the course of this dissertation; from becoming engaged during my first year, moving in together during the second, and getting married shortly before my advancement to candidacy, you were there every step (and hurdle) of the way. Your words of encouragement when I received discouraging news on a manuscript review, grant submission, and as of this writing, job applications, were always welcomed and immensely appreciated. I am so incredibly lucky to have had you by my side during this process and even more so for the lifelong journeys ahead of us.

Chapter 2, in full, is a reformatted version of the material as it appears in the *International Journal of Applied Earth Observation and Geoinformation*: Kelly, Joshua T. and Gontz, Allen. 2018. Using GPS-surveyed intertidal zones to determine the validity of shorelines automatically mapped by Landsat water indices. *International Journal of Applied Earth Observation and Geoinformation*. v. 65C, p. 92-104. Joshua Terence Kelly was the primary investigator and author of this paper.

Chapter 3, in full, is a reformatted version of the material as it appears in *Marine Geology*: Kelly, Joshua T., McSweeney, Sarah, Shulmeister, James, and Gontz, Allen. 2019. Bimodal climate control of shoreline change influenced by Interdecadal Pacific Oscillation variability along the Cooloola Sand Mass, Queensland, Australia. *Marine Geology*. v. 415C. Joshua Terence Kelly was the primary investigator and author of this paper.

Chapter 4, in full, is a reformatted version of the material as it currently appears ahead of press in the *Journal of Coastal Research*: Kelly, Joshua T. and Gontz, Allen. 2019. Rapid assessment of shoreline changes induced by Tropical Cyclone Oma using CubeSat imagery in southeast Queensland, Australia. Journal of Coastal Research. Joshua Terence Kelly was the primary investigator and author of this paper.

VITA

2020	Ph.D. in Geophysics, University of California San Diego and San Diego State University
2017	M.Sc. in Environmental Science, University of Massachusetts, Boston
2013	M.Sc. in Oceanography, University of Rhode Island
2011	B.Sc. in Geosciences, University of Rhode Island

PUBLICATIONS

Kelly, J. T. and Gontz, A. 2019. Rapid assessment of shoreline changes induced by Tropical Cyclone Oma using CubeSat imagery in southeast Queensland, Australia. *Journal of Coastal Research*. (in press)

Kelly, J. T., McSweeney, S., Shulmeister, J., Gontz, A. 2019. Bimodal climate control of shoreline change influenced by Interdecadal Pacific Oscillation variability along the Cooloola Sand Mass, Queensland, Australia. *Marine Geology*. v. 415C.

Blanton, C. M., Rockwell, T. K., Gontz, A., Kelly, J.T. 2020. Refining the spatial and temporal signatures of creep and co-seismic slip along the Southern San Andreas Fault using very high resolution SfM imagery, Coachella Valley, California. *Geomorphology*.

Kelly, J. T. and Gontz, A. 2018. Using GPS-surveyed intertidal zones to determine the validity of shorelines automatically mapped by Landsat water indices. *International Journal of Applied Earth Observation and Geoinformation*. v. 65C, p. 92-104.

Haneberg, W. C., Kelly, J. T., Graves, H. L., and Dan, G. 2015. A GIS-based decision-support approach to deepwater drilling-hazard maps. *The Leading Edge*. v. 34(4), p. 398-404.

Kelly, J. T., Carey, S., Croff-Bell, K. L., Roman, C., Rosi, M., Marani, M., and Pistolesi, M. 2014. Exploration of the 1891 Foerstner submarine vent site (Pantelleria, Italy): insights into the formation of basaltic balloons. *Bulletin of Volcanology*. v. 76, p. 844-862.

Carey, S., Croff-Bell, K. L., Rosi, M., Marani, M., Nomiku, E., Walker, S., Faure, K., and Kelly, J. T. 2012. New Frontiers in Ocean Exploration: The E/V Nautilus 2011 Field Season, Hydrothermal activity at submarine volcanoes of the Aeolian Arc, Tyrrhenian Sea. *Oceanography*, supplement edition volume 25(1), p. 32-33.

ABSTRACT OF THE DISSERTATION

Climate-Driven Coastal Morphodynamics along Southeast Queensland, Australia

by

Joshua Terence Kelly

Doctor of Philosophy in Geophysics

University of California San Diego, 2020
San Diego State University, 2020

Professor Allen Gontz, Chair

Understanding how shoreline positions change in response to the variability of multitemporal climate and weather phenomena is essential for predicting the impact of future climate extremes. This dissertation aims to provide the first quantitative assessment on the relative influence of climate phenomena operating in the southwest Pacific region, i.e. El Niño-Southern Oscillation, on coastal morphodynamics along the southeast Queensland coast on a yearly to decadal timescale. Morphodynamic changes occurring at the timescale of days are also assessed in response to Tropical Cyclone Oma striking the

region in February 2019. Previous attempts at directly correlating climate to natural shoreline evolution elsewhere were limited in their ability to observe the geomorphic changes as they relied on infrequent aerial photography, isolated beach profile data, or morphodynamic modeling results with no ground trothing. In an effort to capture intra-annual shoreline variability across large spatial scales (100's km), shorelines are mapped using historical Landsat imagery. The accuracy of shorelines mapped automatically using spectral water indices was assessed by comparison to two contemporaneous GPS-surveyed intertidal zones, which represents the true position of the shoreline interface, which were conducted in Brazil and Massachusetts. The Modified Normalized Difference Water Index was determined to be the best index for automated shoreline mapping based on its superior accuracy and repeatable threshold value. MNDWI was used to automatically map over 9,000 km of historical shoreline positions along Queensland using Google Earth Engine. Shoreline change curves were generated using the USGS Digital Shoreline Analysis System and corrected for tidal variations using in situ gauge data and seasonal intertidal widths estimated from equilibrium beach profiles. Cross-correlations between the shoreline dataset and the various climate indices were calculated using a 20 month maximum lag. Correlations suggest a bimodal climate control on shoreline change whereby El Niño-Southern Oscillation has the largest influence during negative Interdecadal Pacific Oscillation with the Subtropical Ridge becoming dominant during positive IPO. As observed using revolutionary PlanetScope satellite imagery, longshore transport along SE Queensland turned northwards in response to a significant anti-clockwise rotation of

incident wave direction during Oma with erosion peaking at 41 m along the Sunshine Coast.

Chapter 1

Introduction

It's well understood that global sea-level rise will have significant ramifications for global populations, ecosystems, and infrastructure. If the upper-end of warming scenarios is realized by 2050 (4º C), sea-level rise caused by enhanced ocean thermal expansion and mountain glacier melt could potentially displace up to 187 million people and cost over $1 trillion USD (Hallegate et al., 2013; Nicholls et al., 2008). Retrogradation, or landward movement, of shoreline positions is an obvious and expected risk of sea-level rise for coastal regions around the world, regardless of shoreline geometry and morphology (Reimann et al., 2018; Sahin et al., 2019; Thorne et al., 2018). In addition to the risk posed by sea-level rise, variations in wave climate are expected to be a significant influence on future shoreline modification of exposed, sandy coastlines in the coming decades (Coelho et al., 2009; Hemer et al., 2012; Slott et al., 2006). Changes in the wave climate, such as significant wave heights and incident wave directions, can change the rate and direction of longshore transport and thus, realign sandy shoreline positions (Thom et al., 2018). Much of Australia's eastern shoreline is dominated by unconsolidated sandy beaches, muddy shores, and semi-lithified rock. These erodible coastal landforms are expected to be relatively resilient in the face of sea-level rise due to their capacity to accrete in the wake of erosion events but will be particularly sensitive to wave climate changes (Thom et al., 2018).

Understanding this coastal morphodynamic relationship, it's plausible that the drivers of wave climate variability in southeastern Australia are, in turn, influencing

shoreline position variability. The coupling between atmospheric and wave climate has been extensively studied in this region and it's generally accepted that the regional wave climate of southeast Queensland is driven by variability in the El Niño-Southern Oscillation (ENSO, McSweeney and Shulmeister, 2018; Mortlock and Goodwin, 2016; Ranasinghe et al., 2004). During negative Southern Oscillation Index (SOI, index for gauging El Niño/La Niña strength) phases, or El Niño, cooler sea surface temperatures (SST) in the Coral Sea promote a more southerly wave direction and lower significant wave heights as a result of reduced cyclonic activity. The opposite is held true during positive SOI phases, or La Niña, when increased Coral Sea SST amplifies cyclonic activity and a more easterly wave direction and higher significant wave heights (McSweeney and Shulmeister, 2018). The impacts of ENSO on Australian climate (i.e. rainfall) have been shown to be modulated by the Interdecadal Pacific Oscillation (Power et al., 1999). For positive IPO phases, the authors found no positive correlation between ENSO and various Australian climate variables as there is during negative phases. Splinter et al. (2012) suggested that this could be due to IPO's control over the position of the South Pacific Convergence Zone (SPCZ), which moves closer to (away from) Australia during negative (positive) IPO phases. As such, Splinter et al. (2012) suggest that when the SPCZ is closer to Australia, the wave climate of SE Queensland is more influenced by ENSO and vice versa when the SPCZ moves away, although they do not suggest an alternative control during the positive IPO phase.

Establishing a correlation between atmospheric and wave climate is relatively straightforward. Global hindcast wave climate data is readily available through the NOAA

WAVEWATCH III model and climate index data can be acquired from a variety of sources including NOAA and the National Weather Service. In order to detect primary climate drivers of shoreline change, a spatiotemporally robust shoreline position dataset is needed to perform correlation analyses with the same climate data. There are very few examples of shoreline monitoring programs that have been active long enough to describe shoreline variability at the interdecadal (IPO) time scale. Previous studies that have attempted to directly correlate natural shoreline evolution with climate relied on marginally suitable shoreline datasets with regards to spatial and temporal coverage. These studies relied on accurate, yet spatially limited, beach profile data (Ranasinghe et al., 2004), infrequent aerial photography with one shoreline measurement every three to five years (McSweeney and Shulmeister, 2018), and coastal morphodynamic modeling without ground reference data (Mortlock and Goodwin, 2016). While all of these studies agree that there is a definitive link between ENSO and SE Australian shoreline variability, none attempted to correlate the observed change with other local climate phenomena (Subtropical Ridge, Southern Annular Mode, among others) and all failed to investigate if and how IPO modulates the shoreline response to ENSO. This dissertation seeks to determine if there is indeed a secondary climate control on shoreline change during positive IPO phases, when the coupling between Australian atmospheric and wave climate with ENSO is weakened.

Given that aerial photographic surveys are conducted sporadically in the region and there is a paucity of other survey data, there are very few shoreline data sources that satisfy the temporal and spatial demands of this investigation. Landsat is likely the only imagery

source that has the temporal extent (1972-present) necessary to investigate interdecadal trends with a global spatial coverage. Delineating shoreline positions using Landsat imagery is far from novel as the data has previously been used to understand the dynamics of mangroves (Fromard et al., 2004), impacts of river dams on coastal erosion processes (Kuenzer et al., 2014), among many others. Like all studies that primarily utilize satellite remote sensing imagery, extensive ground referencing of products derived from the imagery should be performed to ensure that what we are interpreting from pixels accurately represents real world features.

The most commonly used reference data for validating shorelines derived from Landsat imagery is high-resolution aerial photography and satellite imagery (Ford, 2013; Jimenez et al., 1997; Pradjoko and Tanaka, 2010). While this may be a satisfactory for investigations of static features, an aerial photograph only captures the instantaneous position of the shoreline at the time of acquisition. By definition, the shoreline is a 2D interface delineated as the area between high and low tide (intertidal zone). The instantaneous capture of the shoreline, interpreted as the high water line (HWL), does not take into account the spatial and temporal variability of the shoreline boundary (Boak and Turner, 2005). Shorelines can fluctuate centimeters to hundreds of meters in a horizontal direction under the influence of tides, major storms, and anthropogenic activities (Morton, 1991). As such, it should be assumed that the actual shoreline position during the time of aerial survey and Landsat flyover are not identical based on the natural variability of the boundary and the uncertainty will only increase as the time elapsed between the two increases. This dissertation provides a robust, field-based assessment on the accuracy of

shorelines delineated using seven spectral water indices, from which the best performing will be used to map historical shoreline positions in the study area for correlation to climate.

In addition to investigating the influence of climate on yearly to decadal shoreline change, the impacts of extreme storm events are analyzed here using revolutionary satellite imagery. Early on in my PhD, I was granted an Education and Research partnership with Planet Labs, Inc., which affords me 10,000 km^2 of free imagery per month. Their PlanetScope data product is acquired by over 150 CubeSats operating in low earth orbit, enabling them to collect global 3 m multispectral imagery every day. This revelation in satellite imaging technology alleviates the previous tradeoff between high temporal and spatial resolution using a single platform (i.e. Landsat). Fortuitously, Tropical Cyclone Oma struck SE Queensland in February 2019, presenting itself as an opportune event for using the new dataset to observe and quantify extreme, near instantaneous shoreline changes in response to the storm wave climate. The high spatial and temporal resolution of PlanetScope imagery enabled mapping of the high water line (HWL), which was used as a shoreline indicator across 200 km of shoreline.

Given that this is the first application of using PlanetScope imagery to map shoreline positions, this dissertation provides a robust quantitative assessment on the uncertainty of the technique (in addition to assessing storm-induced shoreline changes). Total shoreline position uncertainty is assessed following the methods of Hapke et al. (2006) and Ruggiero and List (2009). Total uncertainty takes into account the ground sample distance of the data, geometric accuracy, and water level variations represented as

the proxy-offset bias. A robust 31 year wave climate record is used to calculate meteorological and oceanographic (metocean) parameters needed to estimate this bias. Storm-induced shoreline changes are assessed every 200 m along a nearly 200 km long study area with only net shoreline movements greater than the range of uncertainty used for interpretation. This dissertation exemplifies the advantages of using this cutting-edge satellite data to assess rapid and significant shoreline changes, especially for areas that are inaccessible due to infrastructure damage (as was the case for Fraser Island here).

References

Boak, E. H. and Turner, I. L., 2005. Shoreline definition and detection: a review. Journal of Coastal Research, 21(4), 688-703.

Coelho, C., Silva, R., Veloso-Gomes, F., Taveira-Pinto, F., 2009. Potential effects of climate change on northwest Portuguese coastal zones. ICES Journal of Marine Science, 66, 1497–1507. https://doi.org/10.1093/icesjms/fsp132

Ford, M., 2013. Shoreline changes interpreted from multi-temporal aerial photographs and high resolution satellite images: Wotje Atoll, Marshall Islands. Remote Sensing of Environment, 135, 130-140. doi:http://dx.doi.org/10.1016/j.rse.2013.03.027

Fromard, F., Vega, C., Proisy, C., 2004. Half a century of dynamic coastal change affecting mangrove shorelines of French Guiana. A case study based on remote sensing data analyses and field surveys. Marine Geology, 208(2-4), 265-280. doi:http://dx.doi.org/10.1016/j.margeo.2004.04.018

Hallegatte, S., Green, C., Nicholls, R.J., Corfee-Morlot, J., 2013. Future flood losses in major coastal cities. Nature Climate Change, 3, 802–806. https://doi.org/10.1038/nclimate1979

Hapke, C.J., Reid, D., Richmond, B.M., Ruggiero, P., List, J., 2006. National Assessment of Shoreline Change: Part 3: Historical Shoreline Changes and Associated Coastal Land Loss along the Sandy Shorelines of the California Coast. U.S. Geological Survey Open-file Report 2006-1219.

Hemer, M.A., McInnes, K.L., Ranasinghe, R., 2012. Climate and variability bias adjustment of climate model-derived winds for a southeast Australian dynamical

wave model. Ocean Dynamics, 62, 87–104. https://doi.org/10.1007/s10236-011-0486-4

Jimenez, J. A., Sanchez-Arcilla, A., Bou, J., Ortiz, M. A. 1997. Analysing short-term shoreline changes along the Ebro Delta (Spain) using aerial photographs. Journal of Coastal Research, 13(4), 1256-1266.

Kuenzer, C., Beijma, S. v., Gessner, U., Dech, S., 2014. Land surface dynamics and environmental challenges of the Niger Delta, Africa: Remote sensing-based analyses spanning three decades (1986–2013). Applied Geography, 53, 354-368. doi:http://dx.doi.org/10.1016/j.apgeog.2014.07.002

McSweeney, S. and Shulmeister, J., 2018. Variations in wave climate as a driver of decadal scale shoreline change at the Inskip Peninsula, southeast Queensland, Australia. Estuarine Coastal and Shelf Science, 209, 56-69. 10.1016/j.ecss.2018.04.034

Mortlock, T. R. and Goodwin, I. D., 2016. Impacts of enhanced central Pacific ENSO on wave climate and headland-bay beach morphology. Continental Shelf Research, 120, 14-25. 10.1016/j.csr.2016.03.007

Morton, R. A., 1991. Accurate shoreline mapping: Past, present, and future. Proceedings of the Coastal Sediments ’91, p. 997-1010. Seattle, WA.

Nicholls, R.J., Hanson, S., Herweijer, C., Patmore, N., Hallegatte, S., Corfee-Morlot, J., Chateau, J., Muir-Wood, R., 2008. Ranking Port Cities with High Exposure and Vulnerability to Climate Extremes. OECD Environment Working Papers, No. 1, OECD Publishing, Paris. https://doi.org/10.1787/011766488208

Power, S., Casey, T., Folland, C., Colman, A., Mehta, V., 1999. Inter-decadal modulation of the impact of ENSO on Australia. Climate Dynamics, 15(5), 319-324. https://doi.org/10.1007/s003820050284

Pradjoko, E., and Tanaka, H. (2010). Aerial photograph of Sendai Coast for shoreline behavior analysis. Proceedings of the 32nd International Conference of Coastal Engineering, p. 13.

Ranasinghe, R., McLoughlin, R., Short, A., Symonds, G., 2004. The Southern Oscillation Index, wave climate, and beach rotation. Marin Geology, 204(3-4), 273-287. https://doi.org/10.1016/S0025-3227(04)00002-7

Reimann, L., Vafeidis, A. T., Brown, S., Hinkel, J., Tol, R. S. J., 2018. Mediterranean UNESCO World Heritage at risk from coastal flooding and erosion due to sea-level rise. Nature Communications, 9, 4161.

Ruggiero, P. and List, J.H., 2009. Improving Accuracy and Statistical Reliability of Shoreline Position and Change Rate Estimates. Journal of Coastal Research, 25(5), 1069-1081.

Sahin, O., Stewart, R. A., Faivre, G., Ware, D., Tomlinson, R., Mackey, B., 2019. Spatial Bayesian Network for predicting sea level rise induced coastal erosion in a small Pacific Island. Journal of Environmental Management, 238, 341-351.

Slott, J.M., Murray, A.B., Ashton, A.D., Crowley, T.J., 2006. Coastline responses to changing storm patterns. Geophysical Research Letters, 33. https://doi.org/10.1029/2006GL027445

Splinter, K. D., Davidson, M. A., Golshani, A., Tomlinson, R., 2012. Climate Controls on longshore sediment transport. Continental Shelf Research, 48, 146-156. https://doi.org/10.1016/j.csr.2012.07.018

Thom, B. G., Eliot, I., Eliot, M., Harvey, N., Rissik, D., Sharples, C., Short, A. D., Woodroffe, C. D., 2018. National sediment compartment framework for Australian coastal management. Ocean & Coastal Management, 154, 103-120.

Thorne, K., MacDonald, G., Guntenspergen, G., Ambrose, R., Buffington, K., Dugger, B., Freeman, C., Janousek, C., Brown, L., Rosencranz, J., Holmquist, J., Smol, J., Hargan, K., Takekawa, J., 2018. U.S. Pacific coastal wetland resilience and vulnerability to sea-level rise. Science Advances, 4(2).

Chapter 2

Using GPS-Surveyed Intertidal Zones to Determine the Validity of Shorelines Automatically Mapped by Landsat Water Indices

Satellite remote sensing has been used extensively in a variety of shoreline studies and validated using aerial photography. This ground referencing method only represents an instantaneous depiction of the shoreline at the time of acquisition and does not take into account the spatial and temporal variability of the dynamic shoreline boundary. The availability of Landsat 8's Operational Land Imager to accurately delineate a shoreline is assessed by comparing all known Landsat water index-derived shorelines with two GPS-surveyed intertidal zones that coincide with the satellite flyover date, one of which had near-neap tide conditions.

Seven spectral indices developed for automatically classifying water pixels were evaluated for their ability to delineate shorelines. The shoreline is described here as the area above and below maximum low and high tide, otherwise known as the intertidal zone. The high-water line, or wet/dry sediment line, was chosen as the shoreline indicator to be mapped using a handheld GPS. The proportion of the Landsat-derived shorelines that fell within this zone and their alongshore profile lengths were calculated. The most frequently used water index and the predecessor to Modified Normalized Difference Water Index (MNDWI), Normalized Difference Water Index (NDWI), was found to be the least accurate by a significant margin. Other indices required calibration of their threshold value to achieve accurate results, thus diminishing their replicability success for other regions.

MNDWI was determined to be the best index for automated shoreline mapping, based on its superior accuracy and repeatable, stable threshold value.

2.1 Introduction

Landsat imagery has been used for decades to study various earth system processes; one of significant importance is shoreline change. With the onset and acceleration of climate change and measured increases in global air and sea surface temperatures, sea level is rising at an alarming rate due to thermal expansion and ice melt (IPCC, 2014; Nicholls & Cazenave, 2010). The positions of global shorelines are expected to transgress as sea level rises, posing a significant threat to public health (Mendez-Lazaro, 2012; Ziska et al., 2003), socio-economics of coastal communities (Lane et al., 2013; Stern, 2006), coastal ecosystems (Gontz et al., 2013; Hernández-Delgado, 2015; Maio et al., 2014), and sites of cultural heritage (Gontz et al., 2011; Maio et al., 2012). Applications of various remote sensing techniques have been used to delineate variable shoreline positions to confront these issues. Remote sensing data were used to analyze the fifty-year evolution of the Guianese shoreline to understand the dynamics of mangroves (Fromard et al., 2004), impacts of river dams on coastal erosion processes and ecological equilibrium of the Niger Delta (Kuenzer et al., 2014), and to understand the impacts of a reduction in river sediment discharge on the Chongming Dongtan National Nature Reserve coastline in China as a prerequisite for an integrated management plan (Li et al., 2014).

High-resolution aerial photography has been used as reference data for decades in various coastal studies such as analyzing short-term shoreline changes (Ford, 2013; Jimenez et al., 1997; Pradjoko & Tanaka, 2010), projecting future shoreline positions

(Addo et al., 2008; Fenster et al., 1992; Leatherman, 1983), and calculating long-term shoreline recession rates (Dolan et al., 1979; Dolan et al., 1991; Smith & Zarillo, 1990). Although aerial photography provides a very high-resolution image of the shoreline, it only captures the instantaneous position at the time of acquisition. This poses a problem for analyzing changing shoreline positions in areas where the land/water boundary can fluctuate tens of meters across the beach face daily (Romine et al., 2009). Other survey methods have been employed to delineate the position of shorelines including LiDAR (Light Detection and Ranging; Liu et al., 2007; Yang et al., 2012), SAR (Synthetic Aperture Radar; Trebossen et al., 2005; Yu & Action, 2004), and beach profiling (Corbella & Stretch, 2012; Ruggiero & List, 2009). While all of the above techniques offer fine spatial resolution, the cost and/or time of data acquisition are excessively high and all but prohibit them as practical methods for change analysis with high spatial variability over short temporal scales.

In response to the limitations of previous survey methods, satellite remote sensing has been used extensively in a variety of shoreline studies (Garcia-Rubio et al., 2015; Kuleli et al., 2011; Pardo-Pascual et al., 2012). This method provides a more practicable approach to delineating shoreline positions over various spatial and temporal scales (Almonacid-Caballer et al., 2016; Hegde & Akshaya, 2015; Li & Gong, 2016). Several spectral indices have been developed for automatically extracting water pixels from Landsat imagery. Zhai et al. (2015) compared the performance of these spectral indices and concluded that the Automated Water Extraction Index (AWEI) and Modified Normalized Difference Water Index (MNDWI) indices perform better than the Normalized

Difference Vegetation Index (NDVI) and the Normalized Difference Water Index (NDWI) by comparing extraction results to shorelines manually interpreted from high-resolution DigitalGLobe Quickbird imagery. Fisher et al. (2016) performed a similar comparative analysis using high-resolution imagery and concluded that $AWEI_{sh}$, MNDWI, and their newly developed index, WI_{2015}, were the most accurate water classification indices.

Like Zhai et al. (2015), the majority of Landsat shoreline studies use high-resolution aerial photography to validate the shoreline location derived from the various extraction techniques (Almonacid-Caballer et al., 2016; Ghoneim et al., 2015; Li & Gong, 2016). Some studies did not even attempt to corroborate their shorelines with reference data (Dada et al., 2016; Hegde & Akshaya, 2015). A separate ground-based dataset is essential to understanding and validating the performance of any remote sensing product (Lillesand et al., 2015).

The biggest complication of using high-resolution aerial photography as validation data is that the instantaneous depiction of the shoreline at the time of acquisition does not consider the spatial and temporal variability of the shoreline boundary. The assumption that the shorelines observed in these images represent “normal” conditions is the most substantial and likely incorrect assumption in many shoreline investigations (Boak & Turner, 2005), even more so for those using Landsat. Over a given tidal cycle and depending on beach geometry, a shoreline can fluctuate centimeters to hundreds of meters in a horizontal direction. Over longer time scales (months to years), major storms and anthropogenic activities can move a shoreline significantly landward. As such, the shoreline is an extremely dynamic boundary that exhibits significant short and long-term

spatial fluctuation (Morton, 1991). In most published Landsat shoreline studies, aerial photography used as validation data is not collected during the same day as the satellite flyover. It can reasonably, and should be, assumed that the actual shoreline position during the aerial photography and Landsat acquisition days are not identical based on the natural variability of the boundary through the stage and range of tides, wind, and prevailing wave energy (Pajak & Leatherman, 2002). Therefore, using aerial photography as validation data for Landsat-extracted shorelines is likely not ideal.

2.1.1 Purpose

To overcome this limitation and truly test the capability of using Landsat to accurately define and describe changing shoreline positions, this paper uses GPS surveying to validate Landsat-derived shorelines. The shoreline boundary is best described as the area above low and below high tides and as such, the maximum of both of these stages is mapped using GPS. The intertidal zone GPS survey data and Landsat 8 imagery were collected within hours of each other to ensure the best possible temporal correlation. Seven Landsat-based spectral water indices are assessed for their ability to delineate the shoreline with the overarching goal of identifying an index best suited for the task.

2.1.2 Study Areas

This analysis was applied to a 5 km stretch of Atalaia Beach in Aracaju, Sergipe located in the northeastern region of Brazil (Figure 2.1). This region of Brazil is a classic example of a wave-dominated coastline with minimal tidal and river influence (Bhattacharya & Giosan, 2003; Dominguez, 1996; Wright & Coleman, 1973). The beach consists of clastic sediment predominantly composed of fine grained, well-rounded and

well-sorted quartz with small amounts of feldspar and trace amounts of mica and magnetite grains. The shoreline experiences a micro- to meso- tidal range (up to 2.5 m) and a falling sea level since the mid-Holocene highstand around 5.1 kya (Dominguez et al., 1992; Martin et al., 2003). The low-lying urban area of Aracaju is located adjacent to the beach and is at the greatest risk of flooding in northeastern Brazil (Muehe, 2010).

A second shoreline was surveyed along a 5 km stretch of the Salisbury State Beach Reservation in Salisbury, Massachusetts, USA (Figure 2.2). The beach is a part of the larger Merrimack barrier system that extends to Cape Ann, Massachusetts to the south and Great Boars Head, New Hampshire to the north and has been well studied (Costas & FitzGerald, 2011; Dougherty et al., 2004; FitzGerald & van Heteren, 1999; FitzGerald et al., 2002; Hein et al., 2012). The beach consists of fine sand to cobble-sized sediment, typical of a paraglacial barrier system and is influenced by both tides and waves ("mixed energy", FitzGerald & van Heteren, 1999). The shoreline experiences a micro- to meso-vertical tidal range, averaging 2.6 m (Smith & FitzGerald, 1994). Sea level has risen approximately 10 m across northern Massachusetts since 7.5-6.8 kya (Engelhart & Horton, 2012).

2.2 Methods

A single Landsat 8 Operational Land Imager image was acquired for each study area. The Aracaju scene (path: 215, row: 68) was acquired on July 11, 2016, one day prior to the month's neap tide. Tidal conditions were verified by tide height observations reported by the Banco Nacional de Dados Oceanográficos Centro de Hidrografia da Marinha. Landsat 8 flew over the study area (12:36 pm) almost midway between the

surveyed semidiurnal high (9:07 am) and low (3:24 pm) tides (Figure 2.3). The Salisbury scene (path: 12, row: 30) was acquired on July 16, 2017 during average tidal conditions. Tidal conditions were verified by tide height observations at the National Oceanic and Atmospheric Administration (NOAA) Plum Island/Merrimack River Entrance Station. Landsat 8 flew over the study area (3:26 pm) in between the surveyed semidiurnal low (11:18 am) and high (5:15 pm) tides (Figure 2.3).

The Landsat 8 Surface Reflectance (SR) data products were obtained from the USGS data archive (Vermote et al., 2016). SR was calculated using the Landsat 8 Surface Reflectance Code (LaSRC). The scenes were given an Image Quality value of 9, or best possible with no errors detected. The 30 m Level-1 precision- and terrain-corrected products (L1T) were acquired with radiometric calibration and geographic reference and as surface reflectance was already calculated, minimal processing steps were required. All procedures were carried out using the Environmental Systems Research Institute (ESRI) ArcGIS Desktop 10.5.1 software suite.

Shorelines are interpreted as the boundary separating water and non-water pixels calculated by spectral water indices. A total of seven indices were selected for comparison (Table 2.1). The Normalized Difference Vegetation Index (NDVI; Rouse et al. 1974) divides the difference in the near-infrared (NIR) and visible red bands (5 and 4) by the sum of the same bands. The Tasseled Cap Wetness index (TCW; Crist, 1985) subtracts the sum of the shortwave infrared bands (6 and 7) from the sum of the visible and NIR bands (2 through 5, Fisher et al., 2016). The Normalized Difference Water Index (McFeeters, 1996) divides the difference in the visible green and NIR bands (3 and 5) by the sum of the same

bands to enhance water pixels from the background. The Modified Normalized Difference Water Index (MNDWI; Xu, 2006) improved the discrimination of water body pixels by substituting the middle-infrared (MIR) band 6 in place of the NDWI's NIR band 5. The Automated Water Extraction Indices (AWEI) use five spectral bands (2, 3, 5, 6, 7) and empirically determined coefficients to "maximize separability of water and non-water pixels through band differencing, addition, and applying different coefficients" (Feyisa et al., 2014). Two separate equations were developed for areas with shadows and built-up urban backgrounds ($AWEI_{sh}$) and areas without ($AWEI_{nsh}$). The WI_{2015} uses surface reflectance data through the combination of bands 3 through 7 and their coefficients determined using linear discriminant analysis classification (Fisher et al., 2016).

Fisher et al. (2016) determined optimum index thresholds for all of these indices except NDVI. Thresholds classify each index into two categories, water and non-water pixels. They assessed the accuracy of each index's classification of pure water pixels determined from high-resolution imagery by plotting the true positive rate (TPR) against the false positive rate (FPR) across a range of thresholds. The optimum index thresholds for separating water and non-water pixels as calculated by Fisher et al. (2016) are used in this study (Table 2.2).

If a threshold performed poorly in extracting water pixels, a new optimal threshold value was determined using the Jenks-Caspall technique (Jenks & Caspall, 1971). This technique separates raster values where large changes in values occur and identifies the pixel value at the boundary of the largest difference in value (de Smith et al., 2015). This

maximum separation value is then used as the threshold to discriminate water and non-water pixels in the water index.

The Landsat-derived shorelines were created by digitizing the boundary of water and non-water pixels along the coastline as calculated by the water indices. Each index's digitized line boundary was exported as a unique shapefile for further spatial analysis in ArcGIS. To evaluate the true capacity of Landsat's ability to delineate the shoreline, it was imperative that the shoreline position during the maximum low and high tides of the Landsat flyover dates (July 11, 2016 and July 16, 2017) were accurately mapped. Fortunately, the Aracaju flyover date also fell one day before the bi-monthly neap tide. The intertidal zone is at its narrowest during a neap tide and thus provides the most vigorous assessment of the accuracy of a Landsat-delineated shoreline. The tidal range during the surveyed flyover date in Aracaju was 1.08 m, 0.15 m greater than the neap tidal range the following day (July 12, 2016)(Figure 2.3).

The wet/dry sediment line, representing the high water line (HWL), was chosen as the shoreline indicator to be mapped using handheld GPS to capture the true intertidal width on the Landsat flyover days. The HWL is the most common shoreline indicator used in coastal investigations and is visually observed as the extent of maximum wave run-up and the corresponding wet/dry sediment line (Boak & Turner, 2005)(Figure 2.4). It was estimated that it would take approximately one hour to survey a 5 km line so the surveys began 30 minutes prior to maximum high (and low) tide. A Garmin GPSMAP 64st handheld unit was used to survey the low and high near-neap tide shorelines along Atalaia Beach, Aracaju and average low and high tide shorelines in Salisbury, MA. The survey of

both lines in Aracaju was completed on July 11, 2016 and on July 16, 2017 in Salisbury, MA, corresponding with the Landsat flyover dates. Two obstacles, wildlife and infrastructure, were encountered during the Salisbury survey. These two areas are omitted from the Salisbury analysis resulting in a survey line slightly shorter than 5 km.

All of the Landsat water index-derived and GPS shorelines were imported into ArcMap 10.5.1 and georeferenced to the Universal Transverse Mercator projection system (zones: 24° S for Aracaju and 19° N for Salisbury, datum: WGS-84). The Landsat shorelines were assessed for their accuracy as a shoreline indicator by comparing them to the intertidal zone defined by the GPS shorelines. For both study areas, the proportion of the Landsat shoreline that's situated within the intertidal zone was calculated for each index by manually splitting the Landsat shoreline where it crossed in and out of the zone. The distance of each "in" and "out" line segment was then calculated and summed for a total Landsat shoreline distance and percentage that falls within the intertidal zone (Figure 2.5). In addition to comparing the "in zone" percentage of each Landsat shoreline, the true shoreline distance was calculated and compared to each Landsat shoreline. The actual along-shoreline distance was calculated by measuring the distances of the GPS survey lines along the high tide line.

2.3 Results

2.3.1 Threshold Evaluation

The optimal thresholds as determined by Fisher et al. (2016) were successful in delineating complete shorelines across the study area in Aracaju for five of the seven water indices (WI_{2015}, NDWI, MNDWI, NDVI, and $AWEI_{sh}$). TCW and $AWEI_{nsh}$ did not

produce a complete shoreline using the suggested optimal thresholds, -0.07 and -0.01, respectively (Figure 2.6). The index results show areas where water pixels were not extracted but should have been in the densely clouded region in the northeastern section of the study area. The cloud-covered area dominates the eastern one third of the study area (Figure 2.6). TCW and $AWEI_{nsh}$ struggled to discriminate the boundary of water and non-water pixels in the clouded coastal area and a complete shoreline delineation was not achieved. The $AWEI_{nsh}$ shoreline is missing a total of 291 m while the TCW shoreline is missing 668 m. Furthermore, a large inland water body was poorly defined by the indices using the optimal thresholds, especially $AWEI_{nsh}$ with >50% of the area omitted.

New thresholds for both the $AWEI_{nsh}$ and TCW indices were determined based on the performance of Fisher et al.'s (2016) suggested optimal thresholds. The new values were determined using the Jenks-Caspall algorithm (Jenks & Caspall, 1971), a form of variance-minimization classification, on the complete range of index pixel values. The Jenks-Caspall algorithm empirically groups similar data values to a number of classes as defined by the user. This is accomplished by minimizing the absolute deviation of each class from their mean, while maximizing the deviation of each class from the means of others (Slocum et al., 2009). By selecting only two classes for the $AWEI_{nsh}$ and TCW index values, the Jenks-Caspall clustering algorithm identified the pixel value that best partitions the index into water and non-water pixels (including clouds).

The new threshold determined using this method for $AWEI_{nsh}$ is -0.55 and -0.06 for TCW. Where the total pixel value ranges for $AWEI_{nsh}$ and TCW are -4.18 to 2.79 and -0.90 to 0.54, respectively, these new values represent small departures of 6.8% and

3.4% from Fisher et al.'s (2016) suggested values. Although the new threshold value for $AWEI_{nsh}$ is not a notable deviation from the old, it now classifies a greater number of index pixels with values between -0.55 and above as water including a peak reflectance around -0.3 (Figure 2.7). The mixed cloud and water pixels are no longer ommitted from the water pixel extraction using the new threshold values. As such, $AWEI_{nsh}$ and TCW are now successful in delineating a complete, more accurate shoreline (Figure 2.6). Furthermore, a large, cloud-free inland body of water is wholly classified as such using the new threshold value as opposed to the >50% ommission error using the old. All shoreline analyses involving $AWEI_{nsh}$ and TCW were conducted using the new Jenks-Caspall threshold values.

2.3.2 Comparison to True Shoreline Lengths

The shorelines extracted from each of the seven spectral index calculations were imported into ArcGIS and their lengths were measured (Table 2.3). The high tide line, as surveyed, was imported and the length calculated. The GPS-high tide line serves as the reference. Comparison of the index-derived shorelines with the GPS-high tide line were conducted suggesting all indices, except NDWI, produced shorelines with differences of <1.2% in Aracaju and <0.5% in Salisbury. All index-derived shorelines, except NDWI, were shorter than the GPS-high tide line.

2.3.3 Intertidal Zone Assessments

The high-water line was successfully mapped during the low and high tides in Aracaju and Salisbury using handheld GPS. The surveyed high and low tide lines have measured distances of 4,997 and 5,093 m in Aracaju and 4,811 m and 4,808 m in

Salisbury. Salisbury had a vertical tidal range of 2.56 m on July 16, 2017 while Aracaju had a range of 1.08 m on July 11, 2016 (Figure 2.3). Shoreline widths were measured every 100 meters along the study areas using the U.S. Geological Survey's Digital Shoreline Analysis System (Thieler et al., 2009). The average shoreline width in Aracaju is 52 m and 37.6 m in Salisbury.

For Aracaju, the Landsat water index that delineated a shoreline with the highest accuracy, or largest proportion within the intertidal zone, was WI_{2015} (Figure 2.9). Of its total length of 4,974 m, 4,715 m of the shoreline was located within the surveyed tidal zone and only 259 m fell outside the boundary for a total accuracy of 94.8%. MNDWI, $AWEI_{sh}$, and NDVI also produced accurate results as 92.9%, 92.0%, and 90.8% of their shoreline boundaries fell within the intertidal zone, respectively. The most inaccurate Landsat shoreline was mapped using the NDWI index. It had an accuracy of 6.3% as only 387 m of its total 6,124 m shoreline length was positioned within the intertidal zone. TCW and $AWEI_{nsh}$ produced moderately accurate results with delineated shorelines that fell within 84.8% and 78.6% of the intertidal zone.

The water index that mapped the narrow Salisbury intertidal zone with the highest accuracy was $AWEI_{nsh}$ (Figure 2.10). Of its total 4,788 m length, 4,686 m is positioned within the intertidal zone for a total accuracy of 97.8%. No other indices produced shorelines with accuracies above 90%. WI_{2015}, TCW, and MNDWI produced moderate results with accuracies of 77.5%, 80.6%, and 83.9%, respectively. $AWEI_{sh}$, NDWI, and NDVI yielded poor results with accuracies of 62.5%, 38.9%, and 9.1%.

2.4 Discussion

The optimal thresholds determined by Fisher et al. (2016) proved to be effective for some indices, albeit with widely varying degrees of accuracy. Original indices were used for all but TCW and $AWEI_{nsh}$, both of which struggled to create a complete shoreline through cloudy areas with their suggested thresholds. MNDWI and NDVI both used the zero threshold value as suggested by their original authors or others (Xu, 2006; Zhai et al., 2015), although only MNDWI did so with accurate results. The threshold value used for WI_{2015} (Fisher et al., 2016) was deemed unnecessary to change. Of the remaining two indices that utilized optimal thresholds suggested by Fisher et al. (2016), $AWEI_{sh}$ and NDWI; only $AWEI_{sh}$ had satisfactory accuracy. These trends point to an underlying complication with band index classifications in that the threshold value that is optimized for the index's use in a certain study area (i.e. Australia for Fisher et al., 2016). The threshold values may not be suitable for other locations because of different water and land surface conditions, cloud coverage, and other prevailing environmental conditions that affect index performance.

The $AWEI_{nsh}$ and TCW indices using Fisher et al.'s (2016) threshold struggled to discriminate between mixed water, cloud, and beach pixels, producing shorelines with missing segments in cloudy areas. This is a common issue in earth surface remote sensing studies as clouds and white sand have similar or even identical reflectance properties (Irish, 2000). A histogram of the complete range of $AWEI_{nsh}$ index values for the Landsat tile that covers Aracaju shows that Fisher et al. (2016) selected a threshold value that classifies only the purest of water pixels (Figure 2.7). Application of the Jenks-Caspall technique (Jenks & Caspall, 1971) lowered the threshold to include a shorter secondary reflectance

peak that likely includes water pixels that have some component of cloud, land surface, and/or breaking waves.

Using the new Jenks-Caspall threshold, $AWEI_{nsh}$ extracted water pixels in the open ocean that contained sub-pixel cloud components not identified using Fisher et al.'s (2016) suggested threshold. The threshold adjustment allowed for a complete delineation of the shoreline through the clouded portions of the Aracaju study area. Furthermore, the Jenks-Caspall threshold increased the accuracy of the $AWEI_{nsh}$ index in Salisbury by 37.5% compared to using the Fisher et al. (2016) threshold, which had an accuracy of 60.3%. In Salisbury, where the $AWEI_{nsh}$ shoreline lies outside the intertidal zone (using the older threshold), it falls just outside of the low tide GPS line. Given that the Salisbury study area was entirely cloud-free during Landsat acquisition, it is very likely that the index interpreted the spectral reflectance of breaking waves or whitecaps as a non-water pixel. These features are now almost entirely classified as water pixels based on $AWEI_{nsh}$'s incredibly robust shoreline delineation that has an accuracy of 97.8%. In addition, the Jenks-Caspall threshold increased the accuracy of TCW's shoreline delineation in Salisbury by 17.5%. While Fisher et al.'s (2016) thresholds for TCW and $AWEI_{nsh}$ produced the best results for their study area, similar results were not replicated here. An index that requires threshold calibration for every unique study area where applied, defeats the original purpose to provide a repeatable method that can be used globally.

The geometry of the two beaches has a significant influence on the width of the intertidal zone. Even though the Aracaju survey occurred in near-neap tide conditions, the intertidal zone has an average width of 52 m because of its low slope gradient (1-2°,

Pereira et al., 2016). Whereas the intertidal zone at Salisbury has a much narrower width of 37.6 m in spite of a greater vertical tidal range because of its steep gradient, which was determined to be 3.9° based on observed hydrographic and geomorphic conditions. Based on the average intertidal widths, the narrow Salisbury shoreline provides the most vigorous assessment for the Landsat-derived shorelines, even though the Landsat 8 flyover in Aracaju was concurrent with near-neap tide conditions. The Salisbury intertidal width is nearly completely covered by one Landsat pixel (30 m) providing little room for error.

The ability of a Landsat water index to delineate the shoreline boundary was assessed by comparing its interpreted alongshore length with the actual measured length and spatial agreement within the GPS-surveyed intertidal zones. Based on the results of both analyses (Table 2.4), it's quite clear that there is varying capabilities to accurately map shorelines among the seven water indices. Most frequently, an index produced an accurate result in one study area (>90% accuracy) and would fail to replicate those results in the second study area.

WI_{2015} produced a very accurate shoreline in Aracaju (94.8%) but not in Salisbury (77.5%). Given that it succeeded in delineating an accurate shoreline through cloudy data and not in clear, it's likely that the expanded width (almost two Landsat pixels instead of one) of the Aracaju intertidal zone allowed for a greater portion of the WI_{2015} to coincide with the zone boundaries.

NDVI had the most dichotomous results as it achieved 90.8% accuracy in Aracaju and 9.1% in Salisbury. Its shoreline lies within 15 m (half of one Landsat pixel) outside of

the low tide line in Salisbury, supporting the notion that the slightly wider (+25 m) shoreline in Aracaju has a significant influence on the resulting accuracy.

The $AWEI_{nsh}$ index produced a very accurate shoreline in Salisbury (97.8%), an environment with no cloud shadow coverage at the time of Landsat acquisition. On the contrary, it produced a moderately accurate shoreline (78.6%) in Aracaju, struggling to delineate in the clouded regions. $AWEI_{nsh}$ "is suited for situations where shadows are not a problem" (Feyisa et al., 2014) so this was an expected result.

The $AWEI_{sh}$ index produced an accurate shoreline in Aracaju with 92% falling within the cloudy intertidal zone. This was a 13.4% improvement over $AWEI_{nsh}$, which agrees well with the original intention of $AWEI_{sh}$ to "enhance the separability of water and dark surfaces such as shadow" (Feyisa et al., 2014), such as those from clouds present in Aracaju. Like the previous indices described, the $AWEI_{sh}$ shoreline fell within one half of a Landsat pixel outside of the low tide line in Salisbury for 37.5% of its total length.

The NDWI index is the oldest and most frequently cited spectral water index among the seven compared in this study. This is of particular concern to the authors as it was the poorest performing index by a large margin, producing a shoreline with 6.3% accuracy in Aracaju and 38.9% in Salisbury. In Aracaju, the NDVI shoreline drastically shifts in multiple locales producing an irregular "saw tooth" pattern atypical of an expected alongshore beach profile. This result disagrees with other Landsat shoreline studies such as Ozturk & Sesli (2015) who concluded that NDWI provided the best result for their study area. Although, the authors came to this conclusion by simply visually comparing

separability of shoreline infrastructure and water surfaces in the index images (Ozturk & Sesli, 2015).

The NDWI shoreline shows the land/water boundary incorrectly positioned near the extreme inland limit of the beach in Aracaju, particularly in the clouded regions. The commission of mixed water and cloud pixels with beach sand by NDWI would pose a significant problem for the automated mapping of a shoreline in global coastal areas.

This problem is alleviated by the substitution of the near-infrared band in NDWI with the mid-infrared band in MNDWI, which produced far more accurate shorelines compared to its predecessor. The MNDWI index had the best combined accuracy of all seven indices, with accuracies of 92.9% in Aracaju and 83.9% in Salisbury. It was capable of delineating an accurate shoreline through the clouded regions in Aracaju and fitting mostly within the narrow boundaries of the Salisbury intertidal zone. Given that all other indices could only achieve one of the two, it represents the best water index for automated shoreline mapping on a global scale. Of equal importance, MNDWI uses a threshold value of zero as suggested by Xu et al. (2006) and has been proven by Fisher et al. (2016) and verified by this study that it does not need to be adjusted for site-specific use. This is extremely important for its efficacy and use for mapping shorelines on a global scale.

The selection of MNDWI as the best index for automated shoreline mapping is based on performance in cloud and cloud-free areas and its proven and repeatable threshold value. While other indices may have performed better in a particular study area, they either could not replicate that same result (WI_{2015}) or required threshold adjustment to achieve superior results ($AWEI_{nsh}$). While the superb accuracy of $AWEI_{nsh}$ in Salisbury

(97.8%) is appealing at first glance, it required a determination of a new optimal threshold that may or may not be repeatable for other study areas in addition to yielding mediocre results in cloudy areas. Should a water index aside from MNDWI be desired for a new study area, the Jenks-Caspall technique proved to be a very effective method for determining an optimized site-specific threshold value.

2.5. Conclusions

Seven Landsat water spectral indices (NDVI, NDWI, MNDWI, TCW, WI_{2015}, $AWEI_{sh}$, $AWEI_{nsh}$) were assessed for their ability to delineate a shoreline that represents the temporally and spatially dynamic boundary. Two analytical methods were used: 1) comparison of water index derived shoreline lengths with GPS-high tide surveyed lines and 2) comparison of the location of the water index derived shorelines with respect to the GPS-high tide and GPS-low tide shorelines. The shoreline is most accurately defined as the zone above the lowest tide and below the highest. Thus, a comparison of Landsat-derived shorelines with their corresponding intertidal zones represents the most appropriate and rigorous assessment of the efficacy of Landsat shorelines derived by water indices to date.

MNDWI (Xu, 2006) was determined to be the best index for automated shoreline mapping based on its performance and threshold replicability. It had the highest combined accuracy with 88.4% of both shorelines falling within the intertidal zone, putting it slightly ahead of $AWEI_{nsh}$ (88.2%) and WI_{2015} (86.2%). MNDWI and WI_{2015} both proved to be successful in delineating shorelines through the clouded regions of Aracaju with accuracies of 92.9% and 94.8%, respectively. However, WI_{2015} could not replicate these same results

in Salisbury (77.5%), as much of its shoreline traced whitecaps located just outside of the narrow intertidal zone. The $AWEI_{nsh}$ index threshold value required calibration using the Jenks-Caspall classification technique in order to produce accurate results in both study areas. Of equal importance to MNDWI's superior performance in both cloudy (Aracaju) and narrow (Salisbury) intertidal zones is its repeatable, stable threshold value of zero that does not require site-specific calibration.

This investigation has proven the ability of Landsat to automatically and accurately delineate the shoreline boundary with the proper water index. It's also the first that has attempted to automatically map the shoreline boundary using the recently developed WI_{2015} index and has done so with moderate success, particularly in clouded regions. The authors suggest that the prototypal NDWI index not be used for future shoreline studies based on its combined accuracy of 22.6%.

2.6. Acknowledgements

The authors would like to acknowledge the 100K Strong in the Americas Innovation Fund Competition #9 (Gontz), UMass Boston and Universidade Tiradentes for providing financial support that allowed for collection of GPS data in Brazil. Thank you to Márcia Helena Galina Dompieri from the Brazilian Agricultural Research Corporation (Embrapa) for providing the RapidEye imagery used in the figures. Further acknowledgements go out to Dr. Matheus Batalha and the Universidade Tiradentes for their partnership and logistical support in this project. Landsat Surface Reflectance products courtesy of the U.S. Geological Survey. Final thanks to the reviewers of the journal whose comments made this a better manuscript. This work was carried out within

the Joint Doctoral Program in Earthquake Science and Applied Geophysics at the University of California San Diego and San Diego State University. Chapter 2, in full, is a reformatted version of the material as it appears in the *International Journal of Applied Earth Observation and Geoinformation*: Kelly, Joshua T. and Gontz, Allen. 2018. Using GPS-surveyed intertidal zones to determine the validity of shorelines automatically mapped by Landsat water indices. *International Journal of Applied Earth Observation and Geoinformation*. v. 65C, p. 92-104. Joshua Terence Kelly was the primary investigator and author of this paper.

Table 2.1: Water indices used to automatically delineate the shoreline boundary (ρ= surface reflectance).

Index	Source	Equation
NDVI	Rouse et al., 1974	$\frac{\rho_{b5} - \rho_{b4}}{\rho_{b5} + \rho_{b4}}$
TCW	Crist, 1985	$0.0315\rho_{b2} + 0.2021\rho_{b3} + 0.3102\rho_{b4} + 0.1594\rho_{b5} - 0.6806\rho_{b6} - 0.6109\rho_{b7}$
NDWI	McFeeters, 1996	$\frac{\rho_{b3} - \rho_{b5}}{\rho_{b3} + \rho_{b5}}$
MNDWI	Xu, 2006	$\frac{\rho_{b3} - \rho_{b6}}{\rho_{b3} + \rho_{b6}}$
$AWEI_{sh}$	Feyisa et al., 2014	$\rho_{b2} + 2.5 * \rho_{b3} - 1.5 * (\rho_{b5} + \rho_{b6}) - 0.25 * \rho_{b7}$
$AWEI_{nsh}$	Feyisa et al., 2014	$4 * (\rho_{b3} - \rho_{b6}) - (0.25 * \rho_{b5} + 2.75 * \rho_{b7})$
WI_{2015}	Fisher et al., 2016	$1.7204 + 171\rho_{b3} + 3\rho_{b4} - 70\rho_{b5} - 45\rho_{b6} - 71\rho_{b7}$

Table 2.2: Optimal index thresholds used to classify water and non-water index pixels (Fisher et al., 2016).

Index	Optimal Threshold
WI_{2015}	0.63
TCW	-0.01
NDWI	-0.21
NDVI	0
MNDWI	0
$AWEI_{sh}$	-0.02
$AWEI_{nsh}$	-0.07

Table 2.3: Alongshore lengths for the water index shorelines and comparison to measured lengths of the surveyed high tide lines.

Index	Length (m)	Difference (m)	% Difference
Aracaju, Brazil	**GPS = 4,997**		
WI_{2015}	4974	-23	0.5
TCW	4980	-17	0.3
NDWI	6124	1,127	22.6
NDVI	5056	-59	1.2
MNDWI	4978	-19	0.4
$AWEI_{sh}$	4992	-5	0.1
$AWEI_{nsh}$	4937	-60	1.2
Salisbury, MA	**GPS = 4,811**		
WI_{2015}	4785	-26	0.5
TCW	4787	-24	0.4
NDWI	5592	781	16.2
NDVI	4783	-28	0.5
MNDWI	4784	-27	0.5
$AWEI_{sh}$	4787	-24	0.4
$AWEI_{nsh}$	4788	-23	0.4

Table 2.4: Proportion of the Landsat shorelines that fall within the intertidal zones.

Index	In Zone (m)	Out Zone (m)	Total Distance	% In	% Out
Aracaju, Brazil					
WI_{2015}	4715.62	258.91	4974.53	94.8	5.2
TCW	4223.45	756.62	4980.07	84.8	15.2
NDWI	387.89	5736.7	6124.59	6.3	93.7
NDVI	4590.21	466.48	5056.69	90.8	9.2
MNDWI	4626.07	352.65	4978.72	92.9	7.1
$AWEI_{sh}$	4595.06	397.14	4992.20	92.0	8.0
$AWEI_{nsh}$	3882.13	1055.16	4937.29	78.6	21.4
Salisbury, MA					
WI_{2015}	3711	1074	4785	77.5	22.5
TCW	3863	924	4787	80.6	19.4
NDWI	2176	3416	5592	38.9	61.1
NDVI	438	4345	4783	9.1	90.9
MNDWI	4014	770	4784	83.9	16.1
$AWEI_{sh}$	2994	1793	4787	62.5	37.5
$AWEI_{nsh}$	4686	102	4788	97.8	2.2

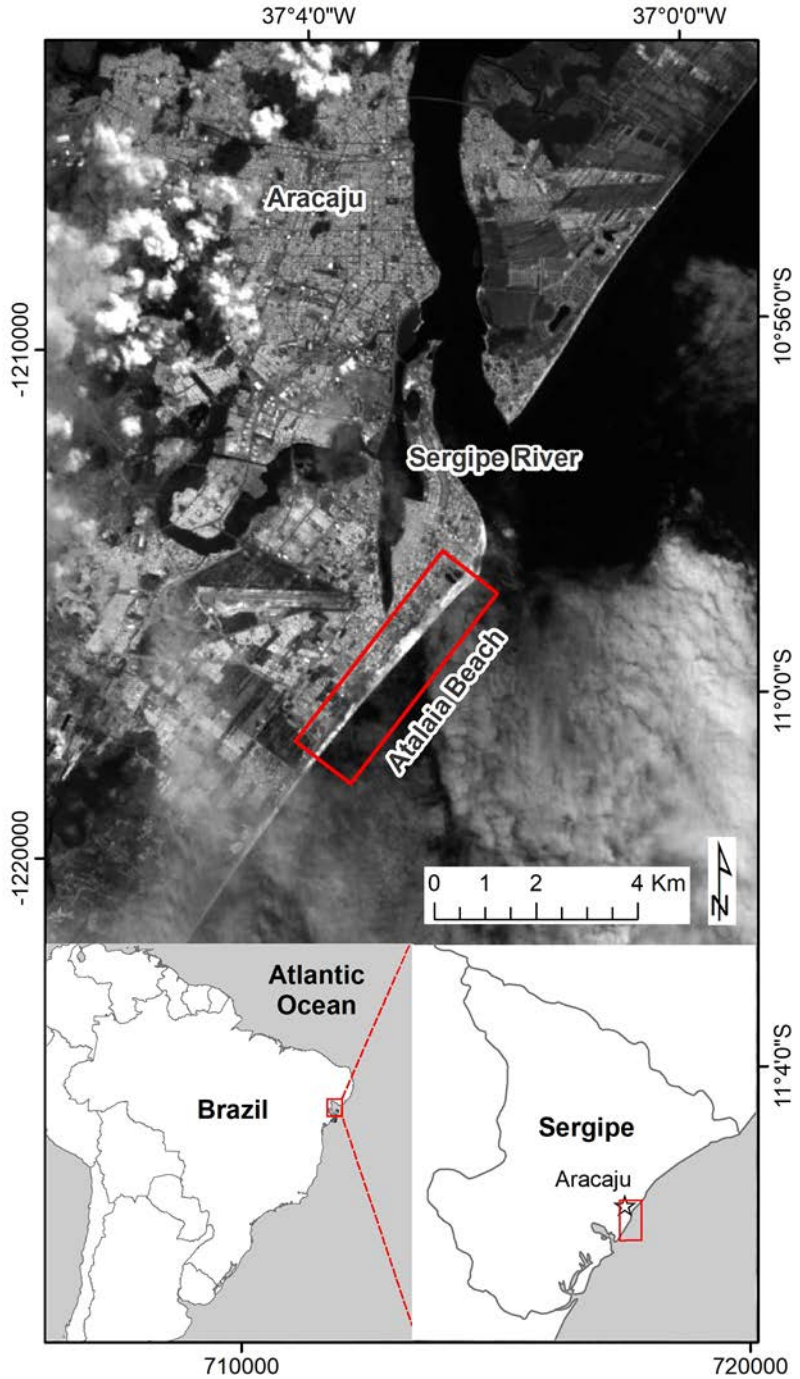

Figure 2.1: Location of the study area, Atalaia Beach, Aracaju, Sergipe, Brazil. Landsat 8 band 7 used as basemap (acquired on July 11, 2016).

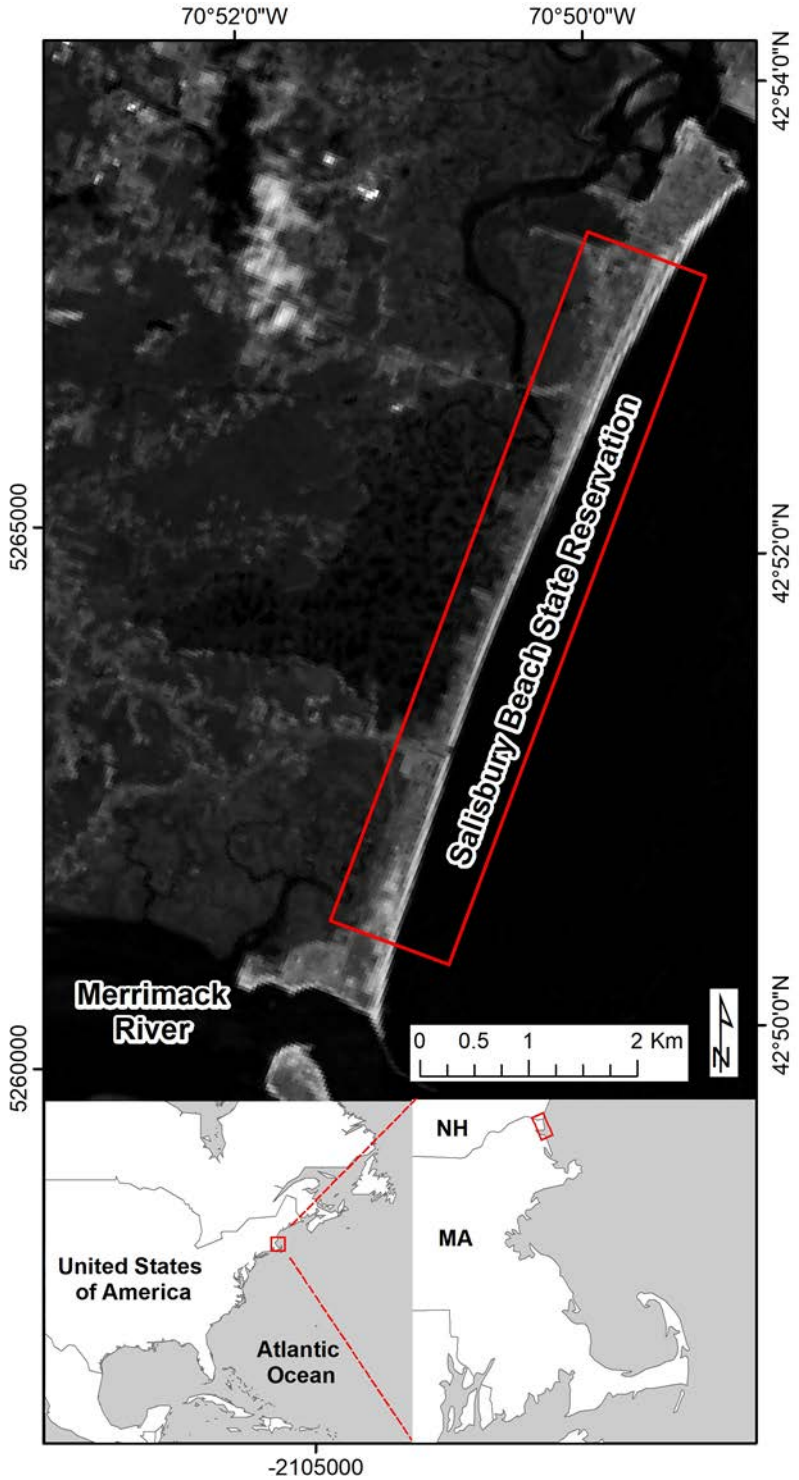

Figure 2.2: Location of the study area, Salisbury Beach State Reservation, Salisbury, Massachusetts, USA. Landsat 8 band 7 used as basemap (acquired on July 16, 2017). MA is abbreviation for Massachusetts and NH is New Hampshire.

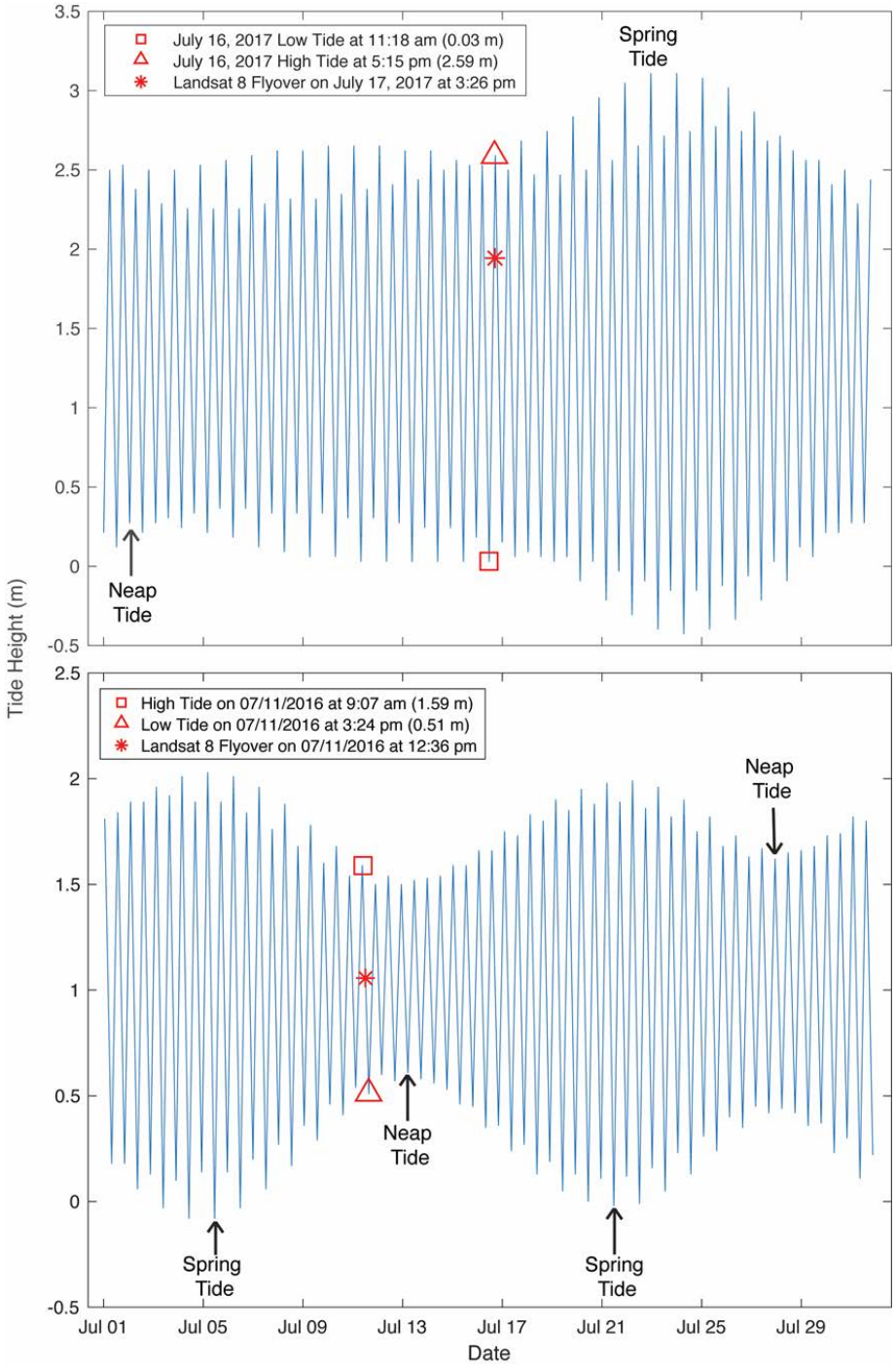

Figure 2.3: Tidal curves for Salisbury, Massachusetts (July 2017, top) and Aracaju, Brazil (July 2016, bottom). Note the near-neap tide conditions during the Landsat flyover in Aracaju on July 11, 2016. GPS surveys were conducted within 30 minutes of the low and high tide on the day of Landsat flyover.

Figure 2.4: Intertidal zone at Atalaia Beach, Aracaju. Arrow points to wet/dry sediment line that was surveyed by GPS and used as a shoreline indicator at high tide.

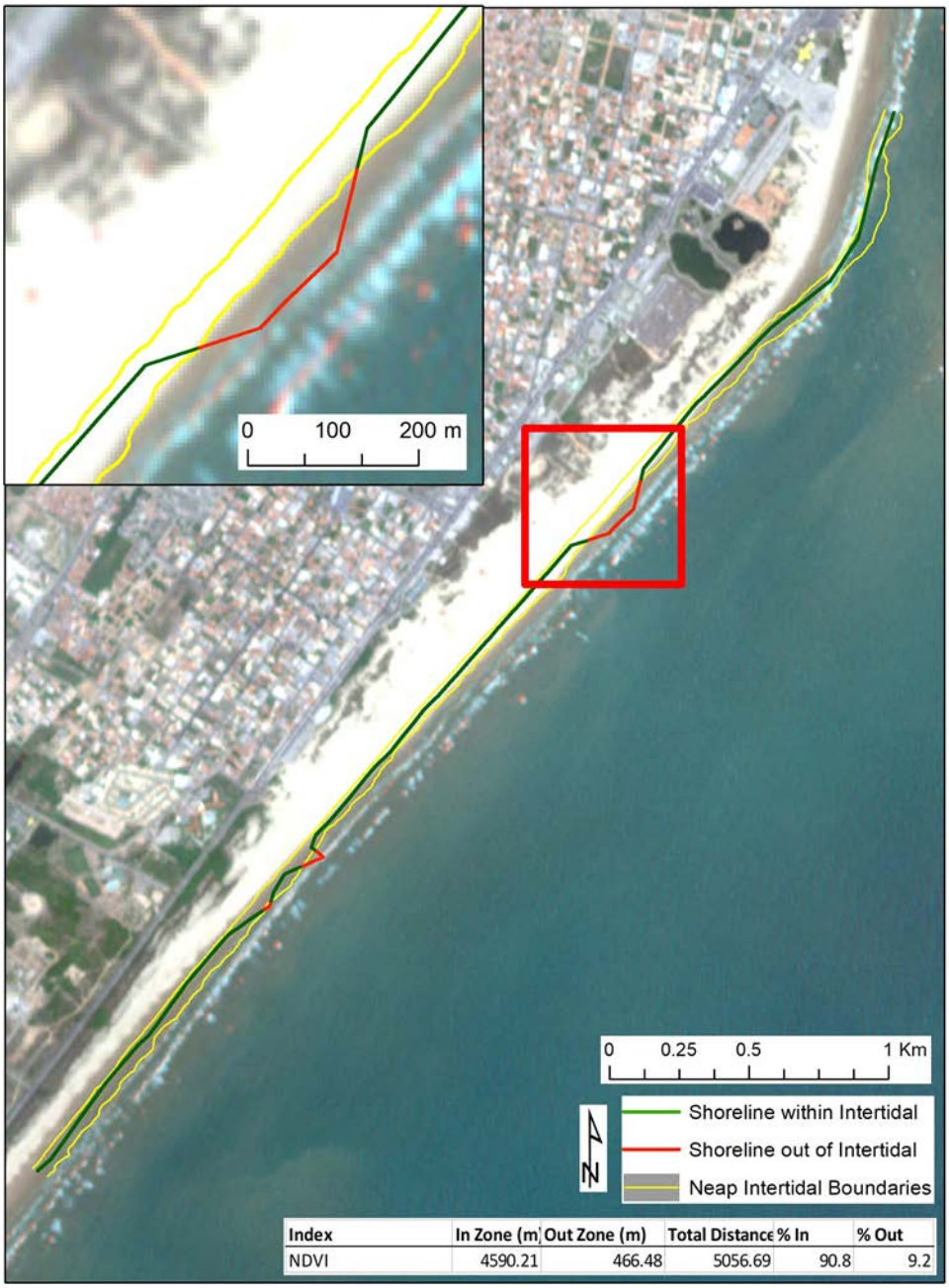

Figure 2.5: Calculating the accuracy of a Landsat-derived shoreline in Aracaju, Brazil (NDVI shown here). The shoreline vector is split where it crosses the intertidal zone boundary and the sum of the shoreline segments that are within the zone (green) and out (red) is calculated. RapidEye 5 m RGB combination is used as base map.

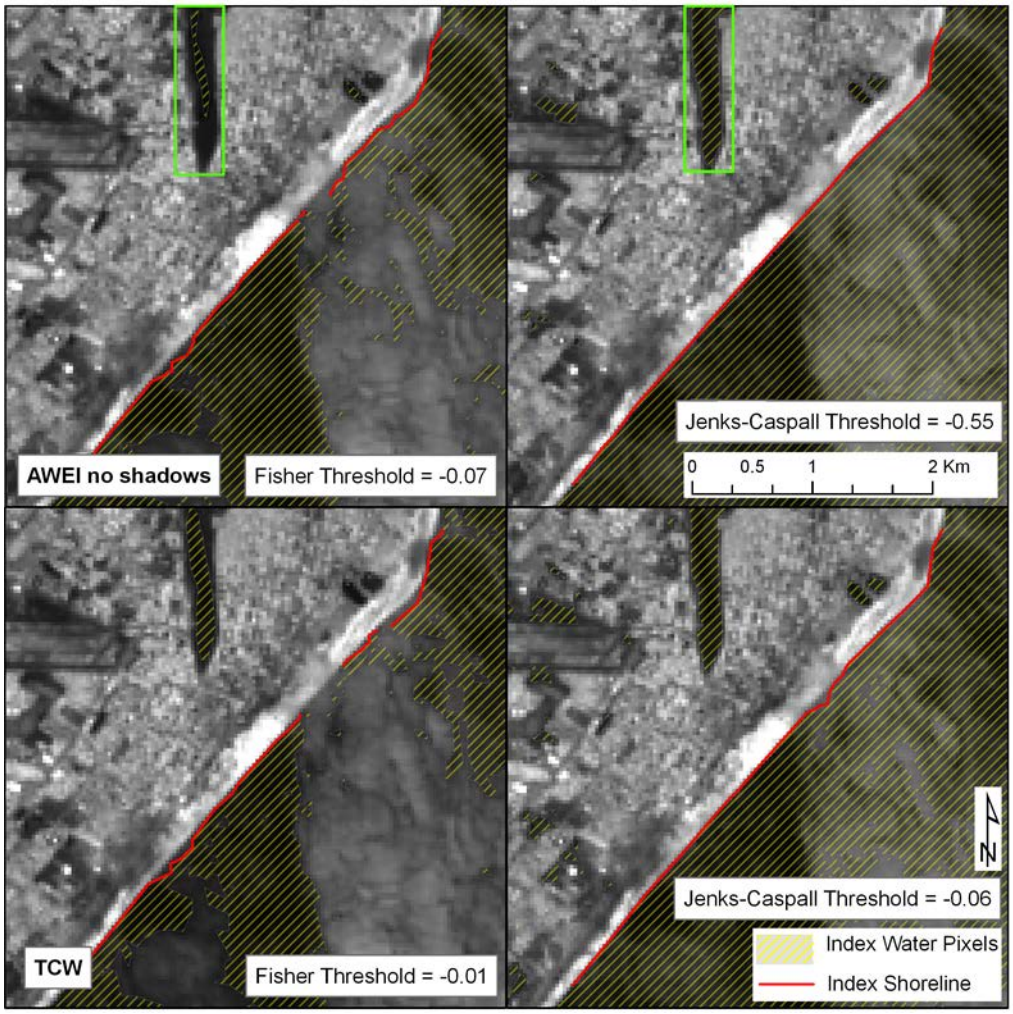

Figure 2.6: $AWEI_{nsh}$ and TCW extraction using the threshold values of -0.07 and -0.01 as suggested by Fisher et al. (2016) as well as those determined using Jenks-Caspall classification (-0.55 and -0.06) at Aracaju, Brazil. The Fisher et al. (2016) indices show significant omission errors in the densely clouded region and incomplete shoreline segments as a result. Jenks-Caspall classification could discriminate pure beach sand pixels from mixed water and cloud pixels within the coastal zone and allowed for the delineation of a complete shoreline in both indices. Green box highlights inland body of water that was completely classified using the new threshold value for $AWEI_{nsh}$, showing significant improvement over the old. Base map is OLI band 7.

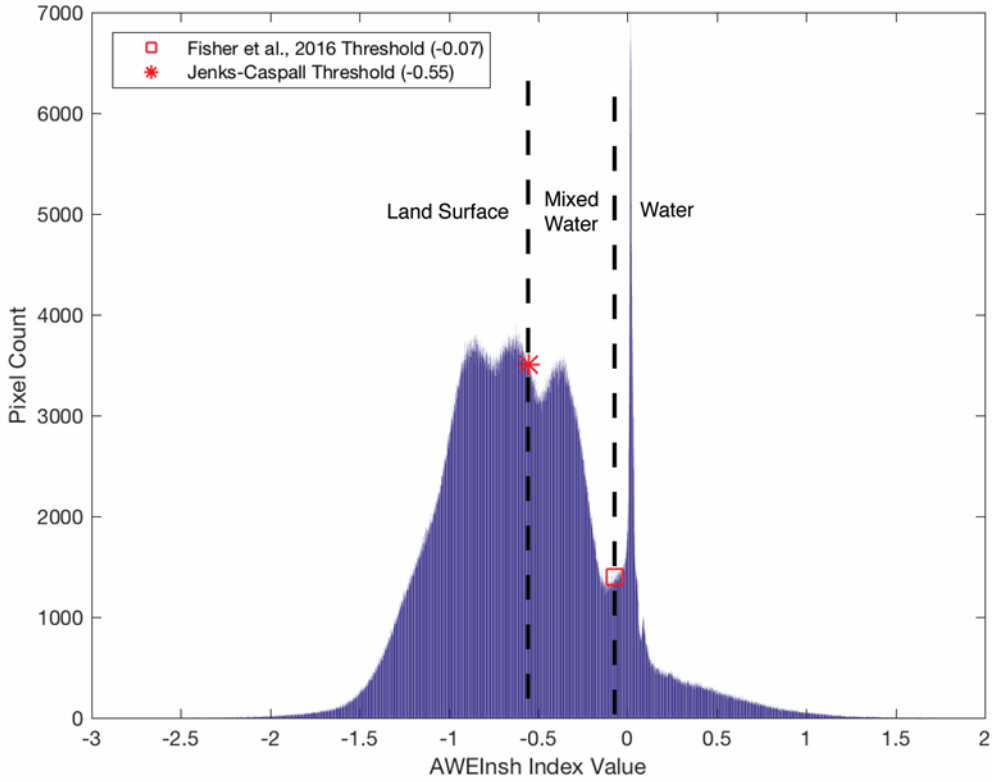

Figure 2.7: Range of $AWEI_{nsh}$ values calculated for Landsat tile LC82150682016193LGN00 used in this study (Aracaju). Fisher et al.'s (2016) and the Jenks-Caspall threshold values are shown.

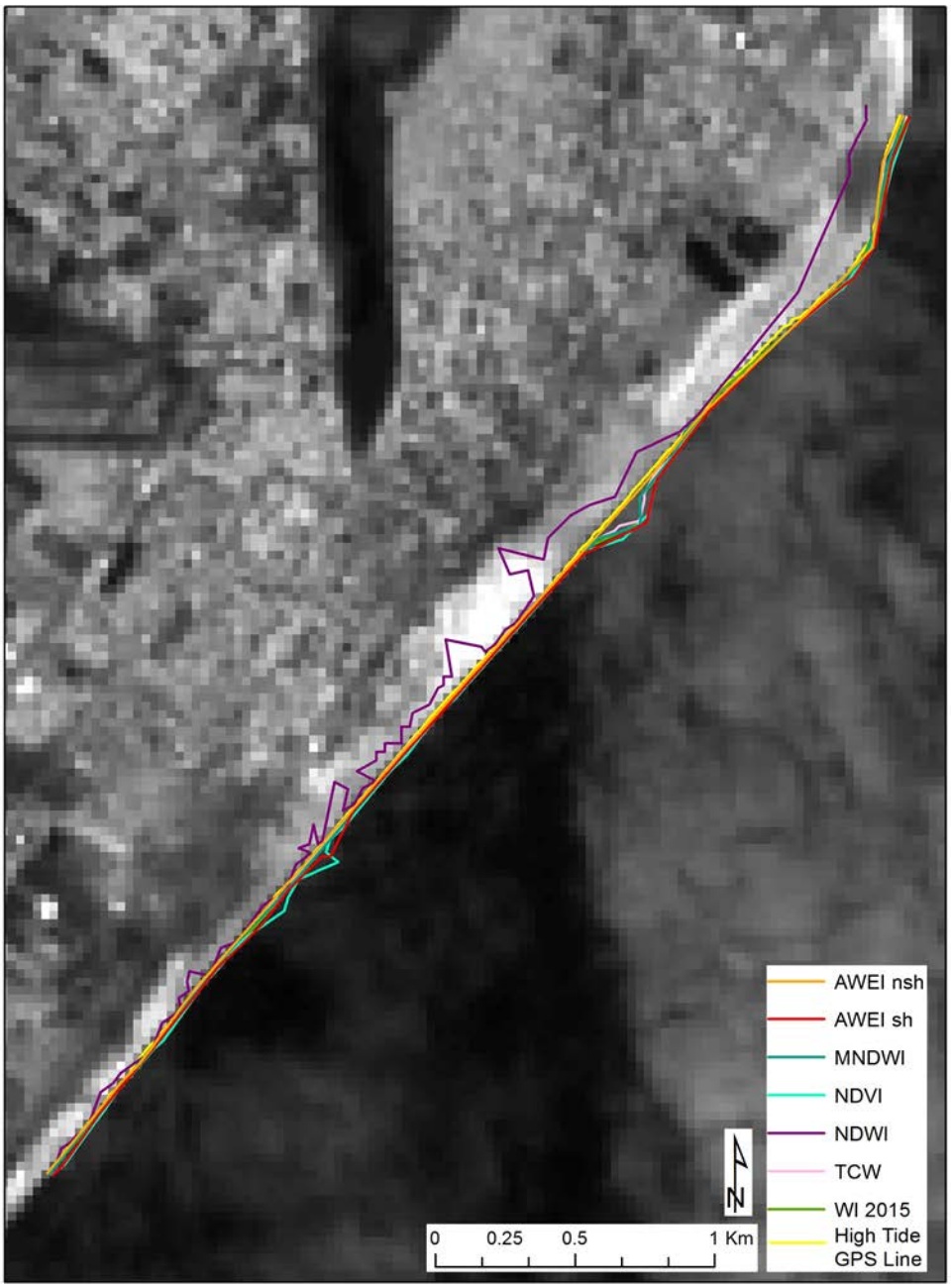

Figure 2.8: Comparing the lengths of the alongshore distance of the Landsat-derived shorelines to the measured length of the high tide GPS line (Aracaju). Base map is OLI band 7.

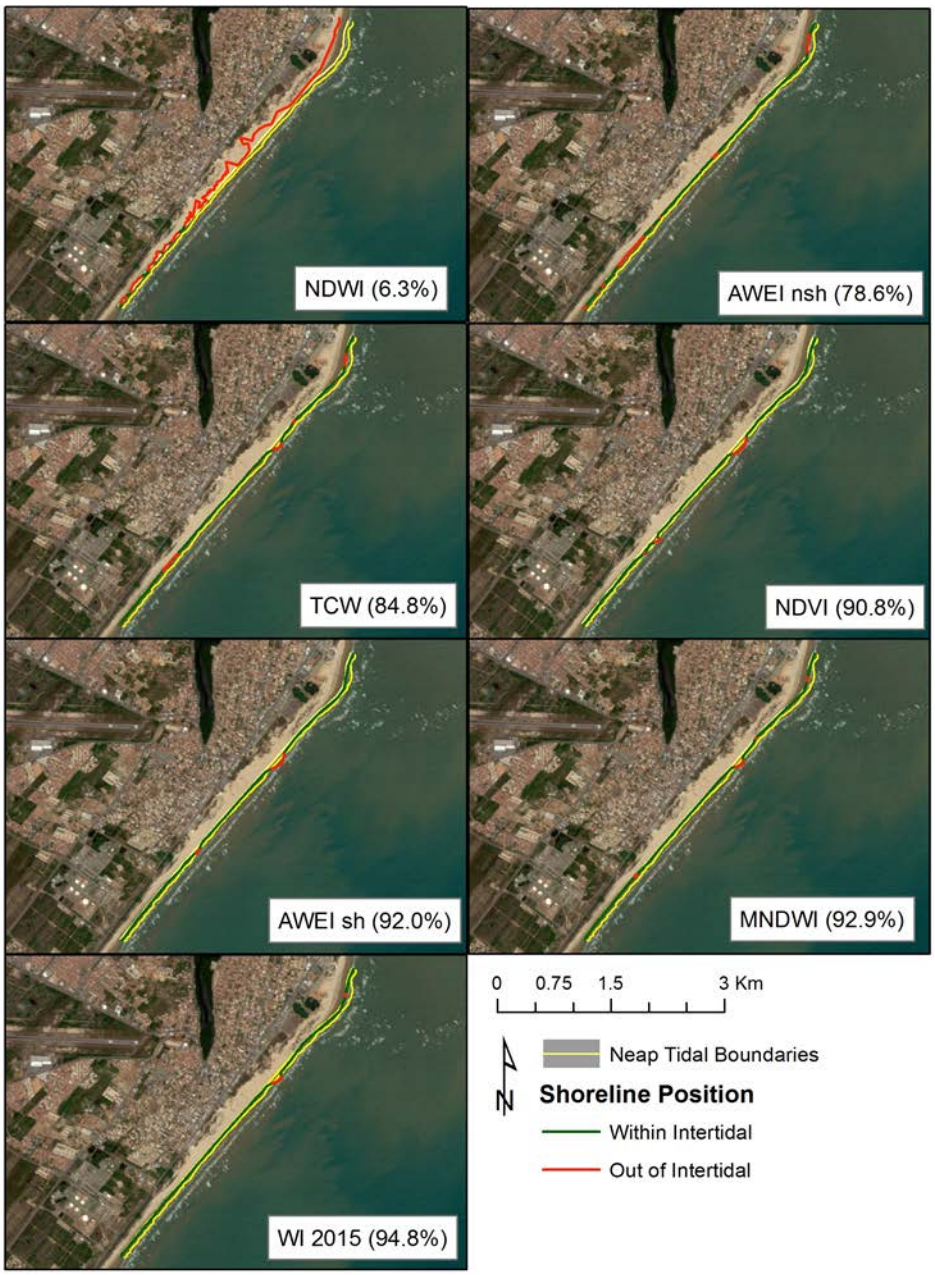

Figure 2.9: Intertidal zone accuracies for all seven indices (Aracaju, Brazil). WI_{2015} was the most accurate with 94.8% of its shoreline falling between the low and high tide lines while NDWI was the least accurate at 6.3%.

Figure 2.10: Intertidal zone accuracies for all seven indices. $AWEI_{nsh}$ was the most accurate with 97.8% of its shoreline falling between the low and high tide lines while NDVI was the least accurate at 9.1%.

References

Addo, K. A., Walkden, M., Mills, J. P., 2008. Detection, measurement and prediction of shoreline recession. ISPRS Journal of Photogrammetry & Remote Sensing, 63(5), 543-558. doi:http://dx.doi.org/10.1016/j.isprsjprs.2008.04.001

Almonacid-Caballer, J., Sánchez-García, E., Pardo-Pascual, J. E., Balaguer-Beser, A. A., & Palomar-Vázquez, J., 2016. Evaluation of annual mean shoreline position deduced from Landsat imagery as a mid-term coastal evolution indicator. Marine Geology, 372, 79-88.

Bhattacharya, J. P. and Giosan, L., 2003. Wave-influenced deltas: geomorphological implications for facies reconstruction. Sedimentology, 50, 187-210.

Boak, E. H. and Turner, I. L., 2005. Shoreline definition and detection: a review. Journal of Coastal Research, 21(4), 688-703.

Corbella, S. and Stretch, D., 2012. Decadal trends in beach morphology on the east coast of South Africa and likely causative factors. Natural Hazards and Earth System Sciences, 12, 2515-2527.

Costas, S. and FitzGerald, D., 2011. Sedimentary architecture of a spit-end (Salisbury Beach, Massachusetts): the imprints of sea-level rise and inlet dynamics. Marine Geology, 284(1-4), 203-216.

Crist, E. P., 1985. A TM Tasseled Cap equivalent transformation for reflectance factor data. Remote Sensing of Environment, 17, 301-306.

Dada, O. A., Li, G., Qiao, L., Ma, Y., Ding, D., Xu, J., Li., P., Yang, J., 2016. Response of waves and coastline evolution to climate variability off the Niger Delta coast during the past 110 years. Journal of Marine Systems, 160, 64-80.

Dolan, R., Fenster, M. S., Holme, S. J., 1991. Temporal analysis of shoreline recession and accretion. Journal of Coastal Research, 7(3), 723-744.

Dolan, R., Hayden, B., Rea, C., Heywood, J., 1979. Shoreline erosion rates along the middle Atlantic coast of the United States. Geology, 7(12), 602. doi:10.1130/0091-7613(1979)7<602:SERATM>2.0.CO;2

Dominguez, J. M., 1996. The São Francisco strandplain: A paradigm for wave-dominated deltas? Geological Society London Special Publications, 117(1), 217-231.

Dominguez, J. M., Bittencourt, A. C., Martin, L., 1992. Controls on Quaternary coastal evolution of the east-northeastern coast of Brazil: roles of sea-level history, trade winds and climate. Sedimentary Geology, 80, 213-232.

Dougherty, A. J., FitzGerald, D. M., Buynevich, I. V., 2004. Evidence for storm-dominated early progradation of Castle Neck barrier, Massachusetts, USA. Marine Geology, 210(1-4), 123-134.

Engelhart, S. E. and Horton, B. P., 2012. Holocene sea level database for the Atlantic coast of the United States. Quaternary Science Reviews, 54, 12-25.

Fenster, M. S., Dolan, R., Elder, J. F., 1992. A new method for predicting shoreline positions from historical data. Journal of Coastal Research, 9(1), 147-171.

Feyisa, G. L., Meilby, H., Fensholt, R., Proud, S. R., 2014. Automated Water Extraction Index: A new technique for surface water mapping using Landsat imagery. Remote Sensing of Environment, 140, 23-35.

Fisher, A., Flood, N., Danaher, T., 2016. Comparing Landsat water index methods for automated water classification in eastern Australia. Remote Sensing of Environment, 175, 167-182.

Fitzgerald, D. M. and Heteren, S. V., 1999. Classification of paraglacial barrier systems: coastal New England, USA. Sedimentology, 46, 1083-1108.

FitzGerald, D. M., Buynevich, I. V., Davis Jr., R. A., Fenster, M. S., 2002. New England tidal inlets with special reference to riverine-associated inlet systems. Geomorphology, 48(1-3), 179-208.

Ford, M.. 2013. Shoreline changes interpreted from multi-temporal aerial photographs and high resolution satellite images: Wotje Atoll, Marshall Islands. Remote Sensing of Environment, 135, 130-140. doi:http://dx.doi.org/10.1016/j.rse.2013.03.027

Fromard, F., Vega, C., Proisy, C., 2004. Half a century of dynamic coastal change affecting mangrove shorelines of French Guiana. A case study based on remote sensing data analyses and field surveys. Marine Geology, 208(2-4), 265-280. doi:http://dx.doi.org/10.1016/j.margeo.2004.04.018

Garcia-Rubio, G., Huntley, D., Russell, P., 2015. Evaluating shoreline identification using optical satellite images. Marine Geology, 359, 96-105. doi:http://dx.doi.org/10.1016/j.margeo.2014.11.002

Ghoneim, E., Mashaly, J., Gamble, D., Halls, J., AbuBakr, M., 2015. Nile Delta exhibited a spatial reversal in the rates of shoreline retreat on the Rosetta promontory comparing pre- and post-beach protection. Geomorphology, 228, 1-14.

Gontz, A., Maio, C., Rueda, L., 2013. The sunken forest of Duxbury, MA – constraints on sea level, coastal erosion and paleo-environments. Journal of Coastal Research, 6A, 168-176.

Gontz, A., Maio, C., Berkland, E., Wagenknecht, E., 2011. Assessment of the Colonial through Industrial aged cemetery on Rainsford Island, Boston Harbor, Massachusetts. Journal of Cultural Heritage, 12(4), 451-458.

Hegde, A. V. and Akshaya, B. J., 2015. Shoreline transformation study of Karnataka Coast: geospatial approach. Aquatic Procedia, 4, 151-156.

Hein, C. J., FitzGerald, D. M., Carruthers, E. A., Stone, B. D., Barnhardt, W. A., Gontz, A. M., 2012. Refining the model of barrier island formation along a paraglacial coast in the Gulf of Maine. Marine Geology, 307-310, 40-57.

Hernández-Delgado, E., 2015. The emerging threats of climate change on tropical coastal ecosystem services, public health, local economies and livelihood sustainability of small islands: Cumulative impacts and synergies. Marine Pollution Bulletin, 101(1), 5-28.

IPCC., 2014. Climate Change 2014: Synthesis Report. Contribution of working groups I, II, and III to the Fifth Assessment Report of the Intergovernmental Panel on Climate Change. Geneva, Switzerland.

Irish, R. R., 2000. Landsat 7 automatic cloud cover assessment. Proceedings of SPIE, Orlando, FL.

Jenks, G. F. and Caspall, F. C., 1971. Error on choroplethic maps: Definition, measurement, reduction. Annals of American Geographers, 61, 217-244.

Jimenez, J. A., Sanchez-Arcilla, A., Bou, J., Ortiz, M. A., 1997. Analysing short-term shoreline changes along the Ebro Delta (Spain) using aerial photographs. Journal of Coastal Research, 13(4), 1256-1266.

Kuenzer, C., Beijma, S. v., Gessner, U., Dech, S., 2014. Land surface dynamics and environmental challenges of the Niger Delta, Africa: Remote sensing-based analyses spanning three decades (1986–2013). Applied Geography, 53, 354-368. doi:http://dx.doi.org/10.1016/j.apgeog.2014.07.002

Kuleli, T., Guneroglu, A., Karsli, F., Dihkan, M., 2011. Automatic detection of shoreline change on coastal Ramsar wetlands of Turkey. Ocean Engineering, 38(10), 1141-1149. doi:http://dx.doi.org/10.1016/j.oceaneng.2011.05.006

Lane, D. R., Ready, R. C., Buddemeier, R. W., Martinich, J. A., Shouse, K. C., Wobus, C. W., 2013. Quantifying and valuing potential climate change impacts on coral reefs in the United States: comparison of two scenarios. PLoS One, 8, 1-13. doi:http://dx.doi.org/10.1371/journal.pone.0082579

Leatherman, S. P., 1983. Historical and projected shoreline mapping. Proceedings of the Coastal Zone '83 (pp. 2902-2910). San Diego: American Society of Civil Engineers.

Li, W. and Gong, P., 2016. Continuous monitoring of coastline dynamics in western Florida with a 30-year time series of Landsat imagery. Remote Sensing of Environment, 179, 196-209.

Li, X., Zhou, Y., Zhang, L., Kuang, R., 2014. Shoreline change of Chongming Dongtan and response to river sediment load: A remote sensing assessment. Journal of Hydrology, 511, 432-442. doi:http://dx.doi.org/10.1016/j.jhydrol.2014.02.013

Lillesand, T., Kiefer, R. W., Chipman, J., 2015. Remote sensing and image interpretation. 7th ed. Wiley.

Liu, H., Sherman, D., Gu, S., 2007. Automated extraction of shorelines from airborne light detection and ranging data and accuracy assessment based on Monte Carlo simulation. Journal of Coastal Research, 23(6), 1359-1369.

Maio, C., Gontz, A., Tennebaum, D., Berkland, E., 2012. Coastal hazard vulnerability assessment of sensitive historical sites on Rainsford Island, Boston Harbor, Massachusetts. Journal of Coastal Research, 28(1A), 20-33.

Maio, C., Gontz, A., Weidman, C., Donnelly, J., 2014. Late Holocene transgression and the drowning of a coastal forest: lessons from the past, Cape Cod Massachusetts, USA. Paleogeography, Paleoclimateology, Paleoecology, 393, 146-158.

Martin, L., Dominguez, J. M., Bittencourt, A. C., 2003. Fluctuating Holocene sea levels in eastern and southeastern Brazil: evidence from multiple fossil and geometric indicators. Journal of Coastal Research, 19(1), 101-124.

McFeeters, S. K., 1996. The use of the Normalized Difference Water Index (NDWI) in the delineation of open water features. International Journal of Remote Sensing, 17(7), 1425-1432.

Mendez-Lazaro, P., 2012. Potential impacts of climate change and variability on public health. Journal of Geology & Geophysics, 1(2), 2. doi:10.4172/2329-6755.1000e104

Morton, R. A., 1991. Accurate shoreline mapping: Past, present, and future. Proceedings of the Coastal Sediments ’91, p. 997-1010. Seattle, WA.

Muehe, D., 2010. Brazilian coastal vulnerability to climate change. Pan-American Journal of Aquatic Sciences, 5(2), 173-183.

Nicholls, R. J. and Cazenave, A., 2010. Sea-level rise and its impact on coastal zones. Science, 328(5985), 1517-1520.

Ozturk, D. and Sesli, F. A., 2015. Shoreline change analysis of the Kizilirmak Lagoon Series. Ocean & Coastal Management, 118(B), 290-308.

Pajak, M. J. and Leatherman, S., 2002. The high water line as shoreline indicator. Journal of Coastal Research, 18(2), 329-337.

Pardo-Pascual, J. E., Almonacid-Caballer, J., Ruiz, L. A., Palomar-Vazquez, J., 2012. Automatic extraction of shorelines from Landsat TM and ETM+ multi-temporal images with subpixel precision. Remote Sensing of Environment, 123, 1-11. doi:http://dx.doi.org/10.1016/j.rse.2012.02.024

Pereira, L. C., Vila-Concejo, A., Short, A. D., 2016. Coastal morphodynamic processes on the macro-tidal beaches of Para State under tidally-modulated wave conditions. In A. D. Short, & A. H. Klein (Eds.), Brazilian Beach Systems (Vol. 17, pp. 95-124). Switzerland: Springer International Publishing.

Pradjoko, E. and Tanaka, H., 2010. Aerial photograph of Sendai Coast for shoreline behavior analysis. Proceedings of the 32nd International Conference of Coastal Engineering, p. 13.

Romine, B. M., Fletcher, C. H., Frazer, L. N., Genz, A. S., Barbee, M. M., Lim, S.-C., 2009. Historical shoreline change, southeast Oahu, Hawaii; applying polynomial models to calculate shoreline change rates. Journal of Coastal Research, 25(6), 1236-1253.

Rouse, J. W., Haas, R. H., Schell, J. A., Deering, D. W., 1974. Monitoring vegetation systems in the Great Plains with ERTS. Third Earth Resources Technology Satellite-1 Symposium. SP-351, p. 3010-3017. NASA.

Ruggiero, P. and List, J. H., 2009. Improving accuracy and statistical reliability of shoreline position and change rate estimates. Journal of Coastal Research, 25(5), 1069-1081.

Slocum, T. A., McMaster, R. B., Kessler, F. C., Howard, H. H., 2009. Thematic Cartography and Geovisualization (3rd ed.). Upper Saddle River, New Jersey: Pearson Prentice Hall.

Smith, J. B. and FitzGerald, D. M., 1994. Sediment transport patterns at the Essex River inlet ebb-tidal delta, Massachusetts, U.S.A. Journal of Coastal Research, 10(3), 752-774.

Smith, G. L. and Zarillo, G. A., 1990. Calculating long-term shoreline recession rates using aerial photographic and beach profiling techniques. Journal of Coastal Research, 6(1), 111-120.

Smith, M. J., Goodchild, M. F., Longley, P. A., 2015. Geospatial Analysis (5th ed.). Leicester: The Winchelsea Press.

Stern, N., 2006. What is the economics of climate change? World Economics, 7(2), 1-10.

Thieler, E. R., Himmelstoss, E. A., Zichichi, J. L., Ergul, A., 2009. Digital Shoreline Analysis System (DSAS) version 4.0—An ArcGIS extension for calculating shoreline change (ver. 4.4, July 2017). U.S. Geological Survey
.
Trebossen, H., Deffontaines, B., Classeau, N., Kouame, J., Rudant, J.-P., 2005. Monitoring coastal evolution and associated littoral hazards of French Guiana shoreline with radar images. Comptes Rendus Geoscience, 337(13), 1140-1153. doi:http://dx.doi.org/10.1016/j.crte.2005.05.013

Vermote, E., Justice, C., Claverie, M., Franch, B., 2016. Preliminary analysis of the performance of the Landsat 8/OLI land surface reflectance product. Remote Sensing of Environment, 185, 46-56. doi:http://dx.doi.org/10.1016/j.rse.2016.04.008

Wright, L. D. and Coleman, J. M., 1973. Variations in morphology of major river deltas as functions of ocean wave and river discharge regimes. AAPG Bulletin, 57(2), 370-398.

Xu, H., 2006. Modification of Normalized Difference Water Index (NDWI) to enhance open water features in remotely sensed imagery. International Journal of Remote Sensing, 27(14), 3025-3033.

Yang, B., Hwang, C., Cordell, H. K., 2012. Use of LiDAR shoreline extraction for analyzing revetment rock beach protection: A case study of Jekyll Island State Park, USA. Ocean & Coastal Management, 69, 1-15. doi:http://dx.doi.org/10.1016/j.ocecoaman.2012.06.007

Yu, Y. and Action, S. T., 2004. Automated delineation of coastline from polarimetric SAR imagery. International Journal of Remote Sensing, 25(17), 3423-3438.

Zhai, K., Wu, X., Qin, Y., Du, P., 2015. Comparison of surface water extraction performances of different classic water indices using OLI and TM imageries in different situations. Geo-Spatial Information Science, 18(1), 32-42.

Ziska, L. H., Gebhard, D. E., Frenz, D. A., Faulkner, S., Singer, B. D., Straka, J. G., 2003. Cities as harbingers of climate change: Common ragweed, urbanization, and public health. Journal of Allergy and Clinical Immunology, 111(2), 290-295. doi:http://dx.doi.org/10.1067/mai.2003.53

Chapter 3

Bimodal Climate Control of Shoreline Change Influenced by Interdecadal Pacific Oscillation Variability along the Cooloola Sand Mass, Queensland, Australia

Wave climate in southeast Queensland, Australia has been correlated to changes in the Southern Oscillation Index (SOI), but observations of shoreline change associated with the variable wave climate have been limited due to a paucity of aerial photography, LiDAR, and other beach profiling datasets in this region. A multi-decadal, sub-annual temporal resolution shoreline dataset spanning 1996 to 2017 was produced using satellite imagery collected by Landsat 5, 7, and 8. A total of 147 shoreline positions were delineated using the Modified Normalized Difference Water Index on cloud-free imagery and corrected for horizontal offsets forced by variable tide stages at the satellite flyover time. The relative influence of SOI, the Southern Annular Mode (SAM), Pacific Decadal Oscillation (PDO), and Subtropical Ridge Latitude (STR-L) and Pressure (STR-P) on shoreline dynamics along the Cooloola Sand Mass in Queensland are assessed by performing cross correlations between their respective index values and shoreline change distances calculated by the Digital Shoreline Analysis System. A bimodal climate control of shoreline change is observed dependent upon the phase of the Interdecadal Pacific Oscillation (IPO). IPO modulates the impacts of ENSO on eastern Australia through its control over the position of the South Pacific Convergence Zone and elevating/lowering of tropical Pacific sea surface temperatures. During negative IPO, SOI is negatively correlated to the Cooloola Sand Mass shoreline indicating that the shoreline retreats during

negative SOI phases. During positive IPO, the impacts of SOI are weakened and the STR becomes the primary driver of shoreline change with shoreline response being contingent upon its orientation. The SW-NE aligned Noosa North shoreline erodes in response to poleward movement of the STR, likely due to the enhanced cross-shore wave attack as a result of anti-clockwise wave rotation. The opposite response is shown at the SE-NW aligned Rainbow Beach shoreline, which is oriented almost parallel to the incident wave direction and is sheltered by the Double Island Point headland. These results suggest that climate control on shoreline change at Cooloola Sand Mass, and likely other sand islands in the region, is two-tiered, whereby interdecadal variability of the IPO governs the relative influence of SOI and STR under the different IPO phases. The linked climate and shoreline variability correlation shown in this study provides significant insight into how the Cooloola Sand Mass shoreline will respond to future climate changes under a global warming scenario.

3.1 Introduction

Global sea-level rise has the potential to displace up to 187 million people or 2.4% of the global population and cost over $1 trillion USD if the upper-end of warming scenarios (4°C) is realized by 2050 (Hallegate et al., 2013; Nicholls et al., 2008). During the 20th century, eustatic sea level rose by 1.0 to 2.0 mm/year, primarily driven by ocean thermal expansion (0.3 to 0.7 mm/year) and mountain glacier melt (0.2 to 0.4 mm/year; Church et al., 2001). Acceleration of SLR throughout the 21st century at a rate of 0.013 mm/year would culminate in a total rise of 0.28 to 0.34 m globally (Church and White, 2006). While it is clear that a rise of this magnitude would have significant ramifications

for coastal populations and infrastructure across global shorelines, future variability in wave-driven sediment transport is expected to be the dominant process influencing shoreline modification on exposed, sandy coastlines in the coming decades (Coelho et al., 2009; Hemer et al., 2012; Slott et al., 2006).

In southeast Australia, a link between the Southern Oscillation Index (SOI) and regional wave climate is well established (Goodwin, 2005; Harley et al., 2010; McSweeney and Shulmeister, 2018; Mortlock and Goodwin, 2016; Ranasinghe et al., 2004; Short et al., 2000). Negative SOI phases (El Niño), which are associated with cooler sea-surface temperatures in the Coral Sea, promote a more southerly incident wave direction and dampen significant wave heights (Hs). The opposite is true during positive SOI polarity (La Niña), which modulates a more easterly wave component (anti-clockwise wave rotation) and elevated Hs (+0.10 m) due to increased extra-tropical cyclonic activity (McSweeney and Shulmeister, 2018). Short et al. (2000) and Ranasinghe et al. (2004) both describe a statistical relationship between SOI phase and shoreline behavior. They suggested that SOI modulation of wave climate drives the mean direction of longshore transport along the southeast Australia coast northward during El Niño and southward during La Niña (Short et al., 2000). McSweeney and Shulmeister (2018) observed widespread erosion along Rainbow Beach, Queensland (Inskip Peninsula) during periods of larger waves incident from a more easterly direction (La Niña) and subsequent shoreline recovery during El Niño. Similar behavior has been observed along the east coast of New Zealand's North Island beaches (Smith and Benson, 2001).

While El-Niño-Southern Oscillation (ENSO) is a climate phenomenon sourced in tropical latitudes, the wave climate in southeast Australia is also influenced by weather systems that operate in the mid-latitudes. As such, it has been suggested that wave climate variability could be modulated by other climate phenomena such as the Southern Annular Mode (SAM) (Goodwin, 2005), the Subtropical Ridge (STR) (Hemer et al., 2013a; Mortlock and Goodwin, 2015; O'Grady et al., 2015), and the Pacific Decadal Oscillation (PDO) (Goodwin, 2005; Pezza et al., 2007). SAM is the principal control on atmospheric variability in extratropical and high latitudes in the Southern Hemisphere (Marshall, 2003). SAM is zonally symmetric in nature (with opposite signs in Antarctica and mid-latitudes) and both models and observations suggest that it drives large-scale variability throughout the Southern Ocean (Hall and Visbeck, 2002). Goodwin (2005) suggests that wave climate in southeast Australia is modulated by both ENSO and SAM. When SAM is positive, a more easterly wave climate is promoted as mid-latitude storms are deflected northward (Goodwin, 2005). During negative SAM phases, mid-latitude storms form in the southern Tasman Sea generating waves incident from the south. The latitudinal position of the subtropical ridge in mean sea-level pressure (MSLP) along the east Australian margin (*L* index) is significantly correlated to yearly variations in rainfall and other atmospheric parameters such as wind and temperature (Drosdowsky, 2005; Pittock, 1973). Wind and wave climate projections based on future climate scenarios suggest that the latitudinal position of the STR is linked to a strengthening of the easterly winds north of the STR latitudinal position (Hemer et al., 2013b). As the STR continues to strengthen and move poleward under global warming scenarios (Grose et al., 2015), it is predicted that the

strengthened easterly winds will lead to an anti-clockwise rotation in incident wave direction along the New South Wales coast (Hemer et al., 2013b; Mortlock and Goodwin, 2015). This poleward trend will also dampen the influence of southerly wave climates at more northerly sites along the southeast Australia coast.

PDO describes the ENSO-like patterns of sea surface temperature (SST) variability in the Pacific Ocean basin operating at a decadal scale (Mantua et al., 1997; Tanimoto et al., 1993). Pezza et al. (2007) describe a near linear relationship between cyclone/anticyclone strength and strong PDO phases (determined as one standard deviation above/below its mean) across most of the Southern Hemisphere. During positive PDO phases, the Southern Hemisphere is characterized by more intense but fewer cyclones and anticyclones with the opposite pattern applying during negative phases. The Interdecadal Pacific Oscillation (IPO) is described as the interdecadal component of the PDO and tracks SST variability occurring in ~15-30 year intervals across the entire Pacific Basin (Power et al., 1999). Power et al. (1999) observed the modulation of ENSO impacts on Australian climate by the IPO. During positive IPO phases, there was no significant correlation between ENSO and Australian climate variables (i.e. rainfall) as there is during negative IPO phases. IPO has also been shown to modulate the position of the South Pacific Convergence Zone (SPCZ), which moves closer to (further from) Australia during negative (positive) IPO (Splinter et al., 2012). Splinter et al. (2012) suggest that when the SPCZ is closer to Australia (negative IPO), the wave climate of southeast Queensland is more influenced by ENSO and vice versa when SPCZ moves away (positive IPO).

Understanding how the shoreline responds to the variability and interaction of SOI, SAM, PDO, and STR during negative and positive IPO phases is integral to predicting the impact of future climate extremes. Several studies have suggested that SAM will become more positive on average (Gong and Wang, 1999; Kidson, 1999; Marshall, 2003) leading to further anti-clockwise rotation of incident wave direction (more easterly; Hemer et al., 2010). This future wave climate will likely be compounded by a substantial increase in La Niña frequency and a predicted doubling of the rate of extreme La Niña events in the 21st century due to global warming (Cai et al., 2015). Barnard et al. (2015) suggests that further increases in SAM would result in elevated erosion of coastlines in southeast Australia. FOAM climate modeling suggests that PDO may become weaker and shift to a higher frequency in response to global warming due to increased ocean buoyancy and faster Rossby waves under a warmer climate (Fang et al., 2014). A report by the Australian Government's Department of Climate Change highlighted the desire for better information on sediment and coastal dynamics and their susceptibility to climate change effects at manageable scales (Australian Government, 2009). The compartment scale shoreline-climate dynamics (as per Thom et al., 2018) presented here with exceptional temporal resolution supports these efforts to assess hazard vulnerability and coastal management planning.

3.1.1 Purpose

This paper aims to provide the first quantitative assessment on determining the relative influence of SAM, SOI, PDO, and STR variability during both negative and positive IPO phases on shoreline dynamics along the southeast Queensland coast. A high

temporal resolution satellite imagery dataset spanning the last 21 years is used to delineate shoreline positions and create a shoreline change curve that captures intra-annual variability and is statistically compared to contemporaneous SOI, SAM, PDO, and STR indices. This represents a significant improvement over previous studies in southeast Australia that relied solely on morphodynamic modelling (Mortlock and Goodwin, 2016), isolated beach profile data (Ranasinghe et al., 2004), or relatively infrequent aerial photography (McSweeney and Shulmeister, 2018) to describe how shoreline positions responded to solely SOI phase changes. The results of this study can support the development of short and long-term coastal management strategies for the Sand Island region of the east Australian coast and to predict changes in coastal sediment budgets and realignment.

3.1.2 Regional Setting

Sand islands and coastal dune fields constitute a significant part of the southeast Queensland coastline (e.g. Ellerton et al., 2018). The Cooloola Sand Mass (CSM) is one of these dune fields (Figure 3.1) and is suggested to be one of the oldest continuous coastal sand dune complexes in the world. Thermoluminescence dating has revealed an age of ~700 ka for the oldest dune units (Tejan-Kella et al., 1990), an age recently confirmed by optically stimulated luminescence dating (Walker et al., 2018). Most of the 240 km^2 sand mass is constructed of large, parabolic dunes with elevations reaching up to 240 m.a.s.l (Thompson, 1992) and the dune field abuts the ocean on its southeastern and northeastern flanks. The ~60 km long CSM shoreline is analyzed in this study (Figure 3.1) and is representative of the other SW-NE aligned sand islands (i.e. Fraser and North Stradbroke

Islands) and mainland attached dune fields that constitute ~370 km of southeast Queensland's coastline. The CSM is a part of two different secondary coastal compartments as defined by the National Climate Change Adaptation Research Facility (NCCARF, 2017). The northern half of the CSM (Rainbow Beach) is a part of the Fraser Island sediment compartment, which is Queensland's longest wave dominated beach. The southern half of the CSM (Noosa North) is a part of the Cooloola sediment compartment and shares similar geomorphic features to Fraser Island. Both compartments have a high sensitivity to erosion rating (4.5/5) owing to their susceptibility to sea level rise and erosive sandy shores.

The CSM open coast shoreline is wave-dominated and micro-tidal (Harris et al., 2002). The wave climate is influenced by six synoptic weather patterns operating in, or peripheral to, the Coral Sea: Tropical Cyclones, Tropical Lows, Anti-cyclonic Flows, East Coast Lows, Southern Tasman Lows, and Southern Secondary Lows (BBW, 1985; Harley et al., 2010; Shand et al., 2011; Short and Trenaman, 1992). These systems develop a wave climate with variable amplitudes and directions resulting in a strong seasonal cycle (Hemer et al., 2013a). The shoreline is supplied by an extensive longshore transport system that originates in New South Wales and is primarily active during periods of lower sea level (Boyd et al., 2008; Roy and Thom, 1981). This south-to-north drift system is still active for parts of the northern New South Wales and southern Queensland coasts, transporting approximately 500,000 m^3 of sand per year northward (Boyd et al., 2008). The subaqueous Breaksea Spit attached to the northern end of Fraser Island represents the terminus of this coastal transport system where estuarine ebb tidal currents transport littoral sands over the

shelf edge (Boyd et al., 2008). The sediments transported in this system are sourced from the proximal Middle Triassic Hawkesbury Sandstone, Ordovician turbidites, and Silurian granitoids (Veevers 2015). Petrographic descriptions of dunes located on Rainbow Beach indicate the sediment is mostly quartz with less than 2% heavy minerals and feldspar and little to no carbonate material (Thompson, 1983).

3.2 Materials and Methods

3.2.1 Shoreline Change Analysis

Google Earth Engine (EE) is a cloud-based GIS platform designed for conducting planetary-scale geospatial analysis (Gorelick et al., 2017). EE houses a multi-petabyte catalog of analysis-ready data, the bulk of which is Earth-observing satellite imagery such as the USGS Landsat, NASA MODIS, and ESA Sentinel-1 and Sentinel-2 historical archives. Google's parallel computation service can be accessed and controlled using an Internet browser-based application programing interface. A custom EE program was written using the JavaScript client libraries to automate the acquisition and majority of processing steps of the imagery used in this study.

A total of 364 Landsat satellite images (path: 89, row: 78) spanning 1996 to 2017 were acquired using EE. These images were collected by Landsat 5's Thematic Mapper, Landsat 7's Enhanced Thematic Mapper Plus, and Landsat 8's Operational Land Imager sensors. The Level-1 precision- and terrain-corrected products were acquired with radiometric calibration and orthorectification in the WGS84 Universal Transverse Mercator Zone 56S spatial reference. All images were atmospherically corrected (processed to Surface Reflectance) using the Landsat Ecosystem Disturbance Adaptive

Processing System (Masek et al., 2006) and the Landsat 8 Surface Reflectance Code (Vermote et al., 2016).

The method for delineating the shoreline position in Landsat imagery described by Kelly and Gontz (2018) was utilized in this study. They determined that the Modified Normalized Difference Water Index (MNDWI; Xu, 2006) is the best spectral index for automatically mapping shorelines in Landsat imagery based on its superior accuracy and repeatable threshold value. MNDWI distinguishes water and non-water pixels based on a normalized difference between surface reflectance values in the visible green and middle-infrared bands (equation 1). MNDWI calculations were iterated through the 364 Landsat images using the "normalized difference" EE mathematical operator.

$$MNDWI = \frac{\rho_{b3} - \rho_{b6}}{\rho_{b3} + \rho_{b6}} \quad (1)$$

The MNDWI EE GeoTIFF files were imported into ArcGIS (v. 10.5.1) for further processing. The images were visually inspected on a year-by-year basis for cloud contamination. Most spectral water indices struggle to discriminate between mixed water, cloud, and beach pixels leading to shorelines with missing segments in cloudy areas (Kelly and Gontz, 2018). As such, 217 images were discarded due to the presence of clouds. The remaining 147 images were reclassified into binary polygons where all pixels with MNDWI values greater than 0 representing water and pixels with MNDWI values less than 0 representing non-water were grouped. The shoreline is interpreted as the boundary that separates water (value=1) and non-water (value=0) pixels in the binary MNDWI image.

With the shoreline positions digitized in ArcGIS, the Digital Shoreline Analysis System (DSAS) was used to calculate change statistics on the time series of shoreline

vector data in an effort to discriminate distinct geomorphic compartments (Thieler et al., 2017). DSAS uses a measurement baseline method to calculate change statistics, which was constructed here by buffering a Landsat shoreline (February 17, 2017) 1 km landward. Transects were cast perpendicular to the shorelines from the baseline at 500 m intervals across the 60 km shoreline (Figure 3.2). DSAS calculates the distance each shoreline is from the baseline along the transects. The Shoreline Change Envelope (SCE), or distance between the shorelines farthest and closest to the baseline, was calculated for each transect representing the total change in shoreline movement for all available shoreline positions (Thieler et al., 2017). The resulting SCE values were used to define distinct shoreline compartments (based on relative morphodynamic behavior), for which shoreline change curves were then constructed. The shoreline positions determined by the intersection of a single Landsat shoreline with the DSAS transects were averaged to define a single position, or "Distance from Baseline" value, for each shoreline compartment. This approach was applied to all 147 shoreline positions and used to construct shoreline change curves for the individual shoreline compartments

3.2.2 Tide Correction

Previous studies that have used Landsat data to describe historical shoreline trends noted that vertical water-level changes due to tides produce significant horizontal changes in shoreline position, even along micro-tidal coasts (Almonacid-Caballer et al., 2016; Pardo-Pascual et al., 2014). Tide data were acquired from the Noosa Head and Mooloolaba tide gauges in order to correct the Landsat shoreline positions for tidal variations during the satellite flyover. The closest gauge to the study area, Noosa Head, is located 48 km to

the south (26° 23’ S, 153° 6’ E) but records managed by the Australian Bureau of Meteorology (BoM) are only available dating back to 2014. Records dating back to 1996 were acquired from the Mooloolaba tide gauge managed by the Queensland Government. The Mooloolaba Storm Surge tidal station is located an additional 33 km south of Noosa Head (26° 40’ S, 153° 8’ E). Dates and times of daily low and high tides as well as tide ranges are compared between the two datasets for 2017 to determine if they can be used interchangeably.

The width of the seasonal intertidal zones were needed in order to adjust shoreline positions to their non-tidal position. The seasonal widths are estimated here by constructing equilibrium beach profiles following the method of Bruun (1954) and Dean (1991) who found the following relationship:

$$h(y) = Ay^{2/3} \quad (2)$$

where h is the water depth relative to mean sea level, y is the horizontal distance from the shoreline, and A is a sediment scale parameter correlated to grain size (D). The sediment scale parameter (A) is determined by:

$$A = 0.51w^{0.44} \quad (3)$$

where A is in units $m^{1/3}$ and w is the settling velocity (cm/s) for D between 0.1 mm and 1 mm defined by (Vellinga 1983):

$$w = 273*D^{1.1} \quad (4)$$

The depth of closure (h_c), which represents the most seaward depth of littoral transport, marks the horizontal extent of an equilibrium profile and is described by Birkemeier (1985) as:

$$h_c = 1.75(H_s) - 57.9(H_s^2/g*T_p^2) \quad (5)$$

where H_s the significant wave height, T_p is the wave period, and g is the gravitational constant. The width of the beach profile (w_b) is then determined by:

$$w_b = (h_c/A)^{3/2} \quad (6)$$

A 31 year (1979-2009) wave record was obtained from the NOAA WAVEWATCH III (WWIII) hindcast dataset. These data were used to calculate seasonal mean H_s and T_p values for Australia (austral winter = JJA) for the generation of seasonal equilibrium beach profiles and intertidal zone widths (Table 3.1). A mean sediment grain size (D) of 0.225 mm was used based on the work of Walker et al. (2018). Zero water depth on the profiles is equivalent to the extent of wave run-up (wet/dry sediment line), which is one of the most frequently used shoreline indicators (Boak and Turner, 2005). The distance offshore of the Mean Lower Low Water line was extracted from the equilibrium profile knowing the average vertical tide range (1.1 m). The distance between these two points represents the seasonal intertidal width used to correct the Landsat-derived shoreline positions (procedure for austral spring shown in Figure 3.3).

To correct for tidal variations, Landsat shoreline dates and times (acquired in Greenwich Mean Time) were converted to local Australian Eastern Standard Time (+10 hours). Noosa Head gauge data were used to correct the 2014-2017 shorelines. Since BoM only provide daily low and high tide heights, heights at the time of Landsat flyover were interpolated based on the time difference between the Landsat flyover and first tide and the duration of the tide stage (Table 3.2). This ratio is multiplied by the tide range (in meters) to estimate the tide height at the time of Landsat flyover. Mooloolaba tide data are

provided in 10-minute intervals and the height at the time closest to the flyover time was used. The difference between this height and the high tide provides a percentage of total tide range the shoreline has been moved. This ratio is then multiplied with the appropriate seasonal intertidal width to determine the absolute distance the shoreline has moved further offshore due to tides. To finally "de-tide" the Landsat shoreline, this absolute distance is subtracted from the DSAS distance from baseline calculation. The DSAS distances were then normalized to the baseline shoreline (February 17, 2017) by subtracting baseline buffer distance (1,000 m).

3.2.3 Correlation to SOI, SAM, PDO, and STR

Monthly mean Southern Oscillation Index (SOI), Southern Annular Mode (SAM), Pacific Decadal Oscillation (PDO), Tripole Index for the Interdecadal Pacific Oscillation (TPI), and Sea Level Pressure (as a proxy for the Subtropical Ridge (STR)) data were acquired for the study time period (1996-2017) from NOAA and the National Weather Service for comparison to observed shoreline change. The SOI is a frequently used measurement of large-scale changes in sea level pressure between Tahiti and Darwin, Australia. SAM describes the latitudinal shift of the westerly wind belt that surrounds Antarctica. PDO describes an ENSO-like SST and pressure variability operating on a multi-decadal scale (Mantua et al., 1997). The *L* index, or latitudinal position of the STR, was calculated following the method of Drosdowsky (2005) using the NCEP/NCAR Reanalysis Mean Sea Level Pressure (MSLP) dataset (Kalnay et al., 1996). This method detects the latitude and magnitude of the maximum SLP over the 150° E longitude band over eastern Australia. The gridded 2.5° resolution SLP dataset was imported into ArcMap

v. 10.5.1 and interpolated to 0.5° using a Cubic Convolution resampling technique. This determines a new cell value based on fitting a smooth curve through the nearest 16 cell centers. The resampled global dataset was clipped to the 150° E longitude and 9-45° S latitude boundary extent defined by Drosdowsky (2005) and Grose et al. (2015). The location and pressure (in millibars) of the pixel with the highest MSLP was determined for each of the 264 time slices. These two variables represent the mean monthly position and intensity of the STR. TPI is a measure of interdecadal variability in the Pacific calculated as the difference between average SST in the central equatorial Pacific and southwest/northwest Pacific. A 3-month running mean of the TPI was used to identify the onset of negative and positive IPO phases during the study time period.

Trailing 3 month averages of the climate indices (i.e. SOI in June is the mean of AMJ) were calculated in order to prevent the omission of significant climate events in the downsampled datasets. The 3 month trailing averaged SOI, SAM, PDO, and STR time series (n = 264) were interpolated to match the sample size of the shoreline change curve (n = 147). The climate indices and shoreline datasets were split into two different datasets based on IPO phase motivated by previous work that has shown IPO's significant modulation of ENSO (Power et al., 1999). Cross correlation analyses were then performed on the tidally-corrected shoreline distances and SOI, SAM, PDO, STR-P, and STR-L index values in Matlab R2017b software. The sample cross correlation function (*crosscorr*) available in the Econometrics toolbox was used to compute and plot the cross-correlation function (XCF) between the two univariate time series. The function returns the lag numbers used for XCF estimation (±20 months was the maximum lag used here), the cross

correlation coefficient scaled from -1 to 1 for each time lag, and the upper and lower cross-correlation confidence bounds defined as two standard deviations from the mean.

3.3 Results

A total of 147 shoreline positions were extracted for the 1996 to 2017 time period (average of 7 positions per year) resulting in a total of ~9,000 km of mapped historical shorelines. The Double Island rocky headland was omitted from all shoreline analyses as its shoreline consists predominantly of Tertiary volcanics. The DSAS Shoreline Change Envelope (SCE) technique shows a wide range of total shoreline movement ranging between 37.75 and 212.5 m across the study area (Figure 3.4a). Two narrow regions show anomalously high SCE values: the shorelines within the Double Island Point headland shadow zone (180.1 m) and along the Great Sandy Strait Inlet (212.5 m). These areas were omitted from the climate analyses as they are likely affected by highly dynamic, localized effects such as ebb tidal deltas and wave diffraction/refraction around the bordering Double Island Point headland. The two sandy, open coast shorelines, Rainbow Beach and Noosa North, which constitute most (54 km) of the 62 km shoreline show a similar magnitude of total horizontal shoreline movement (Figure 3.4b). The 17 km long, SE-NW aligned Rainbow Beach shoreline has a mean SCE value of 68.5 m with a standard deviation (SD) of 17.3 m. The 35 km long, SW-NE aligned Noosa North shoreline has a mean SCE value of 79.6 m and a SD of 12.8 m. Shoreline change curves were created for the Rainbow Beach Open Coast (RB; low SCE, southeast-northwest orientation) and the Noosa North Open Coast (NN; low SCE, southwest-northeast orientation).

The averaged distance from baseline measurement for each NN shoreline shows a statistically significant negative correlation to the tide height at the time of Landsat flyover. The distance from baseline increases (shoreline progrades) when the tide height decreases and vice versa ($R^2 = 0.23$ and p-value << 0.05; Figure 3.5). This correlation indicates that the shoreline positions needed to be corrected for horizontal shifts induced by vertical changes in water level resulting from variable tide stages at the time of Landsat flyover. The mean time difference in the occurrence of daily maximum low and high tides at the two locations in 2017 was determined to be 2 minutes. The mean vertical tide range difference on the same dates was found to only be 2.5% of the overall tide range (0.03 of the 1.1 m vertical tide range, Figure 3.6). The near identical low and high tide timing and vertical tide range at these two locations justified their combined use for shoreline corrections.

The seasonal intertidal widths as determined by equilibrium beach profiles are as follows: Summer: 34.5 m, Autumn: 34.5 m, Winter: 33.3 m, Spring: 32.6 m. The 147 shoreline positions were corrected for tidal fluctuations using these widths and the percentage of intertidal width exposed at the time of flyover based on time since the previous low or high tide. For example, a shoreline extracted from a Landsat image in acquired in January that correlated with the daily low tide was moved 34.5 m towards the baseline (landward) to account for the horizontal change forced by tides. The tidally-corrected shoreline change curves that are used to perform cross correlation analyses with the climate data are shown in Figure 3.7.

The IPO changed phases twice during the study time period: from positive to negative in about June 1998 and a switch back to positive in about March 2014 (Figure 3.8). This agrees well with other studies that have identified a negative IPO phase occurring during the 1998 to 2014 period (Gastineau et al., 2018). The presence and strength of statistical relationships between the two shoreline change trends and five climate indices within each IPO phase were assessed by performing cross correlation analyses (Table 3.3). Correlations were not performed for data prior to 1998 due to a paucity of shoreline sample points.

During the 1998-early 2014 negative IPO, cross correlations reveal that the SOI is the strongest correlated climate index to shoreline change when it lags the shoreline position by 2 months at both NN ($r = -0.42$; Figure 3.9a) and RB ($r = -0.39$; Figure 3.9b). The 95% confidence bounds for NN = ±0.22 and ±0.21 for RB. The PDO shows slightly lower yet still statistically significant positive correlation to both NN (2 month lag, $r = 0.34$) and RB (2 month lag, $r = 0.3$). The latitudinal position of the STR shows positive correlations just within the 95% confidence interval at both NN (lag = 1, $r = 0.28$) and RB (lag = 0, $r = 0.24$). Cross correlations between SAM and STR-P with NN revealed they are most correlated when the shoreline change lags climate, indicating no significant climate forcing. SAM and STR-P both showed correlation with RB during the negative IPO at a zero time lag with $r = -0.33$ and 0.35, respectively.

During the mid-2014 to mid-2017 positive IPO period, the position and intensity of the STR shows the only significant correlation to shoreline change, where the 95% confidence bounds for NN = ±0.33 and ±0.31 for RB. STR-P is most correlated when it

lags shoreline changes by 1 month at RB (r = 0.47; Figure 3.10a) and 0 months at NN (r = -0.53; Figure 3.10b). STR-L shows slightly lower yet still significant correlation when it lags RB by 4 months (r = -0.44; Figure 3.10c) and NN by 2 months (r = 0.39; Figure 3.10d). SOI shows no correlation to shoreline changes at either RB (lag = 7, r = -0.17; Figure 3.9c) or NN where the best correlated lag was the maximum allowed (20 months, r = -0.36; Figure 3.9d). Similar results were achieved for PDO, which shows the RB shoreline lagging PDO (lag = -8, r = 0.33) and NN lagging by 19 months (r = 0.41). SAM shows no statistically significant correlation at either NN (lag = 10, r = -0.28) or RB (lag = 7, r = -0.30).

3.4 Discussion

The coupling between phase changes of the El Niño-Southern Oscillation Index and wave climate has been well described for locations along the New South Wales coast (Goodwin, 2005; Harley et al., 2010; Mortlock and Goodwin, 2016; Ranasinghe et al., 2004; Short et al., 2000). Only recently has it been shown that there is a correlation between the two along the southeast Queensland coast. McSweeney and Shulmeister (2018) show that there is a 0.1 m increase in significant wave height and a 6° anti-clockwise rotation of the mean wave direction during periods of sustained (>6 month) La Niña phases (positive SOI values). Elevated wave heights and a more cross-shore wave attack (easterly wave direction incident on a north-south oriented beach) would be expected to generate significant shoreline erosion. This was observed at a decadal scale by McSweeney and Shulmeister (2018) who used scarce (> 5 years between images for 1996-2012) aerial photography to relate shoreline erosion (accretion) with La Niña (El Niño).

This work expands upon their results by taking advantage of historical Landsat imagery to create a high temporal resolution shoreline change curve. The 147 shoreline positions mapped over the 21 year study period here show that both of the open-coast shorelines do have a negative correlation to SOI as suggested by McSweeney and Shulmeister (2018), yet only during negative IPO phases. Observations of shoreline changes occurring at the timescale of SOI phases (~2.5 years) are made possible using high temporal resolution satellite imagery. Examples of these events include the historically strong El Niño event in 1997-98 and the observed ~40 m shoreline progradation and similar amplitude erosion immediately following during the extreme La Niña of 1998-1999 at both RB and NN (Figure 3.7).

The robust relationship established between shoreline change and SOI only during negative IPO phases agrees with previous work that has suggested IPO's modulation of ENSO (Folland et al., 2002; Power et al., 1999; Splinter et al., 2012). A strong correlation between the SOI and numerous climate variables such as rainfall and surface temperature was observed over eastern Australia only when SST in the tropical Pacific was lowered (negative IPO; Power et al., 1999). Furthermore, the location of the SPCZ has been shown to influence the impact of ENSO on wave climate in southeast Queensland. Splinter et al. (2012) observed that wave climate in the Tasman Sea is more influenced by ENSO when the SPCZ, which lies close to Fiji, moves closer to Australia. This only occurs during negative IPO phases. They theorized that the Tasman Sea wave climate is likely influenced by other climatic variables when the SPCZ is further away from Australia (positive IPO) and the ENSO relationship is weakened, but did not perform any analyses to determine

which indices become prevalent. Based on this previous work and the cross correlation statistics presented here, we theorize that the open coast shorelines at the CSM are predominantly controlled by ENSO during negative IPO phases when the SPCZ moves southwest towards Australia. Negative correlation between both NN and RB were established with SOI indicating that the shorelines retreat (prograde) during La Niña (El Niño) phases. This agrees with previous studies that have suggested a more erosive wave climate during La Niña phases as incident wave directions become more oblique (easterly) and Hs increases (McSweeney and Shulmeister, 2018).

During negative IPO, PDO is shown to be positively correlated to both NN and RB at a similar time delay as SOI. The signs (+/-) of the correlation between PDO and shoreline change would have been expected to be the same as SOI given that PDO and SOI phases typically match one another (Mantua and Hare, 2002; Verdon and Franks, 2006). This could potentially be explained by large-scale anomalies and trends in cyclone and anticyclone behavior in the Tasman Sea. Pezza et al. (2007) show that more (less) frequent but weaker (stronger) cyclones occur during the positive (negative) phase of PDO across the Southern Hemisphere. The authors note a “remarkable exception” to this trend in the Tasman Sea (Figure 3.12), where negative PDO is host to both more frequent and stronger cyclones with the opposite pattern during positive PDO holding true. Waves of notably higher amplitude would result from enhanced cyclone intensity during negative PDO and promote a more erosive shoreline state (concurrently with an underlying La Niña wave climate).

Both SOI and PDO become notably uncorrelated to shoreline changes during the positive IPO phase from April 2014 through the end of the study time period (December 2017). In their place, STR-P and STR-L become the strongest and only statistically significant correlated climate indices to the shoreline change dataset, at a time lag comparable to SOI and PDO during the negative IPO phase. Recent work by Mortlock and Goodwin (2015) has shown that variability in the sub-tropical ridge influences wave climate in the Tasman Sea. They observed that as the STR migrates south, there is an anti-clockwise rotation in incident wave direction during both the austral summer and winter seasons. They noted that under a more southeasterly wave climate, cross-shore sediment movement would become the dominant mode of transport due to a more shoreline-perpendicular wave attack. This shoreline response likely explains why NN and RB are anti-correlated with respect to STR-L as NN (positively correlated) erodes as STR-L decreases (moves south) while RB progrades (negatively correlated). The more southeasterly wave climate would directly impact the exposed, SW-NE oriented NN shoreline causing erosion and offshore transport of foreshore beach sediment. The SE-NW oriented RB shoreline compartment is aligned near parallel to the southeasterly wave climate and is sheltered by the protruding Double Island rocky headland that separates it from NN. In addition to RB not being exposed to direct cross-shore wave attack, the headland significantly disperses wave energy that likely allows sediment to be removed from nearshore bar systems and deposited onshore under a reduced energy state. A conceptual model that illustrates the relationships between IPO phase variability, primary climate drivers of shoreline change, and shoreline response is shown in Figure 3.11.

The relationship between the intensity of the sub-tropical ridge (STR-P) and wave climate has not been studied, although an association between Australian rainfall variability and STR-P has been observed. The drought-like conditions in southern Australia over the past decade is suggested to be related to a more intense STR rather than latitudinal variations of the high MSLP band (Larsen and Nicholls, 2009; Timbal and Drosdowsky, 2013). The underlying climatic cause of variability of the STR and subsequent rainfall are unknown and as such, insight into how STR-P potentially affects wave climate (and shorelines) cannot be made. Cross correlations established in this study suggest there is a strong link between the two and this should be a focus of further investigation. It's also clear from the results presented here that shoreline changes are governed by processes other than global and regional climate cycles as the strongest correlation between NN and STR-P ($r = -0.53$) only accounts for 28% of the variability. Local synoptic weather patterns (i.e. trade winds, East Coast Lows) have been shown to be key drivers of rainfall variability in QLD in conjunction with climate (Klingaman, 2012) and they likely have an influence on shoreline change as well. Future work can include the use of newer generation satellite data products (i.e. PlanetScope). The high spatial resolution afforded by these platforms (<5 m/pixel) could potentially produce a less noisy shoreline change curve and improve upon the correlations established in this study. Although, they have not been in orbit near long enough to study shoreline behavior during multiple IPO phases.

3.5 Conclusions

A multi-decadal, sub-annual temporal resolution shoreline change curve was produced for the open coast sections of one the world's oldest coastal dune systems, the Cooloola Sand Mass, located on the southeast coast of Queensland. Shorelines were observed to be horizontally shifted due to variable tide stages at the synchronous sampling time and tide data located near the study area were used to correct for these offsets. Seasonal intertidal widths ranged from 32.6 to 34.5 m and were determined by correlating the known vertical tide range of the study area to its corresponding offshore distance on equilibrium beach profiles constructed for each austral season. The tidally-corrected change curves show sudden and significant episodes of shoreline progradation and erosion in addition to decadal trends in shoreline position.

The statistical relationship between shoreline change at the two shoreline compartments and SOI, SAM, PDO, STR-P, and STR-L index values were quantified by performing cross correlations. The climate indices and shoreline datasets were split into two different datasets based on IPO phase motivated by previous work that has shown IPO's significant modulation of ENSO. SOI is the strongest correlated index to both RB and NN during the 1998-2014 negative IPO phase. During the 2014-2017 positive IPO, SOI becomes uncorrelated to the shoreline change dataset and the latitudinal position and intensity of the subtropical ridge (STR-P/L) shows the only statistically significant correlation to both shorelines. This bi-modal climate-shoreline relationship is likely related to IPO's modulation of ENSO and the position of the SPCZ. During positive IPO, the SPCZ moves northeast away from Australia and the impacts of ENSO are dampened, allowing STR to become the primary driver of wave climate and subsequent shoreline

change. During negative IPO, the SPCZ migrates closer to Australia and ENSO's impact on eastern Australia wave climate are amplified, which is reflected in the strong correlation statistics between SOI and RB/NN.

This study provides the first attempt at describing the relative influence of the four major climate cycles on shoreline change in southeast Australia. Previous studies have suggested that shoreline change in southeast Australia is primarily driven by ENSO variability. These studies were limited either by their spatial coverage (Ranasinghe et al., 2004) or temporal resolution of their shoreline dataset (McSweeney and Shulmeister, 2018), thus not allowing for a robust assessment on the correlation of climate variability directly with shoreline change on an inter-compartment scale. Using Landsat imagery allowed for near bi-monthly mapping of shoreline positions across two decades. This drastically improved spatial and temporal resolution shoreline dataset enabled statistical analyses and insight into sub-decadal correlations that were previously unfeasible due to small sample sizes.

The bimodal control on shoreline change governed by IPO phases described here is a significant advancement in our understanding of how the southeast Queensland Sand Island region coastline will respond to future predicted climate changes. The frequency of La Niña events and the rate of extreme La Niña events are expected to significantly increase in the 21st century due to global warming (Cai et al., 2015). In addition, the subtropical ridge is predicted to continue to move poleward under future warming scenarios due to the expansion of the Hadley circulation cell (Grose et al., 2015). Based on the shoreline-climate relationships described here, it can be expected that Noosa North and

possibly other SW-NE aligned coasts (i.e. Fraser and North Stradbroke Islands) will experience above average erosion during both positive and negative IPO phases. Meanwhile, Rainbow Beach and other SE-NW aligned coasts may also experience above average erosion during negative IPO when an enhanced La Niña is in effect, but could likely enter a stable to progradational state during positive IPO as STR continues to move south.

3.6 Acknowledgements

The authors would like to acknowledge the Geological Society of America for providing financial support. The work was partly supported by the ARC Discovery grant DP150101513. Landsat Surface Reflectance products courtesy of the U.S. Geological Survey. This work was carried out within the Joint Doctoral Program in Earthquake Science and Applied Geophysics at the University of California San Diego and San Diego State University. The paper was significantly improved by the comments of the three anonymous reviewers. Chapter 3, in full, is a reformatted version of the material as it appears in *Marine Geology*: Kelly, Joshua T., McSweeney, Sarah, Shulmeister, James, and Gontz, Allen. 2019. Bimodal climate control of shoreline change influenced by Interdecadal Pacific Oscillation variability along the Cooloola Sand Mass, Queensland, Australia. *Marine Geology*. v. 415C. Joshua Terence Kelly was the primary investigator and author of this paper.

Table 3.1: Seasonal significant wave height (H_s) and period (T_p) derived from a 31 year (1979-2009) wave record obtained from the NOAA WAVEWATCH III (WWIII) hindcast dataset and used to create equilibrium beach profiles.

Season (months)	**H_s (m)**	**T_p (sec)**
Summer (DJF)	1.93	8.44
Autumn (MAM)	2.17	8.91
zWinter (JJA)	1.91	8.92
Spring (SON)	1.63	8.12

Table 3.2: Explanation of technique for correcting DSAS shoreline distances for horizontal tidal fluctuations. Tide height at the time of Landsat flyover for 2014-2017 shoreline data based on the interpolation of Noosa Head low and high tide times. This method was not necessary for 1996-2013 as 10-minute archive data was available at Mooloolaba.

Tide record	**Flyover date & time (GMT)**	**Flyover date & time (AEST)**	**1st tide**	**Height (m)**	**2nd tide**	**Height (m)**	**Cycle time**	**Time since 1st tide**	
Mooloolaba	4/12/96 22:50	4/13/96 8:50	4:20	1.73	11:00	0.4			
Noosa Head	7/19/14 23:41	7/20/14 9:41	8:43	0.48	15:26	1.64	6:43	0:58	
	% Total tide	**Tide range**	**Flyover tide height (m)**	**ΔHigh tide (m)**	**% Total tide**	**Intertidal width exposed (m)**	**DSAS distance (m)**	**Corrected distance (m)**	**Normalized distance (m)**
Mooloolaba		1.33	0.58	1.15	0.864	27.2	1026.09	998.89	-1.11
Noosa Head	0.144	1.16	0.65	0.99	0.856	26.9	1008.55	981.65	-18.35

Table 3.3: Cross correlations between SOI, SAM, PDO, STR-P, and STR-L and the NN and RB shoreline distances from baseline during negative and positive IPO phases.

Shoreline compartment	Climate index	Lag (months)	Cross correlation	95% Confidence bounds
Negative IPO (1998-2014)				
NN	**SOI**	**2**	**-0.42**	**-0.22**
	SAM	-6	-0.31	-0.22
	PDO	2	0.34	0.22
	STR-P	-1	-0.27	-0.22
	STR-L	1	0.28	0.22
RB	**SOI**	**2**	**-0.39**	**-0.21**
	SAM	0	-0.33	0.21
	PDO	2	0.30	0.21
	STR-P	0	0.35	0.21
	STR-L	0	0.24	0.21
Positive IPO (2014-2017)				
NN	SOI	20	-0.36	-0.33
	SAM	10	-0.28	-0.33
	PDO	19	0.41	0.33
	STR-P	**0**	**-0.53**	**0.33**
	STR-L	2	0.39	0.33
RB	SOI	7	-0.17	-0.31
	SAM	7	-0.3	-0.31
	PDO	-8	0.33	0.31
	STR-P	**1**	**0.47**	**0.31**
	STR-L	4	-0.44	-0.31

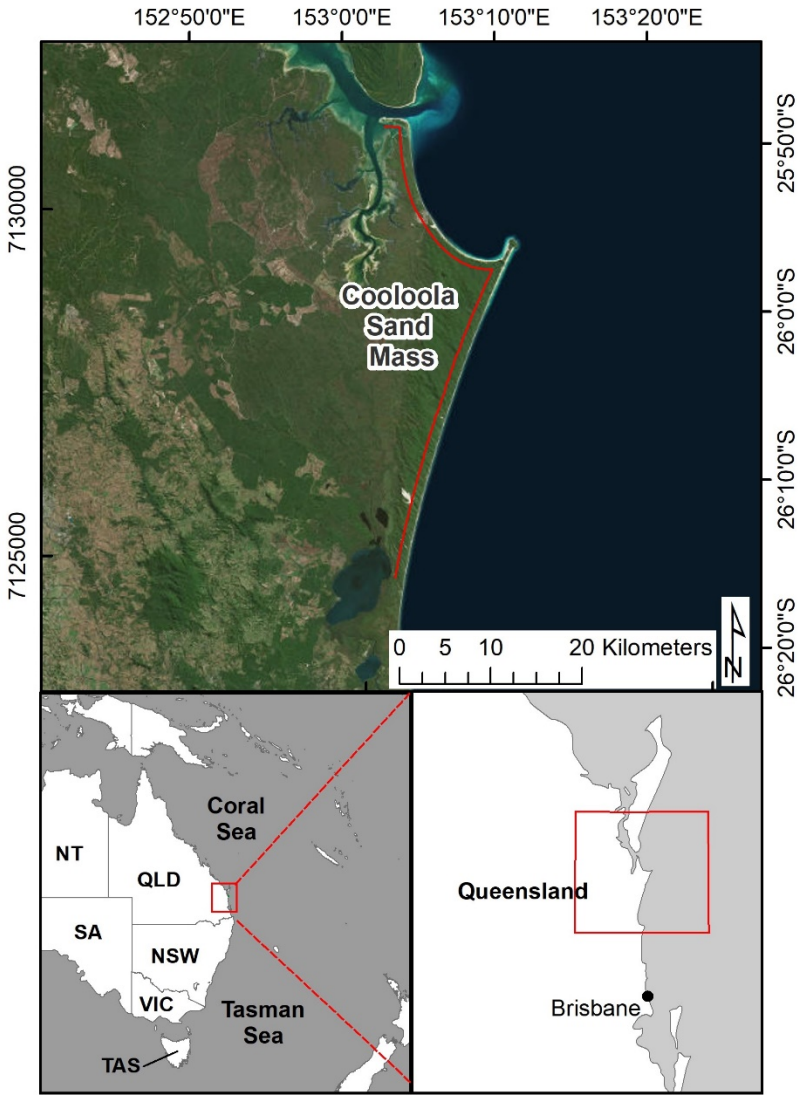

Figure 3.1: Location of the study area, Cooloola Sand Mass, Queensland, Australia. PlanetScope RGB band combination used as basemap.

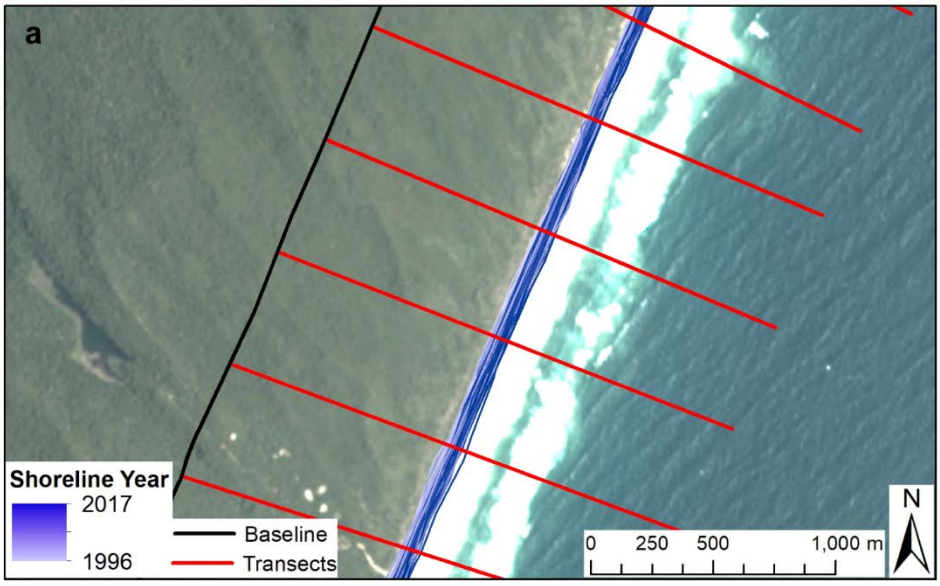

Figure 3.2: The required inputs for DSAS: vector shoreline positions, onshore baseline from which measurement transects are cast, and measurement transects cast every 500 m.

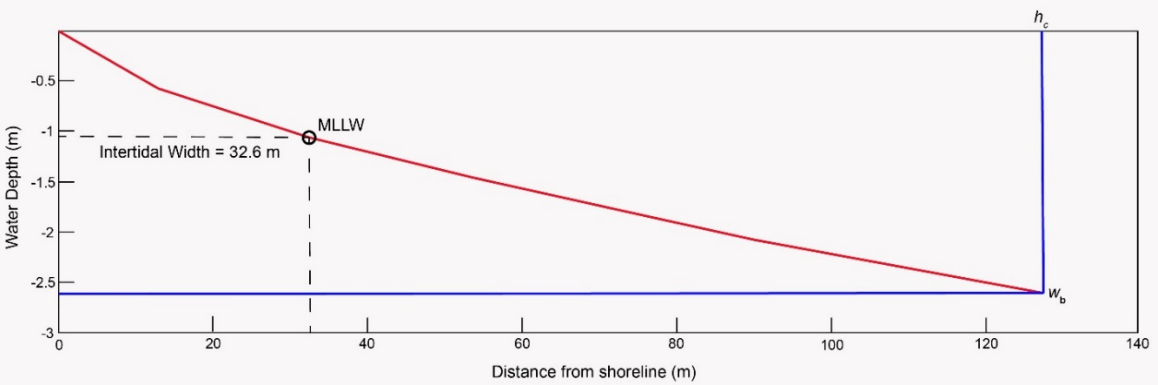

Figure 3.3: Extraction of the austral spring intertidal width from an equilibrium beach profile created using seasonal wave parameters.

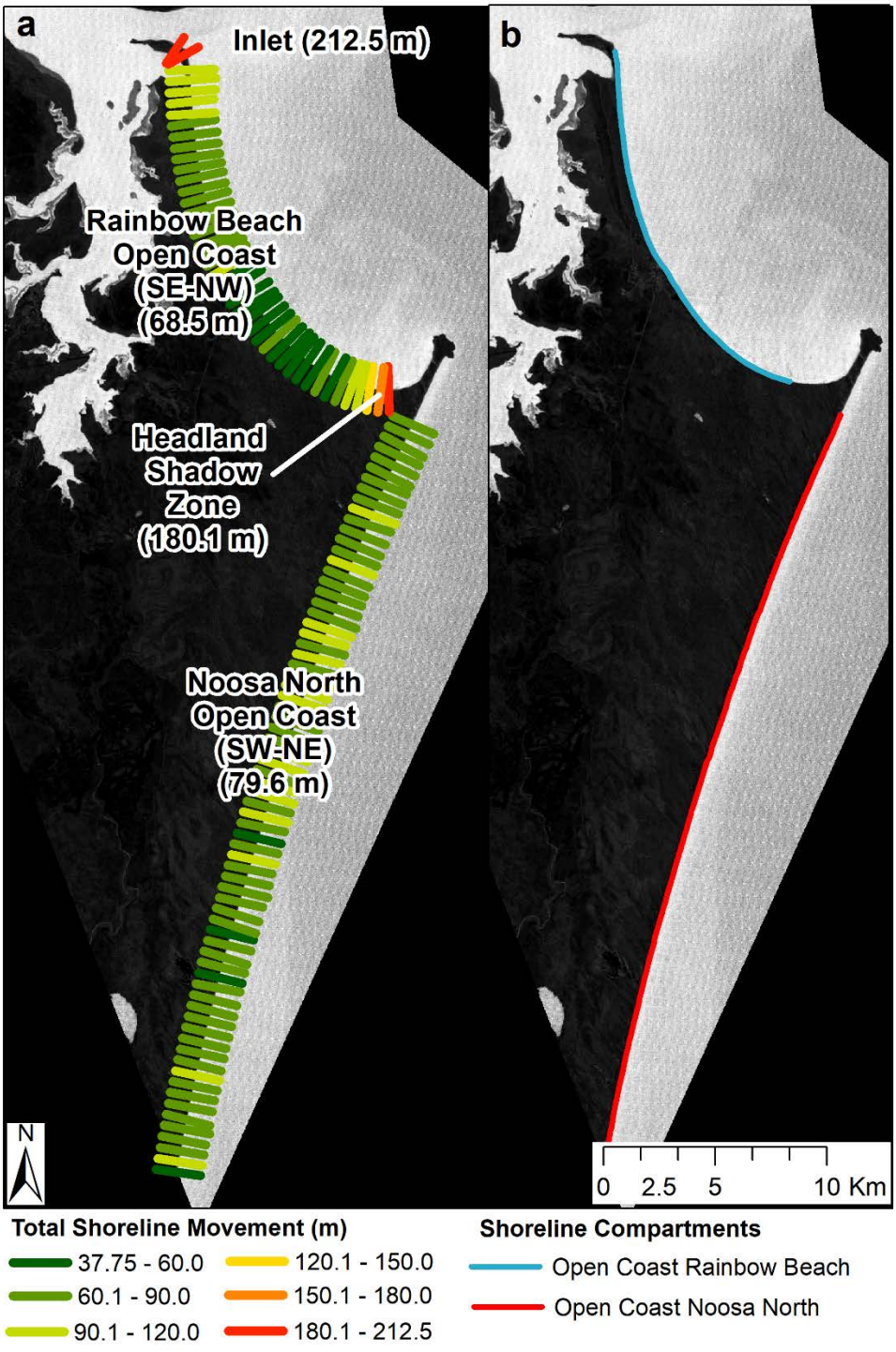

Figure 3.4: a. Total shoreline movement calculations determined by the Shoreline Change Envelope DSAS technique. **b.** Locations of the Rainbow Beach (RB) and Noosa North (NN) open coast shoreline compartments.

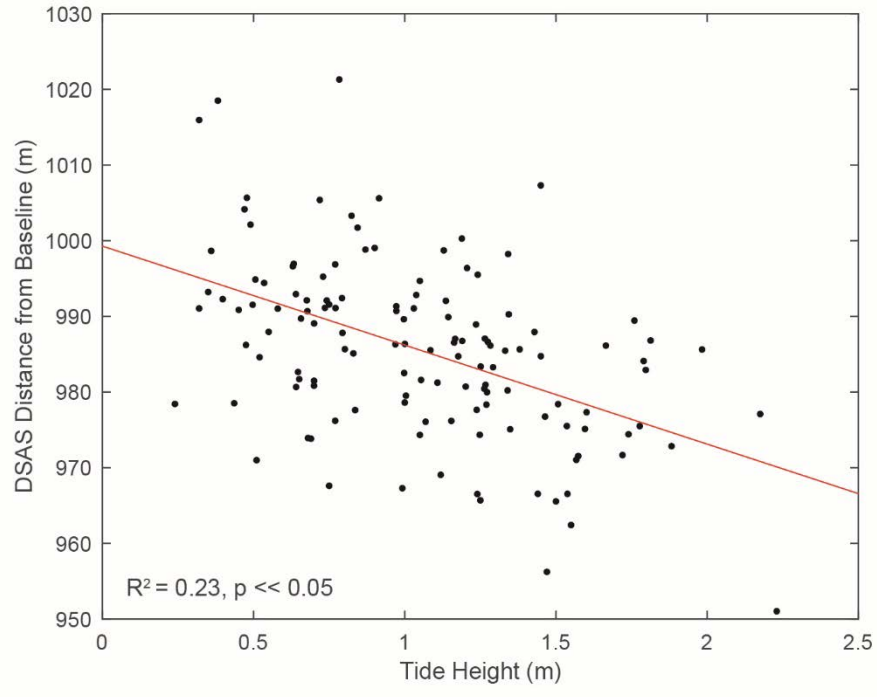

Figure 3.5: Averaged distance from baseline value for each Landsat shoreline (n = 147) plotted against the tide height during the time of Landsat flyover. Line of best fit and correlation statistics show significant negative correlation.

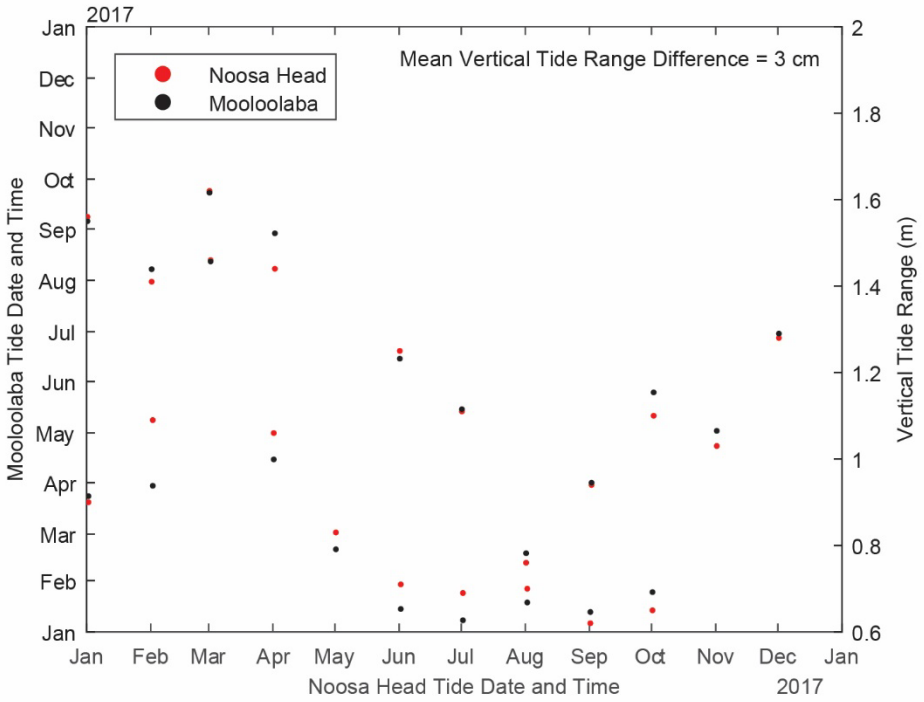

Figure 3.6: Comparison of the times and vertical tide ranges of daily low and high tides at the Noosa Head and Mooloolaba tide gauges.

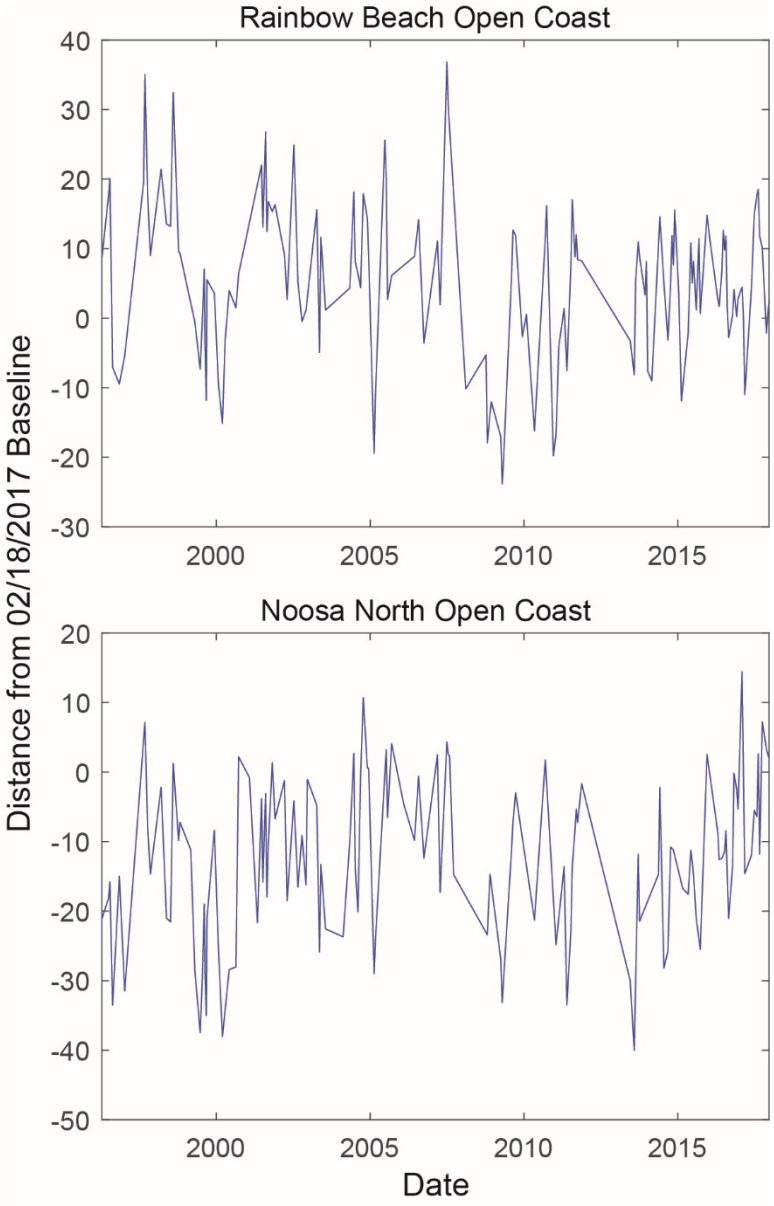

Figure 3.7: Historical shoreline change curves for the Rainbow Beach and Noosa North shoreline compartments created using tidally-corrected Landsat-derived shoreline position data.

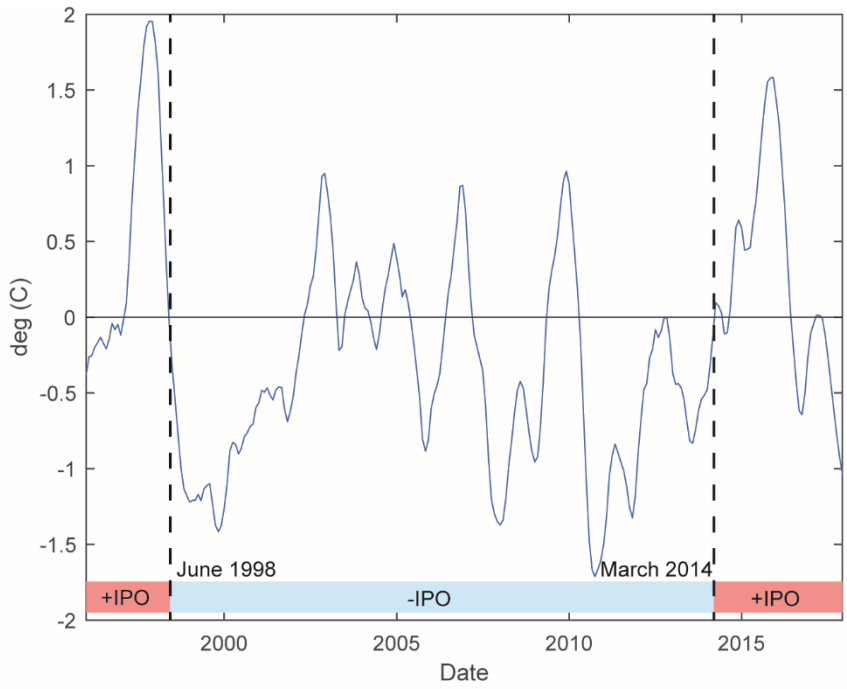

Figure 3.8: 3 month averaged Tripole Index for the Interdecadal Pacific Oscillation data during the study time period and identification of dates of phase changes.

o

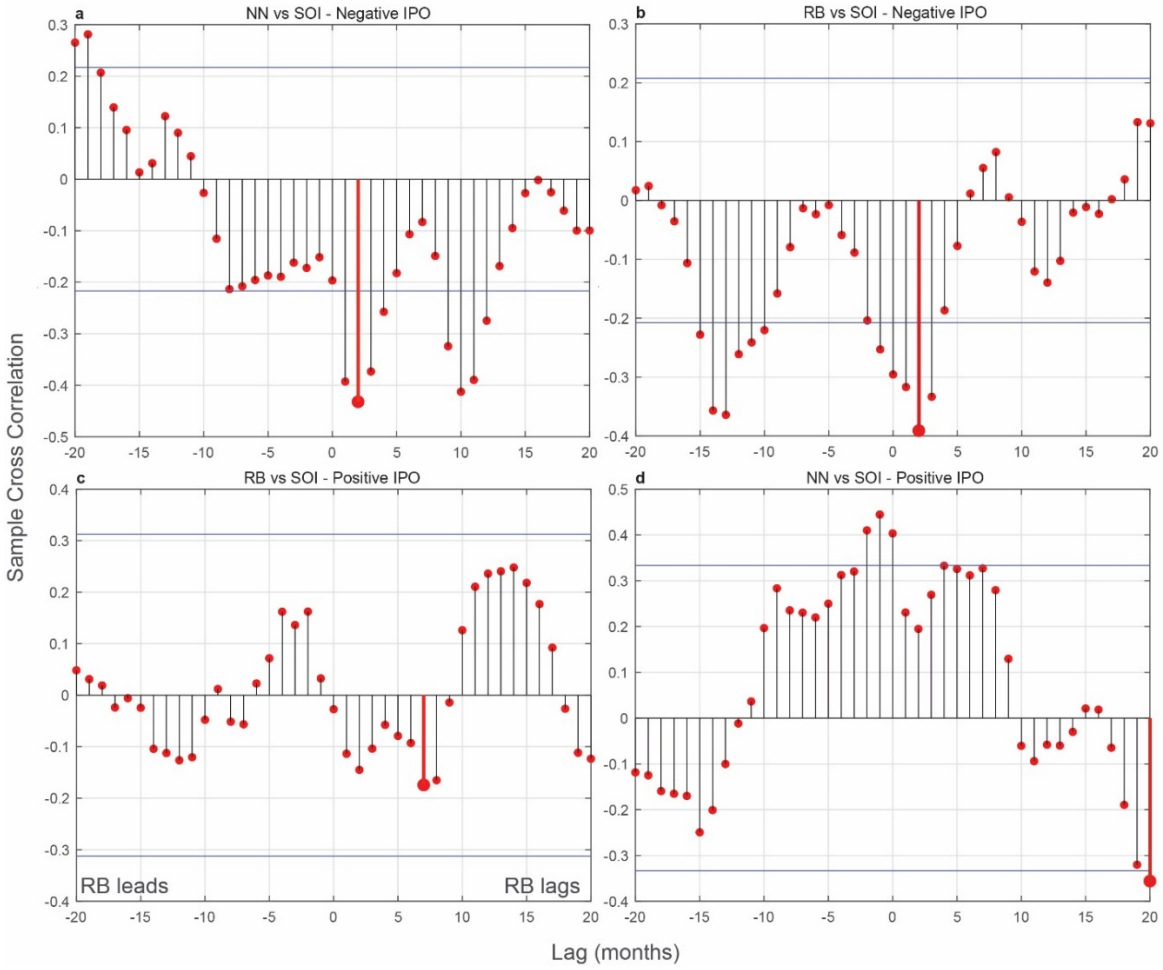

Figure 3.9: Cross correlation analyses between Southern Oscillation Index and **a.** Noosa North (NN) during negative Interdecadal Pacific Oscillation (IPO) **b.** Rainbow Beach (RB) during negative IPO **c.** RB during positive IPO **d.** NN during positive IPO. Red line indicates time lag at which maximum correlation occurs.

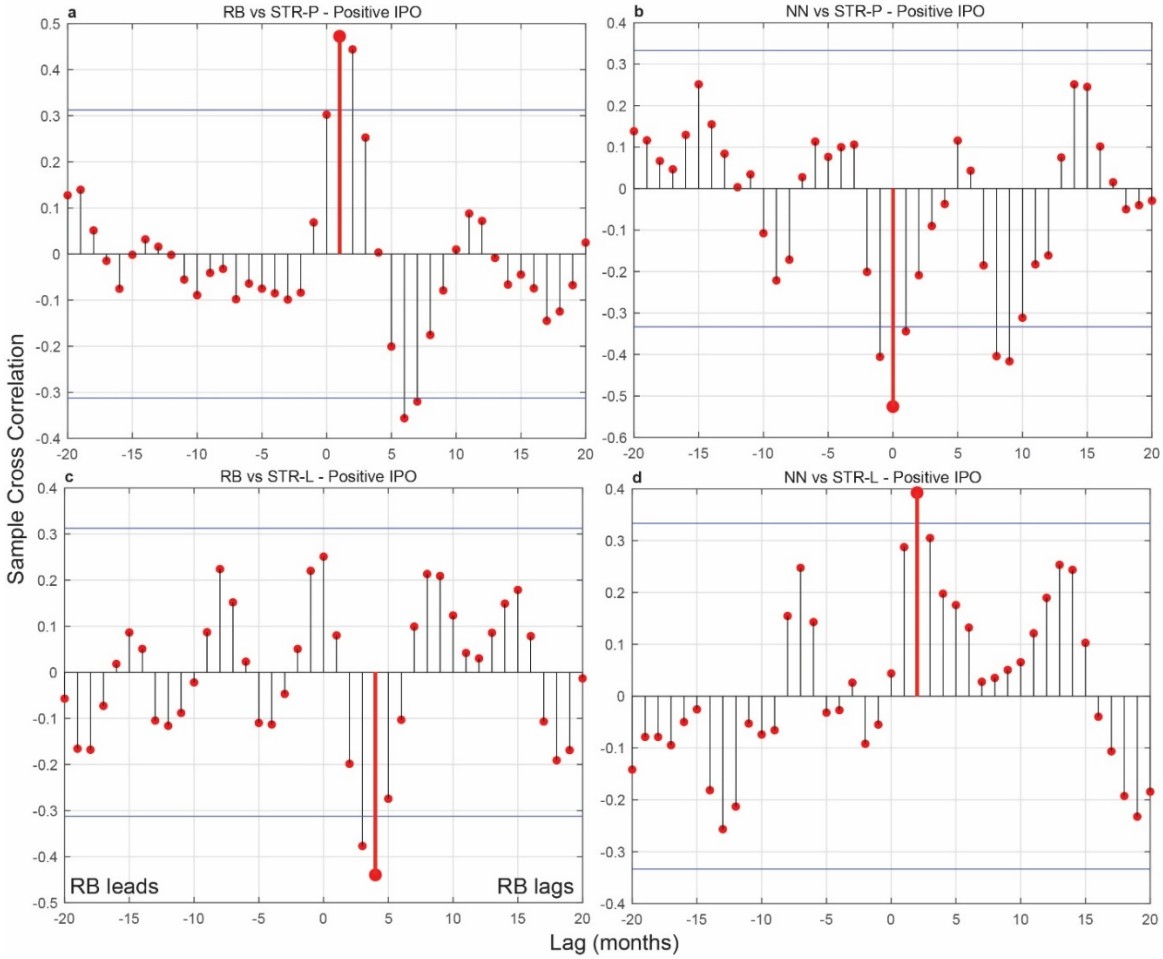

Figure 3.10: Cross correlation analyses occurring during positive Interdecadal Pacific Oscillation between a. Rainbow Beach and Subtropical Ridge-Pressure (STR-P) b. Noosa North (NN) and STR-P c. Rainbow Beach (RB) and Subtropical Ridge-Latitude (STR-L) d. NN and STR-L. Red line indicates time lag at which maximum correlation occurs.

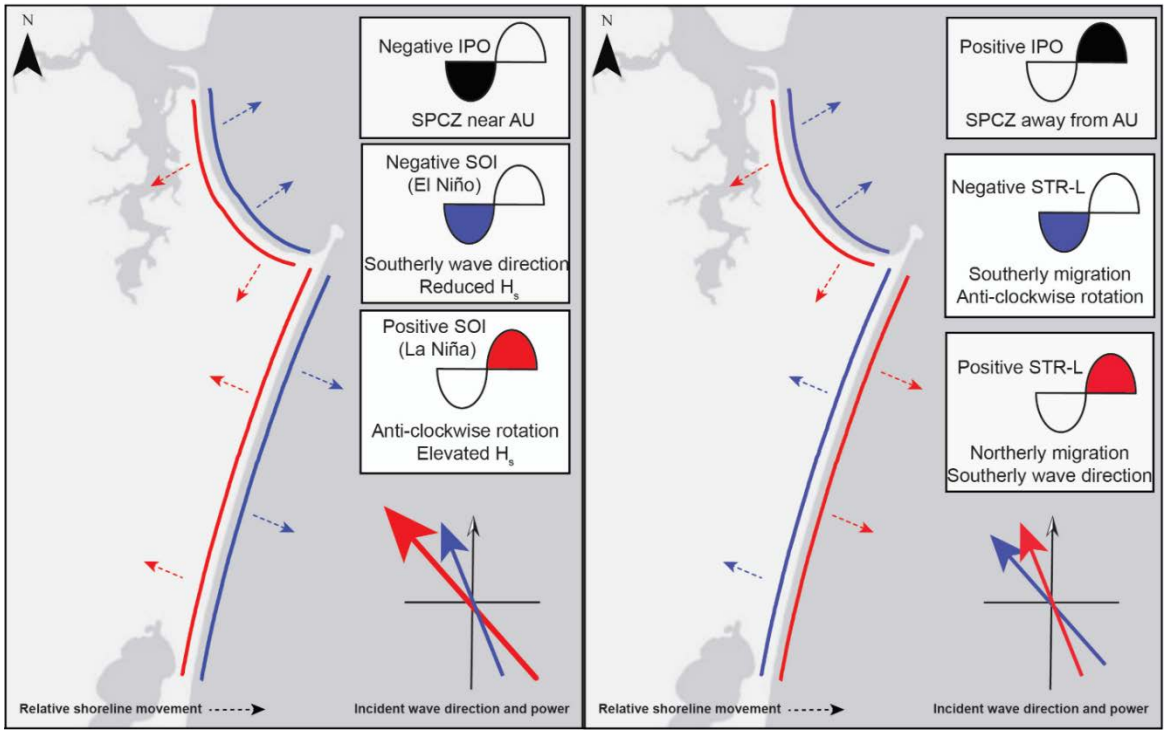

Figure 3.11: a. Shoreline response to Southern Oscillation Index (SOI) phase variability during negative Interdecadal Pacific Oscillation (IPO) phases. The incident wave direction and power during each SOI phase are illustrated by arrow size and color (SOI wave climate of McSweeney and Shulmeister, 2018 used here) and the corresponding shoreline response is indicated by the identical color. **b.** Shoreline response to the latitudinal variability of the Subtropical Ridge during positive IPO phases. Wave climate changes in response to Subtropical Ridge-Latitude variability from Mortlock and Goodwin (2015).

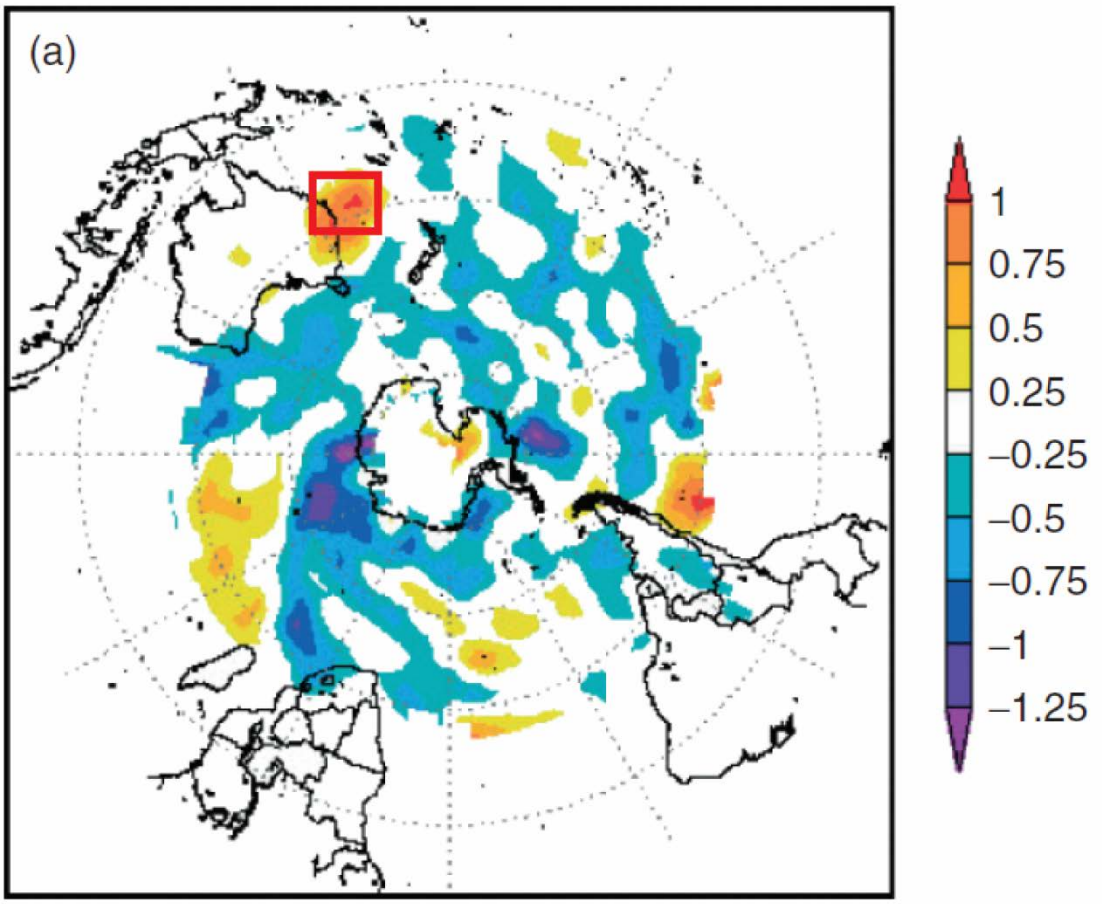

Figure 3.12: Cyclone pressure (hPa) anomalies across the Southern Hemisphere during negative Pacific Decadal Oscillation (PDO) phases (adapted from Pezza et al., 2007). Note the "remarkable exception" in the Tasman and Coral Seas (red square), which are host to more frequent and intense cyclones during negative PDO phases.

References

Almonacid-Caballer, J., Sánchez-García, E., Pardo-Pascual, J.E., Balaguer-Beser, A.A., Palomar-Vázquez, J., 2016. Evaluation of annual mean shoreline position deduced from Landsat imagery as a mid-term coastal evolution indicator. Marin Geology, 372, 79–88. https://doi.org/10.1016/J.MARGEO.2015.12.015

Australian Government., 2009. Climate change risks to Australia's coast - A first pass national assessment. Canberra: Australian Department of Climate Change.

Barnard P.L., Short A.D., Harley M.D., Splinter K., Vitousek S., Turner I., Allan J., Banno M., Bryan K., Doria A., Hansen J., Kato S., Kuriyama Y., Randall-Goodwin E., Ruggiero P., Walker P., Heathfield D., 2015. Coastal vulnerability across the Pacific dominated by El Niño/Southern Oscillation. Nature Geoscience, 8, 801-807. https://doi.org/10.1038/ngeo2539

BBW, 1985. Elevated ocean levels : storms affecting N.S.W. coast, 1880-1980 / prepared by Blain Bremner & Williams Pty Ltd in conjunction with Weatherex Meteorological Services Pty Ltd. - Version details - Trove [WWW Document]. URL https://trove.nla.gov.au/work/18400326?q&versionId=21595380 (accessed 6.15.18).

Birkemeier, W.A., 1985. Field Data on Seaward Limit of Profile Change. Journal of Waterway, Port, Coastal, and Ocean Engineering, 111, 598–602. https://doi.org/10.1061/(ASCE)0733-950X(1985)111:3(598)

Boak, E.H. and Turner, I.L., 2005. Shoreline Definition and Detection: A Review. Journal of Coastal Research, 21(4), 688-703. https://doi.org/10.2112/03-0071.1

Boyd, R., Ruming, K., Goodwin, I., Sandstrom, M., Schröder-Adams, C., 2008. Highstand transport of coastal sand to the deep ocean: A case study from Fraser Island, southeast Australia. Geology, 36, 15. https://doi.org/10.1130/G24211A.1

Bruun, P., 1954. Coast Erosion and the Development of Beach Profiles. Technical Memorandum No. 44, Beach Erosion Board.

Cai, W., Wang, G., Santoso, A., McPhaden, M.J., Wu, L., Jin, F.-F., Timmermann, A., Collins, M., Vecchi, G., Lengaigne, M., England, M.H., Dommenget, D., Takahashi, K., Guilyardi, E., 2015. Increased frequency of extreme La Niña events under greenhouse warming. Nature Climate Change, 5, 132–137. https://doi.org/10.1038/nclimate2492

Church, J. A., Gregory, J. M., Huybrechts, P., Kuhn, M., Lambeck, K., Nhuan, M. T., Qin, D., Woodworth, P. L., 2001. Changes in Sea Level in: J.T Houghton, Y. Ding, D.J. Griggs, M. Noguer, P.J. Van der Linden, X. Dai, K. Maskell, and C.A. Johnson (eds.):

Climate Change 2001: The Scientific Basis: Contribution of Working Group I to the Third Assessment Report of the Intergovernmental Panel.

Church, J.A. and White, N.J., 2006. A 20th century acceleration in global sea-level rise. Geophysical Research Letters, 33. https://doi.org/10.1029/2005GL024826

Coelho, C., Silva, R., Veloso-Gomes, F., Taveira-Pinto, F., 2009. Potential effects of climate change on northwest Portuguese coastal zones. ICES Journal of Marin Science, 66, 1497–1507. https://doi.org/10.1093/icesjms/fsp132

Dean, R. G., 1991. Equilibrium beach profiles: characteristics and applications. Journal of Coastal Research, 7(1), 53-84.

Drosdowsky, W., 2005. The latitude of the subtropical ridge over Eastern Australia: The L index revisited. International Journal of Climatology, 25, 1291–1299. https://doi.org/10.1002/joc.1196

Ellerton, D., Rittenour, T., Miot da Silva, G., Gontz, A., Shulmeister, J., Hesp, P., Santini, T.C., Welsh, K.J., 2018. Late-Holocene cliff-top blowout activation and evolution in the Cooloola Sand Mass, south-east Queensland, Australia. The Holocene, 28, 1697–1711. https://doi.org/10.1177/0959683618788679

Fang, C., Wu, L., Zhang, X., 2014. The impact of global warming on the pacific decadal oscillation and the possible mechanism. Advances in Atmospheric Science, 31, 118–130. https://doi.org/10.1007/s00376-013-2260-7

Folland, C. K., Renwick, J. A., Salinger, M. J., Mullan, A. B., 2002. Relative influences of the Interdecadal Pacific Oscillation and ENSO on the South Pacific Convergence Zone. Geophysical Research Letters, 29(13), 21-1-21-4. https://doi.org/10.1029/2001GL014201

Gastineau, G., Friedman, A. R., Khodri, M., Vialard, J., 2018. Global ocean heat content redistribution during the 1998–2012 Interdecadal Pacific Oscillation negative phase. Climate Dynamics, https://doi.org/10.1007/s00382-018-4387-9

Gong, D. and Wang, S., 1999. Definition of Antarctic oscillation index. Geophysical Research Letters, 26, 459-462. https://doi.org/10.1029/1999GL900003

Goodwin, I, D., 2005. A mid-shelf, mean wave direction climatology for southeastern Australia, and its relationship to the El Niño-Southern Oscillation since 1878 A.D. International Journal of Climatology, 25(13), 1715-1729. https://doi.wiley.com/10.1002/joc.1207

Gorelick, N., Hancher, M., Dixon, M., Ilyushchenko, S., Thau, D., Moore, R., 2017. Google Earth Engine: Planetary-scale geospatial analysis for everyone. Remote Sensing of the Environment, 202, 18–27. https://doi.org/10.1016/J.RSE.2017.06.031

Grose, M., Timbal, B., Wilson, L., Bathols, J., Kent, D., 2015. The subtropical ridge in CMIP5 models, and implications for projections of rainfall in southeast Australia. Australian Meteorological and Oceanographic Journal, 65, 90-106.

Hall, A. and Visbeck, M., 2002. Synchronous Variability in the Southern Hemisphere Atmosphere, Sea Ice, and Ocean Resulting from the Annular Mode. Journal of Climate, 15, 3043–3057. https://doi.org/10.1175/1520-0442(2002)015<3043:SVITSH>2.0.CO;2

Hallegatte, S., Green, C., Nicholls, R.J., Corfee-Morlot, J., 2013. Future flood losses in major coastal cities. Nature Climate Change, 3, 802–806. https://doi.org/10.1038/nclimate1979

Harley, M.D., Turner, I.L., Short, A.D., Ranasinghe, R., 2010. Interannual variability and controls of the Sydney wave climate. International Journal of Climatology, 30(9), 1322-1335. https://doi.org/10.1002/joc.1962

Harris, P.T., Heap, A.D., Bryce, S.M., Porter-Smith, R., Ryan, D.A., Heggie, D.T., 2002. Classification of Australian Clastic Coastal Depositional Environments Based Upon a Quantitative Analysis of Wave, Tidal, and River Power. Journal of Sedimentary Research, 72, 858–870. https://doi.org/10.1306/040902720858

Hemer, M.A., McInnes, K.L., Ranasinghe, R., 2013a. Projections of climate change-driven variations in the offshore wave climate off south eastern Australia. International Journal of Climatology, 33, 1615–1632. https://doi.org/10.1002/joc.3537

Hemer, M.A., Church, J.A., Hunter, J.R., 2010. Variability and trends in the directional wave climate of the Southern Hemisphere. International Journal of Climatology, 30, 475-491. https://doi.org/10.1002/joc.1900

Hemer, M.A., Katzfey, J., Trenham, C.E., 2013b. Global dynamical projections of surface ocean wave climate for a future high greenhouse gas emission scenario. Ocean Modelling, 70, 221–245. https://doi.org/10.1016/J.OCEMOD.2012.09.008

Hemer, M.A., McInnes, K.L., Ranasinghe, R., 2012. Climate and variability bias adjustment of climate model-derived winds for a southeast Australian dynamical wave model. Ocean Dynamics, 62, 87–104. https://doi.org/10.1007/s10236-011-0486-4

Kalnay, E., Kanamitsu, M., Kistler, R., Collins, W., Deaven, D., Gandin, L., Iredell, M., Saha, S., White, G., Woollen, J., Zhu, Y., Leetmaa, A., Reynolds, R., Chelliah, M., Ebisuzaki, W., Higgins, W., Janowiak, J., Mo, K.C., Ropelewski, C., Wang, J., Jenne, R., Joseph, D., Kalnay, E., Kanamitsu, M., Kistler, R., Collins, W., Deaven, D., Gandin, L., Iredell, M., Saha, S., White, G., Woollen, J., Zhu, Y., Chelliah, M., Ebisuzaki, W., Higgins, W., Janowiak, J., Mo, K.C., Ropelewski, C., Wang, J., Leetmaa, A., Reynolds, R., Jenne, R., Joseph, D., 1996. The NCEP/NCAR 40-Year Reanalysis Project. Bulletin of the American Meteorological Society, 77, 437–471. https://doi.org/10.1175/1520-0477(1996)077<0437:TNYRP>2.0.CO;2

Kelly, J. T. and Gontz, A. M., 2018. Using GPS-surveyed intertidal zones to determine the validity of shorelines automatically mapped by Landsat water indices. International Journal of Applied Earth Observation and Geoinformation, 65, 92-104. https://doi.org/10.1016/j.jag.2017.10.007

Kidson, J. W., 1999. Principal modes of Southern Hemisphere low-frequency variability obtained from NCEP–NCAR reanalyses. Journal of Climate, 12, 2808–2830. https://doi.org/10.1175/1520-0442(1999)012<2808:PMOSHL>2.0.CO;2

Klingaman, N. P., 2012. A literature survey of key rainfall drivers in Queensland, Australia: Rainfall variability and change. Rainfall in Queensland, Part 1, Office of Climate Change, QCCCE Research Rep., 37 pp.

Larsen, S. H. and Nicholls, N., 2009. Southern Australian rainfall and the subtropical ridge: Variations, interrelationships, and trends. Geophysical Research Letters, 36(8). https://doi.org/10.1029/2009GL037786

Mantua, N.J. and Hare, S.R., 2002. The Pacific Decadal Oscillation, Journal of Oceanography, 58, 35-44.

Mantua, N.J., Hare, S.R., Zhang, Y., Wallace, J.M., Francis, R.C., 1997. A Pacific Interdecadal Climate Oscillation with Impacts on Salmon Production. Bulletin of the American Meteorological Society, 78, 1069-1079. https://doi.org/10.1175/1520-0477(1997)078<1069:APICOW>2.0.CO;2

Marshall, G.J., 2003. Trends in the Southern Annular Mode from Observations and Reanalyses. Journal of Climate, 16, 4134–4143. https://doi.org/10.1175/1520-0442(2003)016<4134:TITSAM>2.0.CO;2

Masek, J.G., Vermote, E.F., Saleous, N.E., Wolfe, R., Hall, F.G., Huemmrich, K.F., Gao, F., Kutler, J., Lim, T.-K., 2006. A Landsat Surface Reflectance Dataset for North America, 1990–2000. IEEE Geoscience and Remote Sensing Letters, 3, 68–72. https://doi.org/10.1109/LGRS.2005.857030

McSweeney, S. and Shulmeister, J., 2018. Variations in wave climate as a driver of decadal scale shoreline change at the Inskip Peninsula, southeast Queensland, Australia. Estuarine Coastal Shelf Science, 209, 56-69. 10.1016/j.ecss.2018.04.034

Mortlock, T. R. and Goodwin, I. D., 2015. Directional wave climate and power variability along the Southeast Australian shelf. Marine Geology, 98, 36-53. https://doi.org/10.1016/j.csr.2015.02.007

Mortlock, T. R. and Goodwin, I. D., 2016. Impacts of enhanced central Pacific ENSO on wave climate and headland-bay beach morphology. Continental Shelf Research, 120, 14-25. 10.1016/j.csr.2016.03.007

NCCARF, 2017. Climate change and sea-level rise based on observed data. National Climate Change Adaptation Research Facility, Gold Coast. Available from: https://coastadapt.com.au/climate-change-and-sea-level-rise-based-observed-data. Accessed 16 April 2018.

Nicholls, R.J., Hanson, S., Herweijer, C., Patmore, N., Hallegatte, S., Corfee-Morlot, J., Chateau, J., Muir-Wood, R., 2008. Ranking Port Cities with High Exposure and Vulnerability to Climate Extremes. OECD Environment Working Papers, No. 1, OECD Publishing, Paris. https://doi.org/10.1787/011766488208

O'Grady, J.G., McInnes, K.L., Colberg, F., Hemer, M.A., Babanin, A.V., 2015. Longshore wind, waves and currents: climate and climate projections at Ninety Mile Beach, southeastern Australia. International Journal of Climatology, 35, 4079-4093. doi:10.1002/joc.4268

Pardo-Pascual, J.E., Almonacid-Caballer, J., Ruiz, L.A., Palomar-Vázquez, J., Rodrigo-Alemany, R., 2014. Evaluation of storm impact on sandy beaches of the Gulf of Valencia using Landsat imagery series. Geomorphology, 214, 388–401. https://doi.org/10.1016/J.GEOMORPH.2014.02.020

Pezza, A. B., Simmonds, I., Renwick, J. A., 2007. Southern Hemisphere cyclones and anticyclones: Recent trends and links with decadal variability in the Pacific Ocean. International Journal of Climatology, 27, 1403-1419. DOI: 10.1002/joc.1477

Pittock, A.B., 1973. Global meridional interactions in stratosphere and troposphere. Quarterly Journal of the Royal Meteorological Society, 99, 424–437. https://doi.org/10.1002/qj.49709942103

Power, S., Casey, T., Folland, C., Colman, A., Mehta, V., 1999. Inter-decadal modulation of the impact of ENSO on Australia. Climate Dynamics, 15(5), 319-324. https://doi.org/10.1007/s003820050284

Ranasinghe, R., McLoughlin, R., Short, A., Symonds, G., 2004. The Southern Oscillation Index, wave climate, and beach rotation. Marine Geology, 204(3-4), 273-287. https://doi.org/10.1016/S0025-3227(04)00002-7

Roy, P. S. and Thom, B. G., 1981. Late Quaternary marine deposition in New South Wales and southern Queensland — An evolutionary model. Journal of the Geological Society of Australia, 28, 471-489. https://doi.org/10.1080/00167618108729182

Shand, T.D., Goodwin, I.D., Mole, M.A., Carley, J.T., Browning, S., Coghlan, I.R., Harley, M.D., Peirson, W.L., 2011. NSW Coastal Inundation Hazard Study: Coastal Storms and Extreme Waves, WRL Technical Report, UNSW Water Research Laboratory, Sydney, Australia

Short, A.D., Trembanis, A.C., Turner, I.L., 2000. Beach oscillation, rotation and the Southern Oscillation, Narrabeen Beach, Australia. In: Proceedings of the 27th International Coastal Engineering Conference. ASCE, Sydney, 2439-2452.

Short, A.D. and Trenaman, N.L., 1992. Wave Climate of the Sydney Region, an Energetic and Highly Variable Ocean Wave Regime. Australian Journal of Marine and Freshwater Research, 43, 765–91.

Slott, J.M., Murray, A.B., Ashton, A.D., Crowley, T.J., 2006. Coastline responses to changing storm patterns. Geophysical Research Letters, 33. https://doi.org/10.1029/2006GL027445

Smith, R.K. and Benson, A.P., 2001. Beach Profile Monitoring: How Frequent is Sufficient? Journal of Coastal Research, 34, 573-579. https://doi.org/10.2307/25736322

Splinter, K. D., Davidson, M. A., Golshani, A., Tomlinson, R., 2012. Climate Controls on longshore sediment transport. Continental Shelf Research, 48, 146-156. https://doi.org/10.1016/j.csr.2012.07.018

Tanimoto, Y., Hanawa, K., Toba, Y., Iwasaka, N., Tanimoto, Y., Hanawa, K., Toba, Y., Iwasaka, N., 1993. Characteristic Variations of Sea Surface Temperature with Multiple Time Scales in the North Pacific. Journal of Climate, 6, 1153–1160. https://doi.org/10.1175/1520-0442(1993)006<1153:CVOSST>2.0.CO;2

Tejan-Kella, M., Chittleborough, D., Fitzpatrick, R., Thompson, C., Prescott, J., Hutton, J., 1990. Thermoluminescence dating of coastal sand dunes at Cooloola and North Stradbroke Island, Australian Journal of Soil Research, 28, 465. https://doi.org/10.1071/SR9900465

Thom, B.G., Eliot, I., Eliot, M., Harvey, N., Rissik, D., Sharples, C., Short, A.D., Woodroffe, C.D., 2018. National sediment compartment framework for Australian coastal management. Ocean & Coastal Management, 154, 103–120. https://doi.org/10.1016/J.OCECOAMAN.2018.01.001

Thieler, E.R., Himmelstoss, E. A., Zichichi, J. L., Ergul, A., 2017. Digital Shoreline Analysis System (DSAS) version 4.0 - An ArcGIS extension for calculating shoreline change (ver. 4.4, July 2017): U.S Geological Survey Open-File Report 2008-1278, https://pubs.er.usgs.gov/publication/ofr20081278

Thompson, C., 1992. Genesis of podzols on coastal dunes in southern Queensland .I. Field relationships and profile morphology. Soil Research, 30, 593. https://doi.org/10.1071/SR9920593

Thompson, C., 1983. Development and weathering of large parabolic dune systems along the subtropical coast of eastern Australia. Zeitschrift fur Geomorphologie, Supplementband. 45, 205–225.

Timbal, B. and Drosdowsky, W., 2013. The relationship between the decline of Southeastern Australian rainfall and the strengthening of the subtropical ridge, International Journal of Climatology, 33(4), 1021-1034. https://doi.org/10.1002/joc.3492

Veevers, J. J., 2015. Beach sand of SE Australia traced by zircon ages through Ordovician turbidites and S-type granites of the Lachlan Orogen to Africa/Antarctica: a review. Australian Journal of Earth Science, 62(4), 385-408. https://doi.org/10.1080/08120099.2015.1053985

Vellinga, P., 1983. Predictive computational model for beach and dune erosion during storm surges. In: Proceedings, (ASCE), Specialty Conference on Coastal Structures '83, 806-81.

Verdon, D. C. and Franks, S. W., 2006. Long-term behaviour of ENSO: Interactions with the PDO over the past 400 years inferred from paleoclimate records. Geophysical Research Letters, 33(6). https://doi.org/10.1029/2005GL025052

Vermote, E., Justice, C., Claverie, M., Franch, B., 2016. Preliminary analysis of the performance of the Landsat 8/OLI land surface reflectance product. Remote Sensing of Environment, 185, 46–56. https://doi.org/10.1016/J.RSE.2016.04.008

Walker, J., Lees, B., Olley, J., Thompson, C., 2018. Dating the Cooloola coastal dunes of South-Eastern Queensland, Australia. Marine Geology, 398, 73–85. https://doi.org/10.1016/J.MARGEO.2017.12.010

Xu, H., 2006. Modification of normalised difference water index (NDWI) to enhance open water features in remotely sensed imagery. International Journal of Remote Sensing, 27, 3025-3033. https://doi.org/10.1080/01431160600589179

Chapter 4

Rapid Assessment of Shoreline Changes Induced by Tropical Cyclone Oma Using CubeSat Imagery in Southeast Queensland, Australia

Tropical Cyclone Oma impacted the Southeast Queensland coast of Australia in February 2019. Significant wave heights exceeding 10 m were further amplified by a king tide. Satellite remote sensing of pre- and post-Oma shoreline positions was performed as storm impacts hindered the ability to acquire field-based data. The high spatial and temporal resolution of PlanetScope imagery enabled mapping of the high water line (HWL), which was used as a shoreline indicator across 200 km of shoreline. Where this is the first attempt at using PlanetScope to map shoreline positions, the position uncertainty using this data was assessed. Comparison to a temporally coincident, LiDAR-derived mean high water (MHW) shoreline at a distant site showed an average horizontal offset of 9 m with the HWL shoreline. The Oma-impacted shoreline uncertainty ranged between ±13.86 and 23.28 m, primarily influenced by the geometric accuracy of the data used as well as the pixel size of the imagery and the horizontal offset between the HWL and MHW elevation. The Net Shoreline Movement (NSM) was calculated every 200 m along the study area using the Digital Shoreline Analysis System. Only transects with NSM values greater than the uncertainty of their associated shoreline compartment were used to assess change. The spatial distribution of erosion and accretion was similar across the SW-NE oriented shorelines as the southern ends of Fraser Island and the Cooloola Sand Mass eroded while their northern ends prograded. Wave data shows that the wave direction rapidly shifted 56° in an anti-clockwise direction during Oma. Wave propagation became primarily from the

SE and the direction of longshore transport likely turned northward, leading to the shoreline rotation observed in the imagery. This study demonstrates the significant improvement on assessments of regional-scale shoreline changes in the aftermath of an episodic event using new satellite products.

4.1 Introduction

Coastal systems worldwide are under threat from rising sea level (IPCC, 2014), coastal flooding (Kirshen et al., 2008), over development of the coastal zone (Harvey and Smithers, 2018), and increased storm numbers (Yue et al., 2019) and intensity (Putgatch et al., 2019). As a result, at least 24% of the world's sandy shorelines are eroding at rates surpassing 0.5 m/year (Luijendijk et al., 2018), a significant concern for the more than 100 million people living within 1 m of mean sea level (Zhang, Douglas, and Leatherman, 2004). Shoreline erosion impacts infrastructure (Laska et al., 2005), coastal sites of cultural heritage (Gontz et al., 2011; Maio, et al., 2012) and the recreation carrying capacity of the system (Cisneros et al., 2016). Thus, it is critical to understand how coastal systems respond to periods of extreme events.

New advances in satellite technology and geographic information systems provide new mechanisms to examine the impacts of episodic events. These techniques couple traditional methods used in aerial photography (Boak and Turner, 2005) and apply new techniques that take advantage of the multispectral capacity of satellite imagery (Kelly and Gontz, 2018; Kelly et al., 2019; van der Werff, 2019; Xu, 2018). High resolution satellite imagery (< 5 m/pixel) with high temporal resolution (daily) allows for an unprecedented capacity to track the impact of a single event over large areas without the logistical

planning, time and/or cost associated with flying low-altitude aerial imagery (Fellman, 2008), beach profiling (Andrade and Ferreira, 2006; Delgado and Lloyd, 2004), or UAS/UAV surveying (Colomina and Molina, 2014; Gonclaves and Henriques, 2015). The assessments can also be achieved from areas remote to the location of the event, increasing the safety of the individuals surveying the impact. The capacity for rapid assessment of the condition of the coastal system after a major event is critical for management, disaster relief, and safety.

Many early studies that examined the morphological changes to beaches after energetic storms relied on the rudimentary rod and level technique (Fisher and Stauble, 1977; Leatherman et al., 1977; Morton et al., 1995). This labor and time intensive survey method typically yielded spatially and temporally deficient datasets that required interpolation of location points between adjacent profiles (Morton, 1991; Overton and Fisher, 1996; Smith and Jackson, 1992). Aerial photography and Light Detection and Ranging (LIDAR) surveys are a significant improvement on manual surveying as they provide extensive spatial coverage from which quantification of shoreline changes can be assessed, albeit at a much higher acquisition cost which limits temporal resolution (Boak and Turner, 2005; Dolan, Hayden, and May, 1983; Zhang et al., 2005). More recently, freely available multispectral satellite imagery has been used to describe shoreline variability over time, although the moderate-resolution of Landsat (30 m) and Sentinel-2 (10 m) imagery limits the accuracy of the interpreted shoreline position and ability to detect smaller scale changes (Hagenaars et al., 2018; Pardo-Pascual et al., 2014).

These previous shoreline mapping techniques may be found unsuitable for rapid assessments of beach changes induced by high energy storms due to one or a combination of logistical difficulties, survey costs, and limited spatial resolution. The recent development of small, low-cost satellites known as “CubeSats” potentially represents the next step in assessing the impacts of hurricanes and other high energy storms on global shorelines in near-real time (<48 hours). The PlanetScope satellite constellation consists of 150 Triple-CubeSat satellites in a sun-synchronous orbit at an altitude of 475 km. These micro-satellites are equipped with a multispectral sensor that acquires imagery in the Blue, Green, Red, and Near-Infrared wavelength spectrums with a Ground Sample Distance of 3.7 m. Owing to the large number of satellites in orbit, the PlanetScope constellation has been collecting repeat daily coverage of the earth since early 2017. This revelation in satellite technology alleviates the previous tradeoff between high temporal and spatial resolution using a single platform (i.e. Landsat). The daily, 3.7 m multispectral imagery represents a significant improvement on Landsat’s 30 m imagery acquired in 16 day intervals that has been frequently used to assess shoreline changes (Almonacid-Caballer et al., 2016; Kelly et al., 2019) and could provide much greater insight into storm-induced shoreline changes.

The true definition of a “shoreline” is the physical boundary between land and water (Dolan et al., 1980) and a large number of shoreline indicators have been used to delineate its position and track changes over time (Boak and Turner, 2005). The most commonly used shoreline indicator has been the high water line (HWL) as it is easily identifiable in the field as well as in aerial photography and very-high resolution

commercial satellite imagery (Anders and Byrnes, 1991; Dolan et al., 1980; Moore, 2000; Pajak and Leatherman, 2002). It is identified as the color contrast between the wet intertidal and dry supratidal beach sediment left by the maximum wave runup of the previous high tide (Anders and Byrnes, 1991; Moore, Ruggiero, and List, 2006; Zhang et al., 2002). The instantaneous high water line imaged by aerial and space-borne platforms does not consider the prevailing wind, wave, and tide conditions at the time of capture (Boak and Turner, 2005). Elevated wind speeds and wave heights have been shown to horizontally offset the HWL and other shoreline indicators by tens of meters, particularly on gently sloping beaches (Thieler and Danforth, 1994).

4.1.1 History of Cyclones

Cyclonic storms are a significant threat to coastal environments located within the tropical to subtropical zone. The storms are common in the southwestern North Atlantic and Caribbean oceans as well as the southeastern and southwestern North Pacific Ocean (Bengtsson, Hodges, and Roecker, 2006). In eastern Australia, evidence of large-scale erosion events, like those associated with hurricane or cyclone strikes, was reported from a North Stradbroke Island ground penetrating radar survey that showed storm scarps in excess of 2 m occurring on a repetitive basis (Gontz et al., 2013). Other studies have shown similar results from beaches throughout Australia (e.g. Forsyth et al., 2010; Knott et al., 2009; May et al., 2018). Levin (2011) and Levin, Neil, and Syktus (2014) showed that cyclone activity was responsible for controlling blowout development and renewed activity on the large sand islands. Sweeney and Shulmeister (2018) demonstrated that the shoreline of Rainbow Beach in southeast Queensland has experienced large erosive events using

repeat aerial photography and linked the changes to El Niño-Southern Oscillation. However, their study did not include any pre- and post-storm imagery and thus, erosive episodes could not be linked to specific events. Kelly et al. (2019) expanded their work using Landsat imagery over 25 years and showed that long term shoreline change at the Cooloola Sand Mass is controlled by variability in the Interdecadal Pacific Oscillation (IPO). However, Landsat imagery does not have high-spatial resolution and thus impacts of individual storms also could not be discerned, unless the event resulted in shoreline migration of more than ~15 m. Other documented shoreline changes occurring in response to large-scale storm events not only include erosion and progradation, but washover fan development (May et al., 2017; Williams, 2015) and new inlet formation (FitzGerald and Pendleton, 2002; Maio et al., 2014).

4.1.2 Tropical Cyclone Oma

Tropical Cyclone Oma (Oma) reached tropical cyclone status on 12 Feb 2019 at 0000 GMT. The storm was then located at 14° S, 164.5° E, approximately 290 km northwest of Vanuatu. Over the next nine days, the storm slowly moved generally south-southwest toward the eastern coast of Australia (Figure 4.1). During this time, the storm's intensity varied from tropical storm to Category 1 and reached Category 2 on 20 February 2019 at 0400 GMT. On 22 February 2019 at 0000 GMT, the storm intensity had weakened to a Category 1 storm and the models suggested the storm would stay well offshore of the southeast Queensland coast. In response, the tropical cyclone warning for all sections of the southeast coast of Queensland and the northwest coast of New South Wales (NSW) was canceled. However, as the storm center was approximately 600 km east of the northern

section of Fraser Island, hazard surf and high tide warnings were “still in effect for the next several days” as the storm was expected to intensify to a Category 2, slow, turn north and remain offshore (BOM, 2019). On 22 February 2019, the wave monitoring buoy 50 km east of Point Lookout recorded a 16 m wave and a significant wave height of 10 m. Ultimately, the storm turned east and north in a sharp buttonhook, moving the storm center farther from the Queensland coast. The storm was off the coast of Queensland for nearly five days.

Coupled with Oma, the southeast coast of Queensland experienced a king tide on 21 February 2019. Elevated high tide levels resulted in flooding in Brisbane along the Brisbane River (Courier News, 2019a), beach erosion near Orchid Rock on Fraser Island (Personal Commination, 2019), and a potential for Bribie Island to breach (Courier News, 2019b). However, the storm did not approach the coast close enough to cause a rainfall event. No precipitation was recorded at the Brisbane Airport (BOM, 2019). While Oma did not make landfall, or approach the coast closer than 450 km, the situation developed conditions that were favorable for large-scale coastal erosion.

4.1.3 Study Site

The coast of southeast Queensland is dominated by large sand islands and mainland attached dune fields (Ellerton et al., 2018) that have formed as a result of an extensive longshore transport system that originates in New South Wales (Boyd et al., 2008). Fraser Island (FI), the Cooloola Sand Mass (CSM), and the Sunshine Coast (SC) make up a significant part of this region and represent over 200 km of predominantly sandy coastline (Figure 4.1). These sediments are sourced from the Triassic Hawkesbury sandstone unit

located in the Sydney Basin (Wasantha and Ranjith, 2014) and are mostly quartz with less than 2% heavy minerals and little to no carbonate (Thompson, 1983). The CSM is suggested to be one of the world's oldest continuous coastal dune fields based on thermoluminescence dating of sand grains revealing an age of 700 ka (Tejan-Kella et al., 1990; Walker et al., 2018). The mostly open coast shorelines of the study area are wave-dominated and micro-tidal (Harris et al., 2002) and are influenced by a variety of synoptic weather patterns that operate in and around the neighboring Coral Sea (Harley et al., 2010). These weather patterns (i.e. East Coast Lows, Tropical Cyclones, etc.) interact and influence a seasonal wave climate that is highly variable with respect to wave heights and direction (Hemer, McInnes, and Ranasinghe, 2013). Recent work has shown that long-term CSM shoreline dynamics are predominantly controlled by IPO phase variability (Kelly et al., 2019).

4.1.4 Purpose

The purpose of this study is twofold: to understand the capabilities and limitations of using high spatial and temporal resolution PlanetScope imagery to map shoreline positions and to quantitatively assess shoreline changes induced by Tropical Cyclone Oma in southeast Queensland in February 2019.

4.2 Methods

PlanetScope (PS) Analytic Ortho Scene (Level 3B) products were acquired from Planet Labs, Inc. directly. These imagery products are orthorectified using ground control points and fine Digital Elevation Models to achieve <10 m RMSE positional accuracy. Further geometric corrections of the Level 3B imagery are performed using sensor

telemetry and attitude telemetry of the spacecraft. The Analytic Ortho Scene products are radiometrically corrected for any sensor artifacts and conversion to absolute radiometric values based on calibration coefficients, which are continuously updated with on-orbit calibration techniques (Planet, 2017). The Level 3B data are provided as both at-sensor radiance and surface reflectance products, of which surface reflectance was used because of the removal of atmospheric artifacts and improved consistency between images acquired at different times. Surface reflectance is calculated using MODIS near-real time aerosol optical depth, ozone, and water vapor parameters sourced from the MOD09CMA and MOD09CMG datasets. The products are supplied in a WGS84 Universal Transverse Mercator coordinate system (Zone 56S for this study area).

Visual inspection of all available PS Analytic scenes in the study area was required to identify scenes with suitable cloud-free coverage along the shoreline area. Data were acquired pre- and post-Oma as close as possible to the storm date, limited primarily by extensive cloud coverage (to be expected during a tropical cyclone). Although no entirely cloud-free days were found, mostly clear days were observed on February 15 and 19, 2019 (pre-Oma) and February 27 (immediately post-Oma). Georectified Level 3B data products were acquired for the study area on these dates and used for shoreline delineation. The PS images were imported into ArcGIS Pro and resampled using Cubic Convolution, which determines each cell value based on fitting a smooth curve through the 16 nearest input cell centers. The red (band 3), green (band 2), and blue (band 1) layers contained within each 4-band product were composited to create a true color image for visual interpretation. The spatial coverage of the post-Oma imagery is slightly less than the pre-Oma dataset as it

does not cover the northernmost 17 km of Fraser Island. Although post-Oma imagery for this region of Fraser Island is available, the data has not been georectified and was opted not to be used in this study. The ~195 km shoreline area analyzed in this study spans 24° 51’ 5” S to 26° 36’ 41” S.

The high spatial resolution of the PS imagery enabled the manual digitization of the HWL across the study area for both the pre- and post-cyclone image datasets (Figure 4.2). Interpretation of shoreline areas covered by clouds and shadows was avoided as they obscure the contrast difference between the dry supratidal and wet intertidal sand. Separate shoreline datasets were created for each of the shoreline compartments: Fraser Island (FI), Cooloola Sand Mass (CSM), and Sunshine Coast (SC). Multiple shoreline segments mapped within each compartment (separated by uninterpretable areas) were aggregated into a single feature for further analysis.

A LiDAR dataset was acquired from the NSW Government Department of Finance, Services, and Innovation in order to derive a Mean High Water (MHW) shoreline position. This datum-based shoreline has become the modern standard for shoreline position estimates (Ruggiero and List, 2009) and is used here to assess the accuracy of the satellite-derived HWL shoreline estimate. The LiDAR dataset covers 12 km of the Gaagal Wanggaan National Park and Carpe Diem Beach coastlines in the Macksville region of NSW. The LiDAR survey occurred between July 25-28, 2016 and a cloud-free PS image was acquired only a few days later on August 1, 2016, a short enough time interval to assume no significant geomorphic changes had occurred. An annual average MHW value of 1.421 m was described for the nearby Coffs Harbor recording station (~42 km N of

Gaagal Wanggaan) for the period 1990-2010 (MHL, 2012). A MHW shoreline was derived from the LiDAR dataset by extracting elevation values equal to 1.421±0.05 m.

The Digital Shoreline Analysis System (DSAS; Thieler et al., 2017) was used in ArcMap 10.5.1 to quantify the horizontal change in shoreline position pre- and post-Oma as well as to calculate the average horizontal offset between the HWL and MHW shoreline positions. In preparation for analysis for DSAS, the two shorelines were merged into a single feature class and an attribute table was populated following Himmelstoss (2009). A baseline used to cast alongshore measurement transects was created by buffering the post-Oma and MHW shorelines 250 m landward. Transects were then cast perpendicular to the shorelines and spaced 200 m apart along the 183 km Oma shoreline (Figure 4.3; total of 915 measurement transects) and 10 m apart along the 12 km validation shoreline (1,228 transects). The migration of the shoreline post-Oma is assessed by calculating the Net Shoreline Movement (NSM) for each of the 915 transects. A total horizontal error for the PS HWL shoreline position is reported as the mean offset from the MHW shoreline.

While a robust positional error is assessed by comparing to a datum-based MHW position and likely provides a suitable uncertainty benchmark for using PS-derived HWL shorelines, survey data were not available to assess the uncertainty of the Oma shorelines as the most recent LiDAR survey was conducted prior to the launch of the PS satellites (late 2015). As such, the uncertainty of the pre- and post-Oma shoreline positions are quantitatively assessed following the methods of Hapke et al. (2006) and Ruggiero and List (2009). Total shoreline position uncertainty accounts for errors due to: (1) georeferencing (source accuracy) (2) source Ground Sample Distance (GSD) and (3)

shoreline position uncertainty due to water level variations ("proxy-offset bias"; Ruggiero and List, 2009). The proxy-offset bias, or horizontal offset between the HWL and MHW shoreline positions, is estimated by Equation 1:

$$Bias=(X_{HWL}-X_{MHW})=\frac{([Z_T+1.1\{0.35\tan\beta^2(H_0L_0)^{1/2}+([H_0L_0(0.563\tan\beta^2+0.004)]^{1/2})/2\}]Z_{MHW})}{\tan\beta} \quad (1)$$

where Z_T is the tide level at the time of survey, $\tan\beta$ is the foreshore beach slope, H_0 is the offshore wave height, L_0 is the deep-water wave length given by linear theory as $(g/2\pi)/T^2$, where g is the acceleration of gravity and T is the wave period.

Following Ruggiero and List (2009), the long term median wave height and wavelength were used to calculate the best bias estimate. A 31 year (1979-2009) wave record from the NOAA WAVEWATCH III (WWIII) hindcast dataset was used to calculate median H_0 and T_P values (Figure 4.4). The WWIII hindcast record has been widely used due to its good agreement with *in situ* wave buoy data (Hemer, Church, and Hunter, 2007; Hughes and Heap, 2010). The 31 year record provided for this study by McSweeney and Shulmeister (2018) was selectively acquired from the 25.90° S, 153.73° E grid point due to its proximity to the coast yet still uninhibited wave passage. The elevation of Mean High Water (Z_{MHW}) was estimated to be the average of long term Mean High Water Neap and Mean High Water Spring elevations provided by the State of Queensland Department of Transport and Main Roads for tidal datum epoch 1992-2011. The tide elevation at the time of image acquisition (Z_T) was interpolated from daily low/high tide records provided by the Commonwealth of Australia Bureau of Meteorology. The closest Queensland Standard Ports to each shoreline compartment were used, which included

Waddy Point (24° 58’ S, 153° 21’ E) for FI and Noosa Head (26° 23’ S, 153° 06’ E) for CSM and SC.

Due to the unavailability of beach profile data, LiDAR data were used to calculate an average foreshore beach slope ($tan\ \beta$) for each of the three shoreline compartments. A 1 m-resolution LiDAR dataset was acquired from the State of Queensland Department of Natural Resources, Mines, and Energy (survey conducted in 2009). Three polygons defining the spatial extent of the foreshore zone at each compartment were digitized using very-high resolution (0.5 m) DigitalGlobe imagery and used to clip the DEM. The slope of each cell located within the foreshore DEM was calculated in ArcGIS Pro as shown for a stretch of SC in Figure 4.5. The mean foreshore slope values for FI, CSM, and SC were used to calculate the proxy-offset bias for each shoreline compartment.

The total estimated shoreline position uncertainty (E_{sp}) for the FI, CSM, and SC shoreline compartments was estimated following the method of Hapke et al. (2006) and Cenci et al., (2013). The total error is estimated by taking the square root of the sum of the squares of georeferencing error (E_g), source pixel error (E_{GSD}), and the proxy-offset bias (E_p) as shown by Equation 2:

$$E_{sp} = \sqrt{E_g^2 + E_{GSD}^2 + E_p^2} \qquad (2)$$

Per Hapke et al. (2006), the georeferencing error (E_g) is the maximum RMS error for the data source, which is defined as 10 m for PS imagery (Planet, 2017). The source pixel error is equal to the GSD of orthorectified PS imagery (3 m) and is included as features smaller than the GSD cannot be resolved (Cenci et al., 2013). Only transects with NSM values greater than the $\pm Ep$ of their associated compartment were considered valid

and used to describe Oma-induced shoreline change. The greater of the two *Ep* values for the pre- and post-Oma images at each compartment was used as the uncertainty threshold.

Wave monitoring data were acquired in order to understand the interaction between the Oma-enhanced wave climate and the observed shoreline change. The Mooloolaba Waverider buoy is located offshore of Coolum Beach at the southern extent of SC (26° 33.960’ S, 153° 10.870’ E; Figure 4.1) in 32 m water depth and is jointly operated by the State of Queensland Department of Environment and the Department of Transport and Main Roads. The buoy acquires a suite of wave climate parameters such as significant wave height, maximum wave height, wave period, wave direction, and sea surface temperature at a 30 minute interval. A record spanning January 1, 2019 through February 28, 2019 was acquired to characterize the Tropical Cyclone Oma wave climate.

4.3 Results

The absolute positional uncertainty of a PS-derived shoreline was assessed by comparing to a contemporaneous MHW shoreline derived from a 1 m LiDAR dataset (Figure 4.6). The horizontal offset between the HWL and MHW shorelines along the 12 km study area ranged from 0.01 to 22.06 m with an average offset of 9.02 m. The MHW shoreline position was almost ubiquitously landward of the HWL shoreline as only 36 of the 1,227 (3%) measurement transects recorded a negative NSM value.

Storm events in southeast Australia are typically defined as waves exceeding 3 m significant wave height (Harley et al., 2010). This threshold is only achieved during Tropical Cyclone Oma and more specifically, from February 21, 21:30 to February 25, 0:00 AEST (Figure 4.7). The mean H_s during Oma (3.14 m) was more than double the two

month mean H_s leading up to the storm event (1.54 m) with a maximum H_s of 4.21 m recorded on February 22 at 13:30. The average peak wave direction (D_p) during the approximately 3 day storm event was 101.1°, a substantial 11.4° increase over the two month mean (89.7°). The peak wave direction ranged over 50° as a sharp anti-clockwise rotation in wave direction occurred between 63° and 119° (Figure 4.7).

The southeast Queensland coast analyzed in this study is divided into three separate compartments on the basis of political boundaries (i.e. Fraser Island) and broad geomorphic characteristics, i.e. the high dune bluffs backing the CSM shoreline versus the predominantly built-up area adjacent to the SC shoreline. A description of the total shoreline uncertainty (E_{sp}) and the geomorphic and metocean characteristics used for each of these compartments is provided in Table 4.1. The total mapped shoreline length for the pre-Oma shoreline across the entire study area is 183.2 km and 181.5 km for the post, where the remaining 12 to 14 km of the study area were uninterpretable due to the presence of clouds and cloud shadows masking the HWL boundary. Net shoreline movement was calculated every 200 m alongshore with negative values representing erosion and vice versa for accretion in Figures 4.8 through 4.10. Any NSM values that are within the ranges of uncertainty (E_{sp}) were omitted from shoreline change analysis.

Net shoreline movement derived from pre- and post-storm PS imagery shows that the FI shoreline both prograded and eroded during Tropical Cyclone Oma (Figure 4.8). Areas of significant erosion are clustered in the northern and southern extents of FI. Approximately 53% of the SE-NW trending Orchid Beach shoreline (16.7 km) located at the northernmost extent of the FI study area eroded with an average landward movement of

17.4 m and NSM values ranging from -11.99 to -33.4 m. A 12 km, SE-NW trending stretch at the southern end of Seventy-Five Mile Beach shows significant erosion with an average NSM of -19.8 m ranging between -14.25 and -31.66 m. Areas of progradation are clustered throughout much of the SW-NE trending 75 Mile Beach and at the Great Sandy Strait inlet that separates FI from CSM. The northernmost 9 km of 75 Mile Beach prograded an average of 22.1 m within a range of 15.1 to 34.9 m. A 5 km stretch in the north-central region of 75 Mile Beach prograded an average of 19.6 m within a range of 14.2 to 29.0 m. A 9 km stretch in the central region of the same beach showed an average progradation of 17.6 m ranging between 14.4 to 22.9 m. The largest amount of accretion occurred near the Great Sandy Strait inlet where a 3 km stretch of the shoreline prograded an average of 22.4 m within a range of 14.7 to 28.6 m. Within this same section, a narrow, 400 m band of erosion amounting to 22.7 m was observed.

Net shoreline movement statistics show that the CSM mostly prograded in response to Tropical Cyclone Oma (Figure 4.9). A 1.6 km, SE-NW trending stretch at the northernmost extent of the CSM near the inlet experienced the most extreme shoreline change as it predominantly prograded an average of 42.9 m (with a maximum of 70.2 m) with a narrow band of erosion amounting to -21.7 m. Further south, a 500 m stretch located near the Double Island headland shadow zone prograded 19.7 m. The widest area of progradation occurred along the northern end of SW-NE trending Noosa North Shore where a 5 km stretch prograded an average of 21.7 m within a range of 16.0 to 29.7 m. The southernmost 1 km of CSM, bounded by the Noosa River to the south, prograded an average of 19.9 m within a range of 15.0 to 32.8 m. The significantly higher shoreline

position uncertainty for SC (±23.28 m) led to most of the NSM values not being used for shoreline change analysis. Although, discrete locations of erosion are observed throughout the region and most (>90%) of the uncertain NSM data points indicate erosion (Figure 4.10). An NSM value of -41.1 m was calculated at the beach fronting the town of Coolum and is aligned with a tidal creek. To the north, two transects with NSM values of -24.6 and -24.5 m indicate significant erosion of the beach bordering the town of Sunshine Beach. Finally, the NW facing beach at Noosa Spit, which marks the northern terminus of SC, experienced significant erosion with NSM amounting to -29.0 m.

4.4 Discussion

The 3 m imagery provided by the PS constellation proved to be an effective source for mapping the HWL, the most commonly used shoreline indicator in change studies. The color contrast between the dry supratidal and wet intertidal sediment was easily observable in true color composites, which enabled a reliable manual digitization of the shoreline indicator across a large study area for multiple dates. This represents a significant improvement on previous shoreline change studies that utilized lower spatial resolution satellite imagery such as Landsat (30 m) and Sentinel-2 (10 m). Where these image products are too coarse to visualize the HWL, spectral water indices such as NDWI and MNDWI are used to define and track the movement of the shoreline boundary. This mapping technique was found to be significantly influenced by tide height at the time of satellite flyover (Kelly et al., 2019) where interpretation of imagery collected at low tide would show apparent shoreline progradation (and vice versa at high tide). The ability to define the HWL in PS imagery removes much of the uncertainty associated with the

horizontal movement of the shoreline due to tidal variability, which is typically encountered when using spectral water indices to extract a shoreline boundary.

The response of the three shoreline compartments to the storm wave climate show some similarities, primarily based on the relationship between the orientations of the shorelines and their observed response. The northern ends of the extensive SW-NE oriented coasts of FI and CSM show significant progradation, where they are both bound by rocky headlands to the north. Concurrently, the southern end of the same coast on FI that is oriented SE-NW shows similar amplitude erosion. There is a possibility that the southern end of CSM also eroded in a similar manner to FI, although the amount of shoreline erosion detected (-12.0 m) is just below the level of local E_{sp} uncertainty (±13.86 m) but is beyond the bounds of MHW offset error (±9 m). In between the southern erosional and northern progradational hot spots, both the FI and CSM shorelines show stable to progradational change in response to Oma. The second, more northern shoreline compartment on FI (Orchid Beach) shows nearly ubiquitous erosion, with the largest retreat amounting to -33.6 m. The orientation of this section is similar to that of the southern erosional area on FI (SE-NW). While most of the NSM values on SC were omitted due to a much higher uncertainty threshold, areas of significant erosion were detected and the general trend of the alongshore NSM is erosional. SC does not show the shared southern-erosion northern-accretion pattern as FI and CSM, which could be due to its more N-S orientation and exposure to wave incidence.

The rapid and significant anti-clockwise rotation in peak wave direction from 63° (incident from the NE) to 119° (incident from the SE) could potentially describe the spatial

relationship in erosional and progradational patterns observed in the study area. Previous studies have attempted to describe the geomorphic response of shorelines to changes in El Niño-Southern Oscillation (ENSO) influenced wave climates (Ranasinghe et al., 2004; Short, Trembanis, and Turner, 2000). Ranasinghe et al. (2004) show that La Niña phases are associated with a predominantly northeasterly wave direction, which leads to the erosion at the northern end and accretion at the southern end of embayed shorelines in New South Wales (anti-clockwise rotation). The opposite is held true during El Niño phases when a more southeasterly wave climate leads to accretion in the northern end of the same shoreline areas (clockwise rotation).

The same shoreline rotation response likely occurred here, except at the time scale of days rather than years due to the amplified erosive wave power. As the incident wave direction rotated to the SE, the direction of longshore transport switched from a predominantly southerly direction to the north. The southern ends of FI and likely CSM eroded and the material was transported north along the coast where it was ultimately deposited due to blocking from the Double Island and Waddy Point rocky headlands, leading to significant shoreline progradation. Although spatial coverage of the PS imagery did not allow for analysis of the northern end of Fraser, material eroded from Orchid Beach is likely transported to the northern end of the island and transported over the shelf edge due to uninhibited littoral drift (Boyd et al., 2008). The significant progradation observed on the downdrift sides at the inlets of the Great Sandy Strait and Noosa River are likely related to tidal dynamics. This could potentially be due to storm surge-induced ebb-channel switching that ultimately released sediment within a few kilometers downdrift of

the Great Sandy Strait inlet, as has been observed at other inlets during hurricane conditions (Morton et al., 1995). Significant erosion of the ebb tidal delta is also likely to occur during storms, mobilizing sediment that is transported and deposited downdrift (Miner et al., 2009; Morton et al., 1995). The inflection point of the shoreline area influenced by tidal dynamics on FI is likely within the 3 km section located 7 to 10 km alongshore just prior to the erosive section. The predominantly erosive response of SC could be due to its steeper beach slope that could have reduced wave dissipation in the nearshore zone leading to enhanced wave energy at the shoreline (Vousdoukas et al., 2009). Due to this process, offshore transport of beach sediment along SC would cause a reduction in beach slope and significant landward migration of wave runup and the HWL.

In addition to seaward migration of the HWL, geomorphic indicators of shoreline erosion were visually observed in the PS imagery throughout the study area (Figure 4.11). A 2 km long sand spit was present along the southern extent of Orchid Beach on the northern half of FI. Much of the pre-Oma sand spit was subaerial based on similar spectral characteristics with the mainland attached beach. A narrow lagoon (50 m at its widest) separated the sand spit from the mainland and a 15 m wide inlet breached the spit and connected the lagoon to the Coral Sea. The post-Oma image shows significant infilling of the lagoon, with the remnants taking on the form of “cat’s eye” ponds. The once subaerial sand spit appears to have been completely submerged during Oma based on the distinctly darker color of the sediment (Figure 4.11a). Just downdrift from the spit, significant sediment migration over partially vegetated foredune ridges and lagoons is visible in the imagery (Figure 4.11b). Approximately 2 km of Orchid Beach fronting the identically

named seaside resort town experienced significant sand encroachment with an observed maximum migration distance of 61 m. Additionally, significant sediment migration into the Stumers Creek tidal inlet on SC is visible in the post-Oma imagery and is spatially coincident with southernmost erosive NSM transect (-41.1 m; Figure 4.11c). In the pre-Oma image, recent channel outflow onto the beach is apparent based on the appearance of darker, wet sediment spanning the width of the beach and into the channel. In the post-Oma image, there is no longer evidence of active outflow as the backshore now consists of dry, supratidal sediment that has migrated ~30 m into the Stumers Creek inlet.

The acquisition of global, high resolution imagery at a daily repeat interval has been and will continue to be shown to be paramount in modern and future global change studies. The daily acquisition of PS imagery has already been shown to optimize the timing of harvesting events (Houborg and McCabe, 2018), enhance volcano monitoring (Barnie et al., 2018), and aid in global disaster response efforts (Zajic et al., 2018). This work shows for the first time that PlanetScope's daily repeat interval allowed for a near-immediate mapping of the shoreline in the aftermath of a significant storm event. This enabled a detailed description of storm-induced shoreline change and identification of areas that experienced enhanced erosion/progradation, which is of great interest to local decision makers for shoreline management strategies. The method used here represents a notable improvement in rapidly assessing shoreline changes in the aftermath of a storm event. Previous techniques for describing shoreline change in a rapid response manner are limited due to logistical difficulties (expedited mobilization and access to field site) as well as cost (aerial imagery acquisition). Using satellite imagery for rapid assessment was also

previously difficult due to low repeat intervals (5 days for Sentinel-2 and 16 for Landsat) that would likely be exacerbated if the area of interest was cloud covered during the initial post-storm satellite flyover. Classifying geomorphic changes observed during the subsequent flyover up to 4 weeks after the event ended would likely be imprudent. While other commercial satellites that acquire near-daily, very-high resolution imagery such as DigitalGlobe's WorldView constellation have been used to describe shoreline change (Maglione, Parente, and Vallario, 2014; Sekovski et al., 2014), the acquisition cost can be prohibitively expensive.

While the PS imagery can be used for mapping the HWL on a near daily basis, it is not without its own drawbacks. The PS-derived HWL shoreline shows an average horizontal offset of 9 m from the optimal MHW shoreline position at the validation study site. This could potentially be due to drying of the intertidal sediment, which would cause an apparent shoreline progradation of the mapped HWL. This is likely the cause of the error determined here as 97% of the HWL shoreline was positioned seaward of the MHW shoreline. Regardless, this positional error analysis based on in situ, temporally coincident survey data provides a benchmark for future studies that use PS imagery to map and describe shoreline changes over time. It's likely that this uncertainty value will decrease in beach environments with steeper foreshore slopes as the excursion zone is narrowed.

The total shoreline position uncertainty (E_{sp}) of the three Oma study areas omitted 88.3% of the total NSM values as they were within the error of the mapping technique, which ranged between ±13.86 (CSM) and ±23.28 m (SC). This translates to 21.4 km of the 181.5 km long study area ultimately being retained and used to assess geomorphic changes

to the shoreline. A potential source of error in estimating E_{sp} here is the measurements of $tan\beta$ at each shoreline segment, which was derived from a LiDAR dataset collected in 2009. The E_{sp} of SC was calculated for variable $tan\beta$ values in an effort to assess its potential variability based on fluctuating foreshore slopes. Stockdon et al. (2006) describe oceanographic and geomorphic characteristics of a wide range of natural beaches. They noted that gently sloping (dissipative) beaches that have a mean slope of 0.06 can vary by up to ±0.002. Using these upper and lower slope limits, the E_{sp} at SC (20.65 m when $tan\beta$ = 0.049) is 0.32 m greater when $tan\beta$ = 0.047 (1.3% difference) and 0.57 m less when $tan\beta$ = 0.051 (2.4%). As such, variability of $tan\beta$ should not be considered a significant source of error for calculating E_{sp}, although this may not hold true at steeper, more reflective beaches where significant lowering can occur.

The greatest source of error in the E_{sp} calculations for all but one of the image datasets was the georeferencing error (geometric accuracy) of the PS data product (10 m). Only the pre-Oma dataset for SC had a larger source of error, which was its proxy-offset bias (E_p; 20.65 m). The pre-Oma SC E_p value of 20.65 was due to the abnormally high tide during the survey on February 19 (Z_T; 1.79 m), which was 0.17 m higher than the Z_{MHW}. Given that the proxy-offset bias is primarily due to wave driven water level variations (setup and swash) driving the horizontal displacement between the HWL and MHW (Ruggiero and List, 2009), E_p is expected to be anomalously large if $Z_T > Z_{MHW}$ and wave runup is amplified. The lowest E_p values were achieved when $Z_T < Z_{MHW}$ (i.e. E_p = 3.30 and 3.21 m when Z_T = 0.99 and 1.03 m for the post-Oma FI and CSM datasets) as wave runup during low-to-mid tide positions the HWL close to MHW. Future studies using PS to map

shorelines using this technique should consider the tide height during the time of satellite flyover to minimize the position error due to the proxy-offset bias. Future improvements on the orthorectification of the PS data products will also significantly improve the shoreline position uncertainty, although its 10 m RMS geometric accuracy is already an improvement on Landsat 8 (12 m RMS; Roy et al., 2014) and Sentinel-2 (11 m RMS; ESA, 2019).

4.5 Conclusions

Tropical Cyclone Oma was a powerful, Category 2 storm that moved towards the southeast Queensland coast over the course of 9 days. Although the storm never made landfall in Australia, it reached within 450 km of Fraser Island during which time it had weakened to a Category 1 cyclone. The close proximity of the massive storm to the Sand Island coast produced remarkably high surf conditions, as observed by wave monitoring buoys that recorded significant wave heights up to 10 m. These storm surge conditions were amplified by a king tide that resulted in flooding along the Brisbane River. The impacts of these extremely energetic oceanographic conditions on the sandy, open coast shorelines of southeast Queensland were assessed using newly available, high temporal and spatial resolution satellite imagery.

The HWL was mapped on the 3 m resolution, multispectral PlanetScope imagery by manually defining the boundary between wet intertidal and dry supratidal sediment. Pre-storm shoreline positions were mapped across the study area using imagery collected 3 and 6 days prior to the arrival of Oma and post-storm positions were defined a mere 3 days after the storm wave conditions returned to normal. For the first time, the total shoreline

position uncertainty associated with using PS imagery to map the HWL was assessed by comparison to a temporally coincident MHW shoreline at a distant validation site and by calculating the proxy-offset bias at the Oma-impacted study area. The average horizontal offset between the MHW and HWL shorelines across the 12 km validation site was 9.02 m with the HWL shoreline nearly entirely seaward of the MHW. The local E_{sp} across the three shoreline compartments ranged from ±13.86 to 23.28 m. Uncertainty of the PS-derived shorelines was primarily due to the geometric accuracy of the Level 3B PS imagery (10 m RMSE), in addition to its pixel size (3 m) and site-specific proxy-offset bias.

Net Shoreline Movement statistics calculated by the Digital Shoreline Analysis System show that the FI and CSM both prograded and eroded and SC eroded during Tropical Cyclone Oma. The FI and CSM shorelines display similar spatial patterns in the locations of erosion and accretion. The northern ends of their extensive SW-NE oriented shorelines experienced significant progradation that was contemporaneous with shoreline erosion at their southern ends with stable to uncertain progradation occurring in between. The wave climate during the three day storm period (when Hs > 3 m) experienced a rapid and significant 56° anti-clockwise rotation (from 63° to 119°). This likely shifted the mean direction of longshore transport to the north and resulted in clockwise beach rotation, a geomorphic process observed at quasi-biennial time scales due to ENSO phase variability. Although the higher E_{sp} of the SC shoreline omitted most of the NSM values, regions of exceptional shoreline erosion were identified and are theorized to have been due to its steeper beach slopes that lowered due to enhanced wave energy.

This study demonstrates for the first time the capability of using PS imagery to map shoreline positions and detect their horizontal change occurring at a weekly time interval in response to episodic events. The daily repeat interval of the PS satellites allowed for acquisition of mostly cloud-free, georectified imagery one week prior to and after Oma's arrival. This ensured that the significant shoreline changes described by both the migration of the HWL and through direct observation of geomorphic processes were entirely due to Oma. This study also shows that using PS imagery significantly improves rapid detection and assessment of shoreline changes in the immediate aftermath of a storm or other powerful event. Previous techniques were limited due to prohibitively expensive costs (airborne surveys), logistical difficulties (access to damaged field site), and inadequate temporal coverage (Landsat repeat interval of 16 days). Future improvements in the accuracy of PS-derived shoreline positions can be achieved through enhancement of the geometric accuracy of the PS data products and selective use of images that were acquired at mid-to-low tide. Automated mapping of the HWL using PS imagery across regional-to-continental scale study areas could be possible using Support Vector Machine and other machine learning classification techniques and is the subject of future work.

4.6 Acknowledgements

We would like to thank Planet Labs, Inc. for providing their PlanetScope imagery through their Education and Research Program, The State of Queensland for supplying tide and wave data, and the NSW Government for providing the LiDAR dataset. This work was carried out within the Joint Doctoral Program in Earthquake Science and Applied Geophysics at the University of California San Diego and San Diego State University. The

paper was significantly improved by the comments of the two anonymous reviewers. Chapter 4, in full, is a reformatted version of the material as it currently appears ahead of press in the *Journal of Coastal Research*: Kelly, Joshua T. and Gontz, Allen. 2019. Rapid assessment of shoreline changes induced by Tropical Cyclone Oma using CubeSat imagery in southeast Queensland, Australia. Journal of Coastal Research. Joshua Terence Kelly was the primary investigator and author of this paper.

Table 4.1: Geomorphic and metocean characteristics used to calculate the proxy-offset bias (E_p) and total shoreline position uncertainty (E_{sp}) of the three shoreline compartments.

Shoreline Compartment	**Mean *tan β***	**Z_T (pre/post, in m)**	**Z_{MHW} (m)**	**Median H_0 (m)**	**Median T_p (s)**	**Median L_0 (m)**	**E_p (pre/post, in m)**	**E_{sp} (m)**
FI	0.029	1.18/0.987	1.62	1.76	8.60	115.35	8.82/3.30	±13.92
CSM	0.035	1.19/1.03	1.62	1.76	8.60	115.35	8.73/3.21	±13.86
SC	0.049	1.79/1.03	1.62	1.76	8.60	115.35	20.65/5.14	±23.28

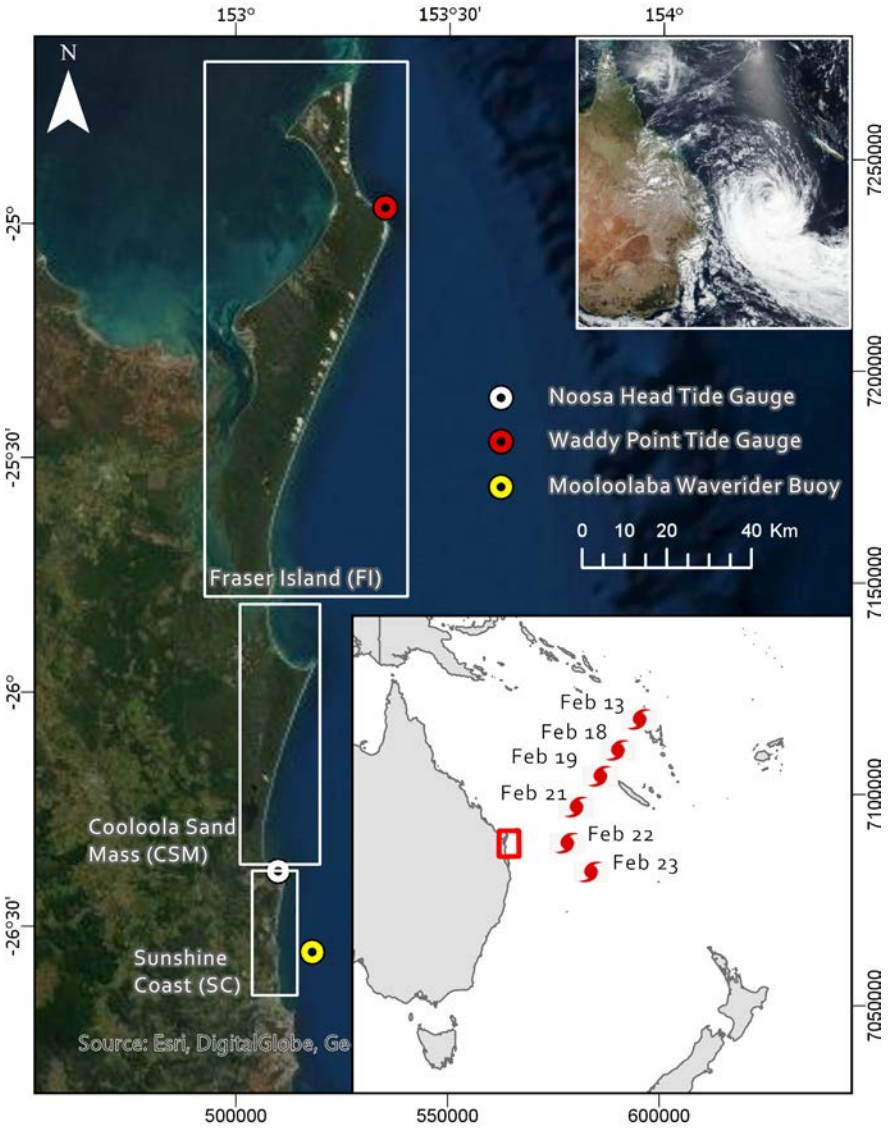

Figure 4.1: Locations of wave and tide monitoring buoys and the three shoreline study areas: Fraser Island (FI), Cooloola Sand Mass (CSM), and the Sunshine Coast (SC), Queensland, Australia. Inset maps show the geographical context of the study area, the track of Tropical Cyclone Oma, and an image of the storm on February 22, 2019 (courtesy of NASA MODIS). DigitalGlobe WorldView imagery used as basemap.

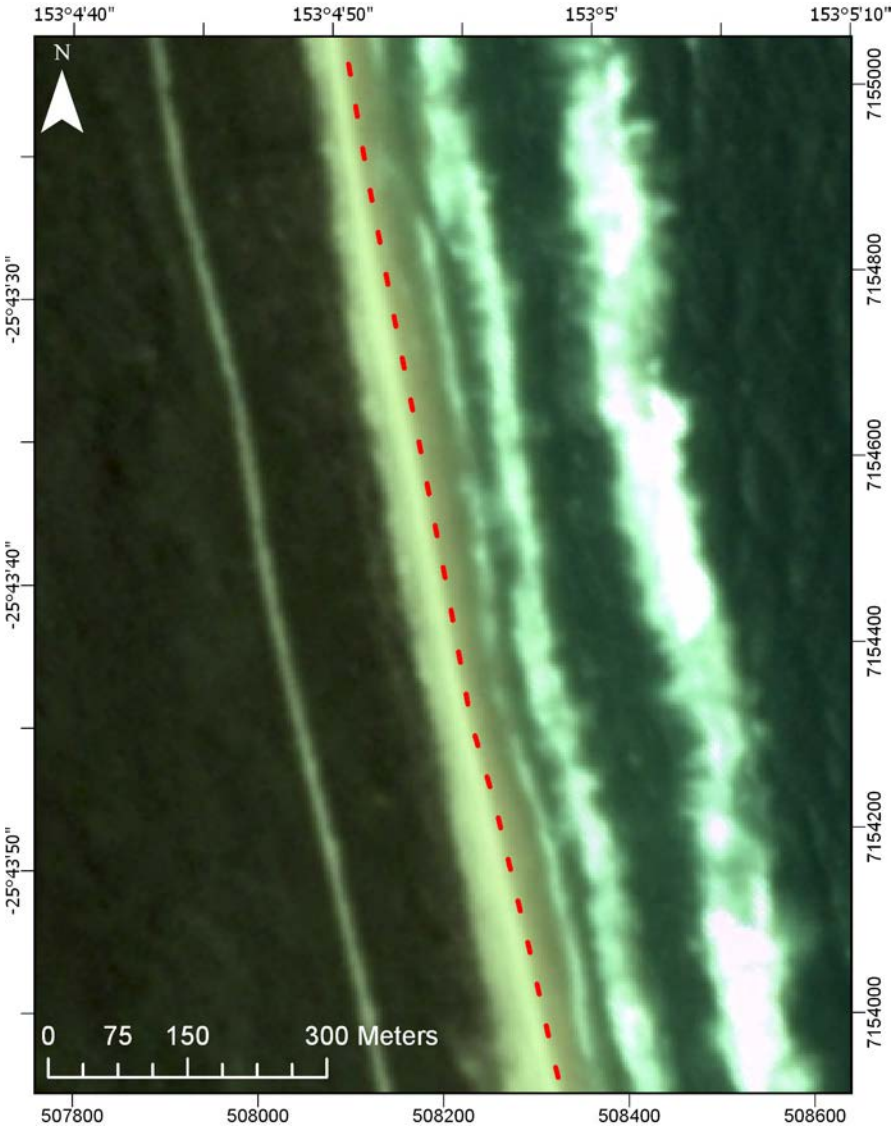

Figure 4.2: Delineation of the High Water Line boundary on a PlanetScope RGB composite image.

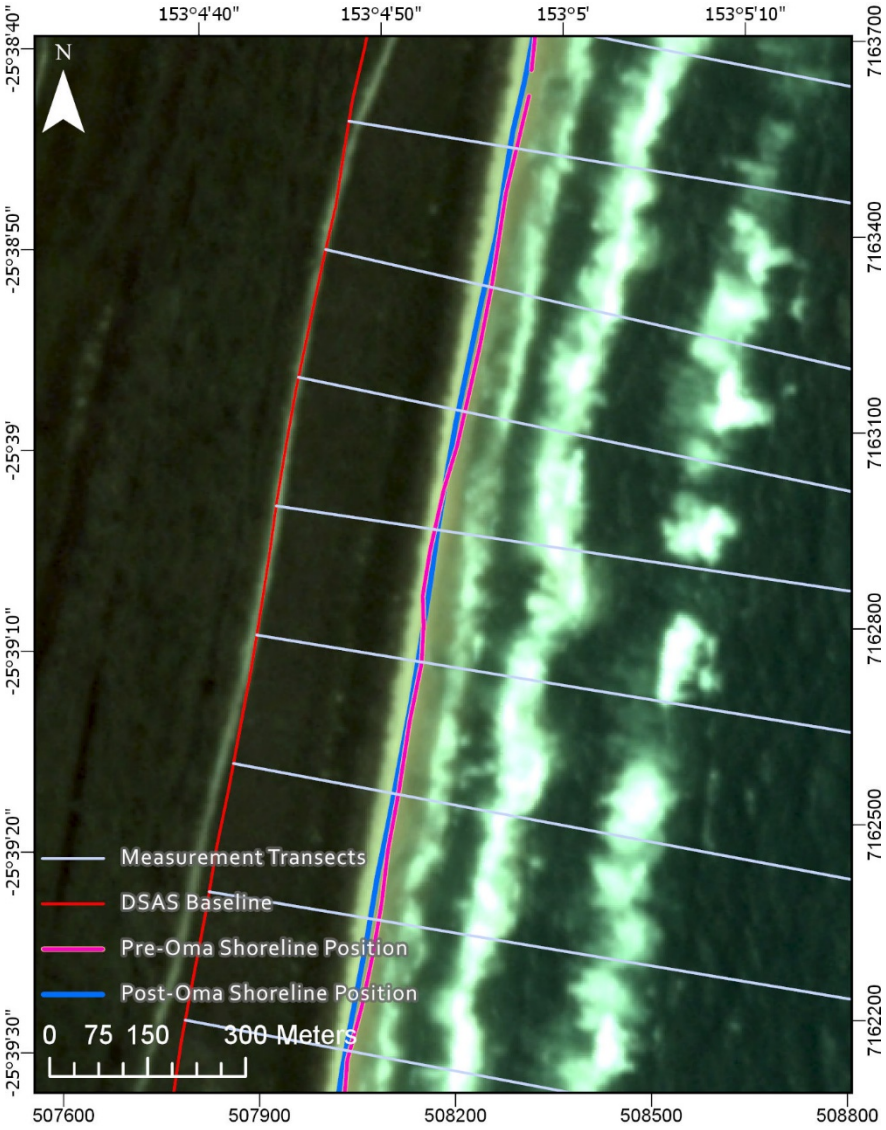

Figure 4.3: Components of the Digital Shoreline Analysis System: pre- and post-storm shoreline positions, baseline constructed landward of the shoreline dataset, and measurement transects cast every 200 m alongshore from the baseline.

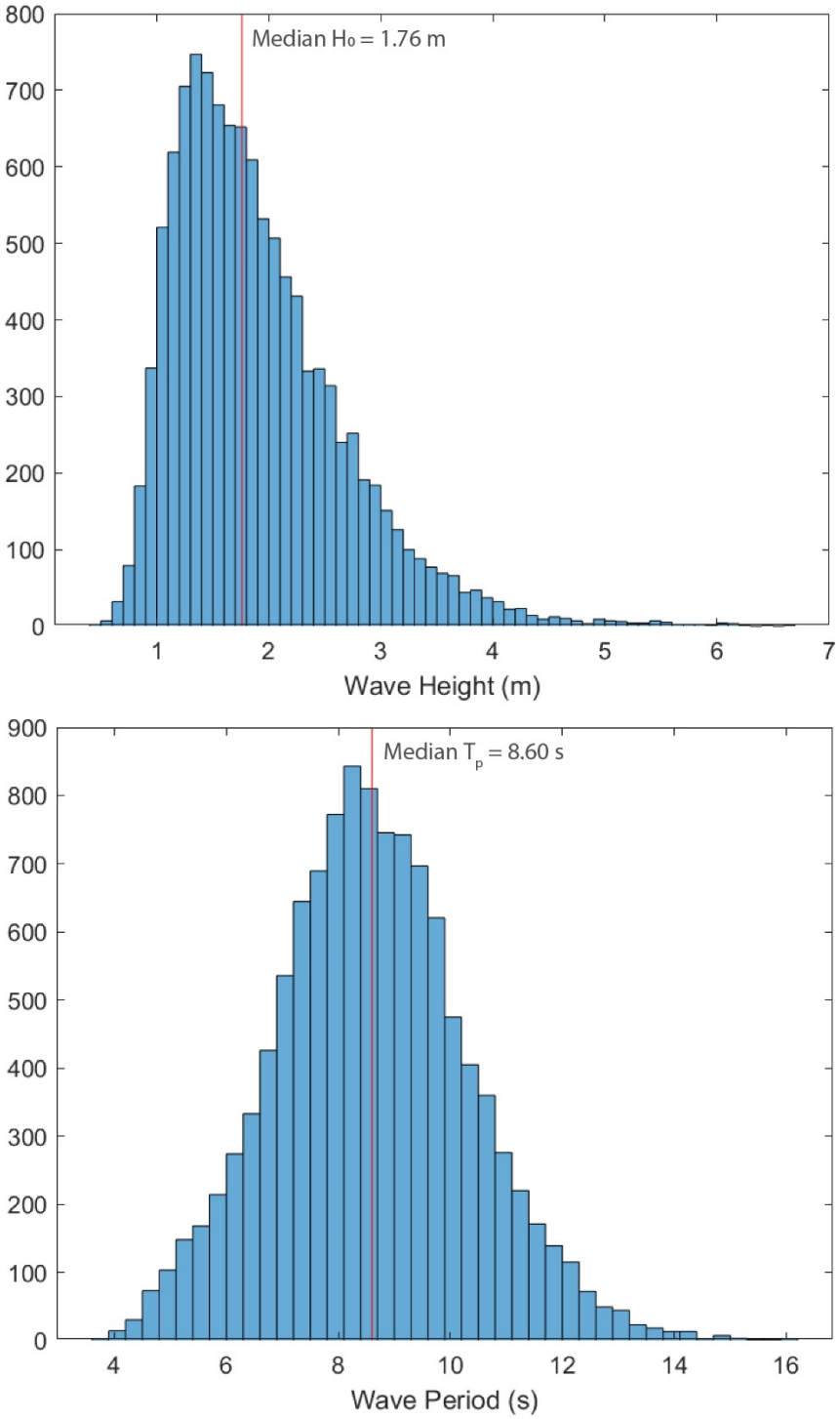

Figure 4.4: 31 year (1979-2009) wave height (m) and period (s) record from the NOAA WAVEWATCH III (WWIII) hindcast dataset used to calculate median H0 (1.76 m) and Tp (8.60 s) values.

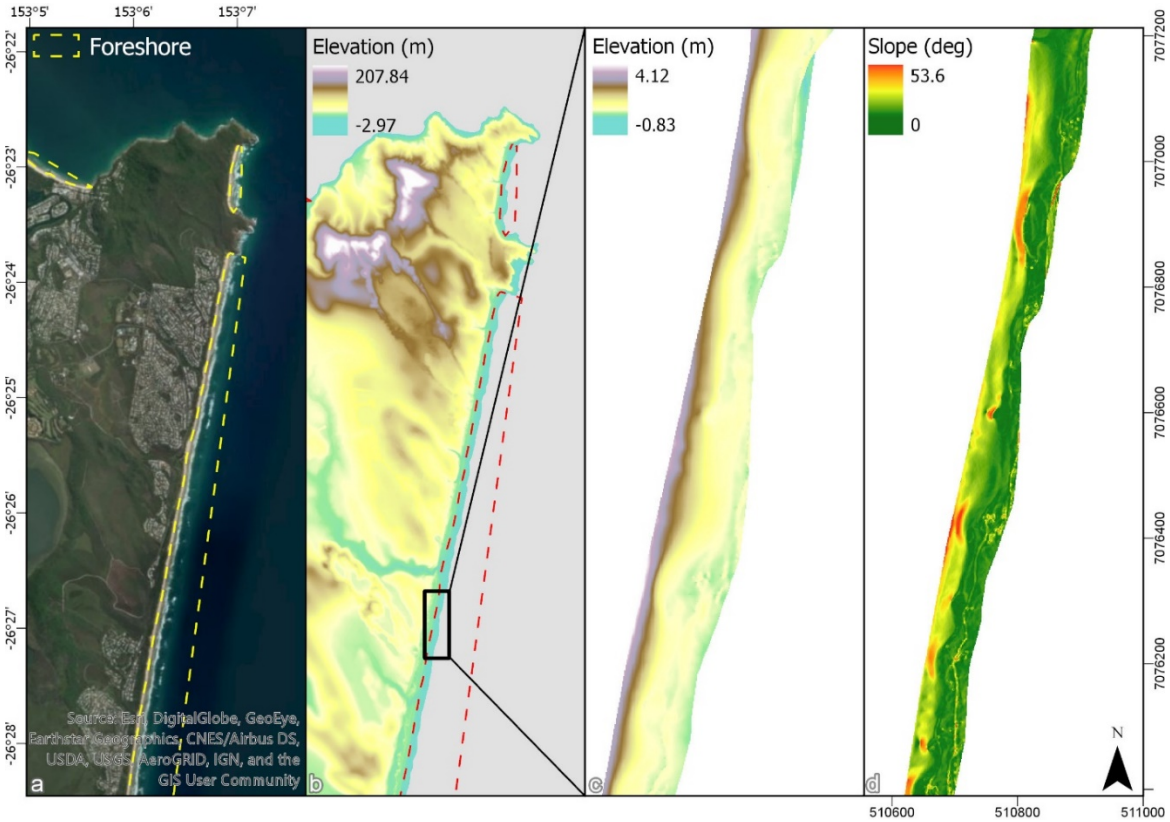

Figure 4.5: Process of deriving average foreshore slope values from 1 m LiDAR data a. Manual delineation of the foreshore area in very high resolution WorldView imagery b. Digital Elevation Model (DEM) derived from the LiDAR point cloud data c. Extraction of the DEM for the mapped foreshore area d. Slope calculation for every cell located in foreshore.

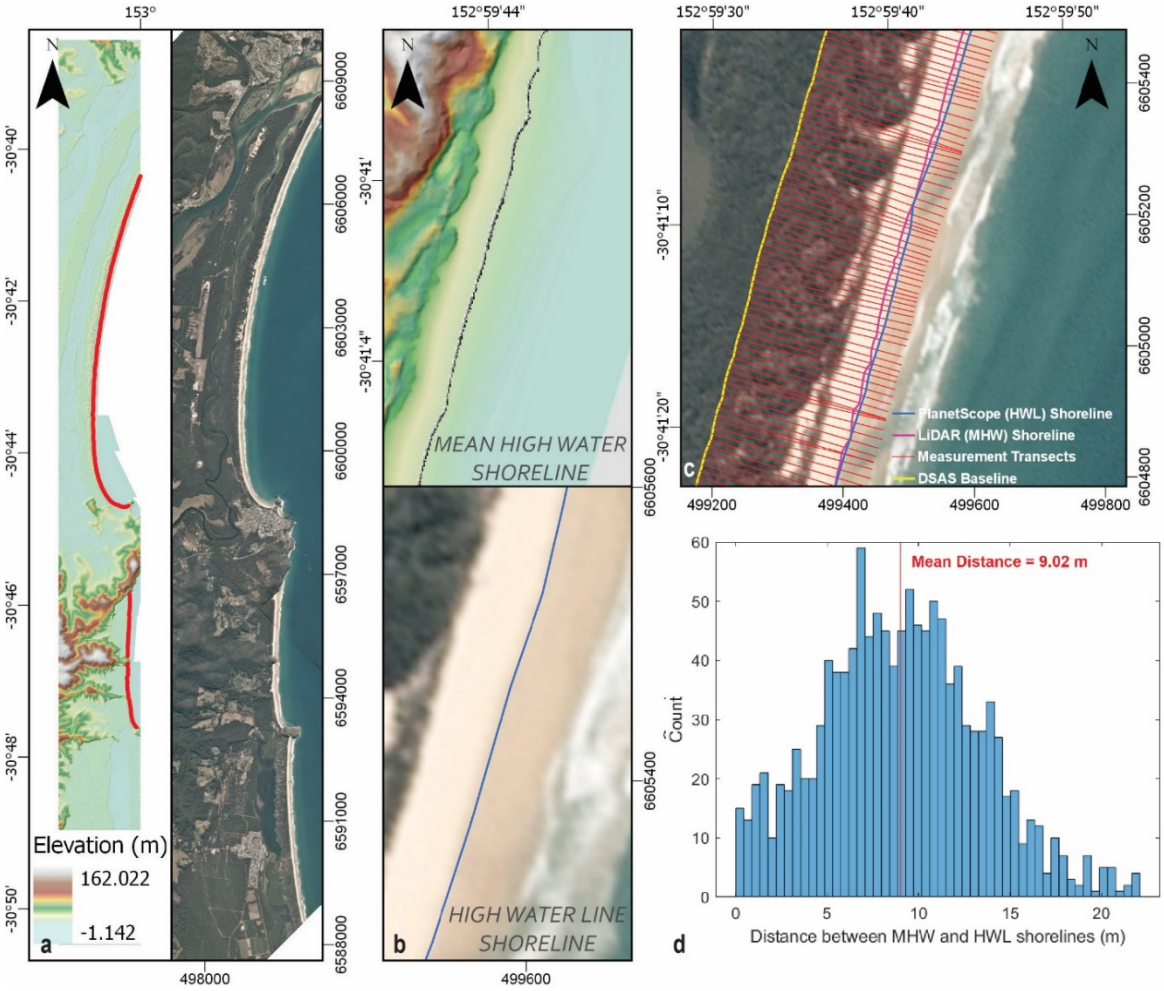

Figure 4.6: a. LiDAR and PlanetScope imagery used to extract MHW and HWL shoreline positions at the validation site (indicated by red line) b. Extraction of MHW and HWL shorelines c. DSAS components showing HWL and MHW shorelines with 10 m-spaced measurement transects d. Histogram count of 1,227 NSM calculations indicating an average horizontal offset of 9.02 m.

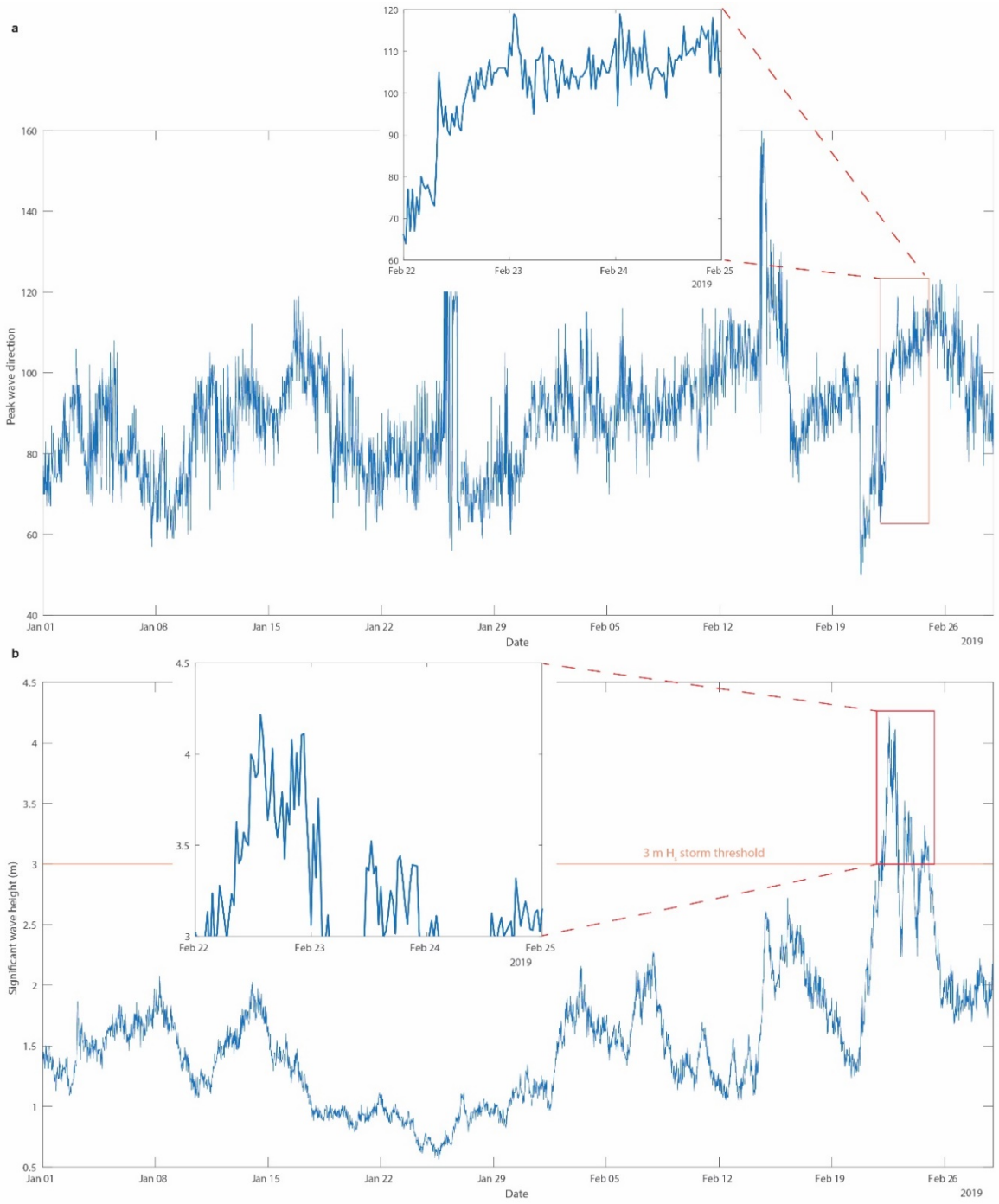

Figure 4.7: a. Normal and storm wave directions (° from north) measured from the Mooloolaba Waverider buoy from January 1 to February 28, 2019. Inset plot highlights Oma storm wave directions b. Normal and storm significant wave heights (m) as defined by the 3 m Hs threshold.

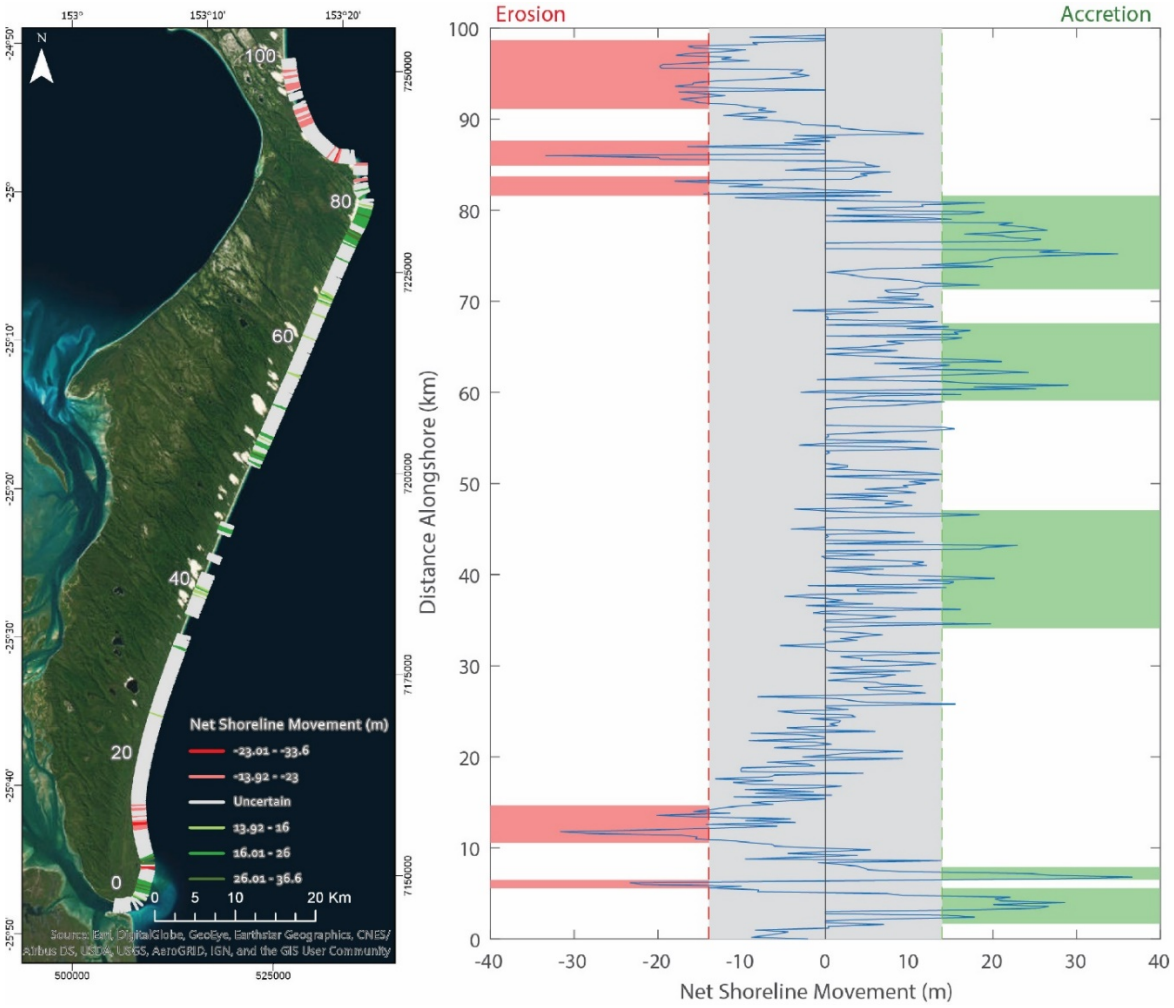

Figure 4.8: Net Shoreline Movement across the Fraser Island (FI) study area. Positive NSM values (green) indicate areas of certain progradation and negative NSM values (red) highlight erosion. The grey region in the plot indicates NSM values within the range of uncertainty (±13.92 m). Numeric values on the map show distance alongshore for correlation to the plot.

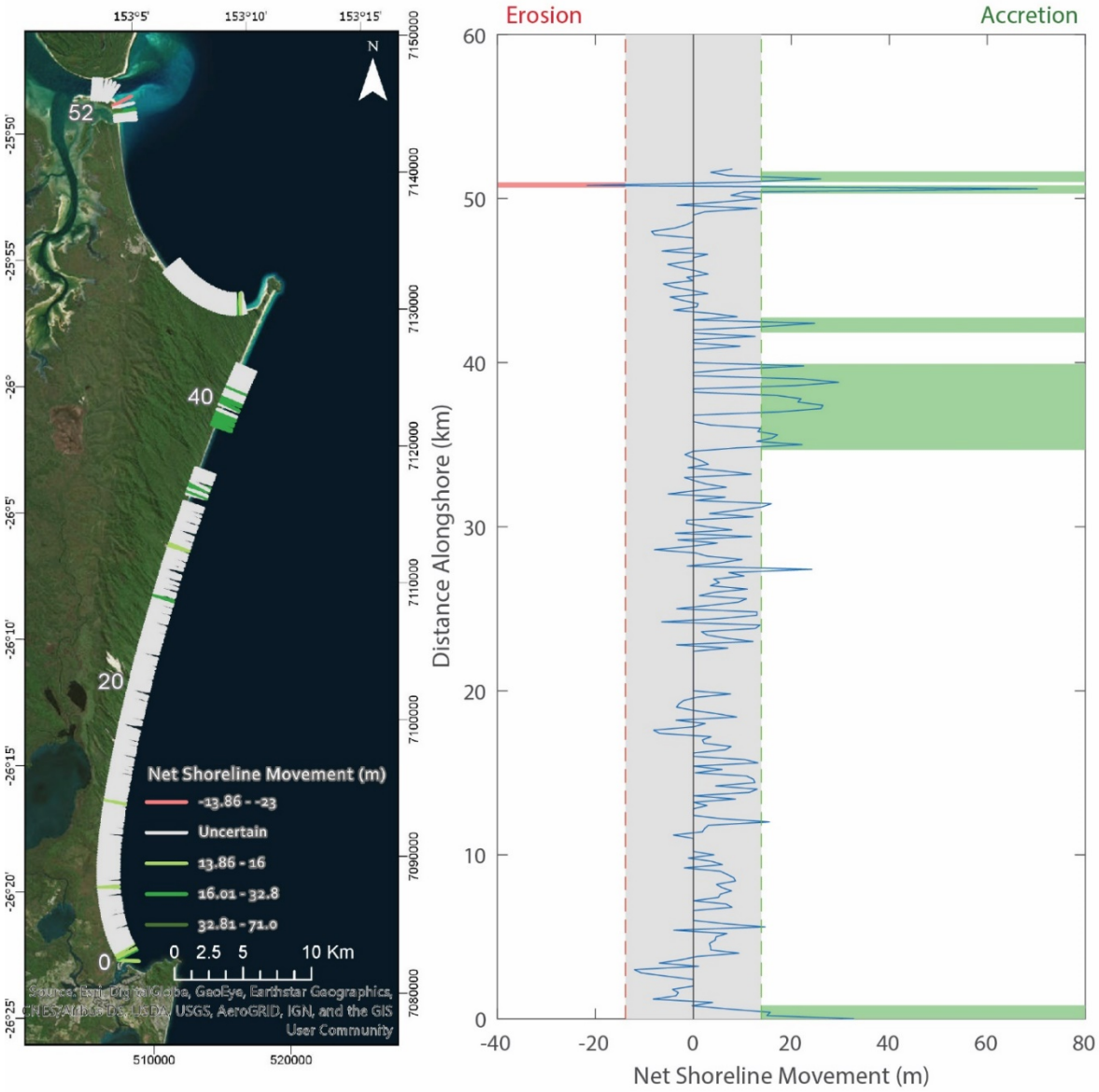

Figure 4.9: Net Shoreline Movement across the Cooloola Sand Mass (CSM) study area (uncertainty = ±13.86 m).

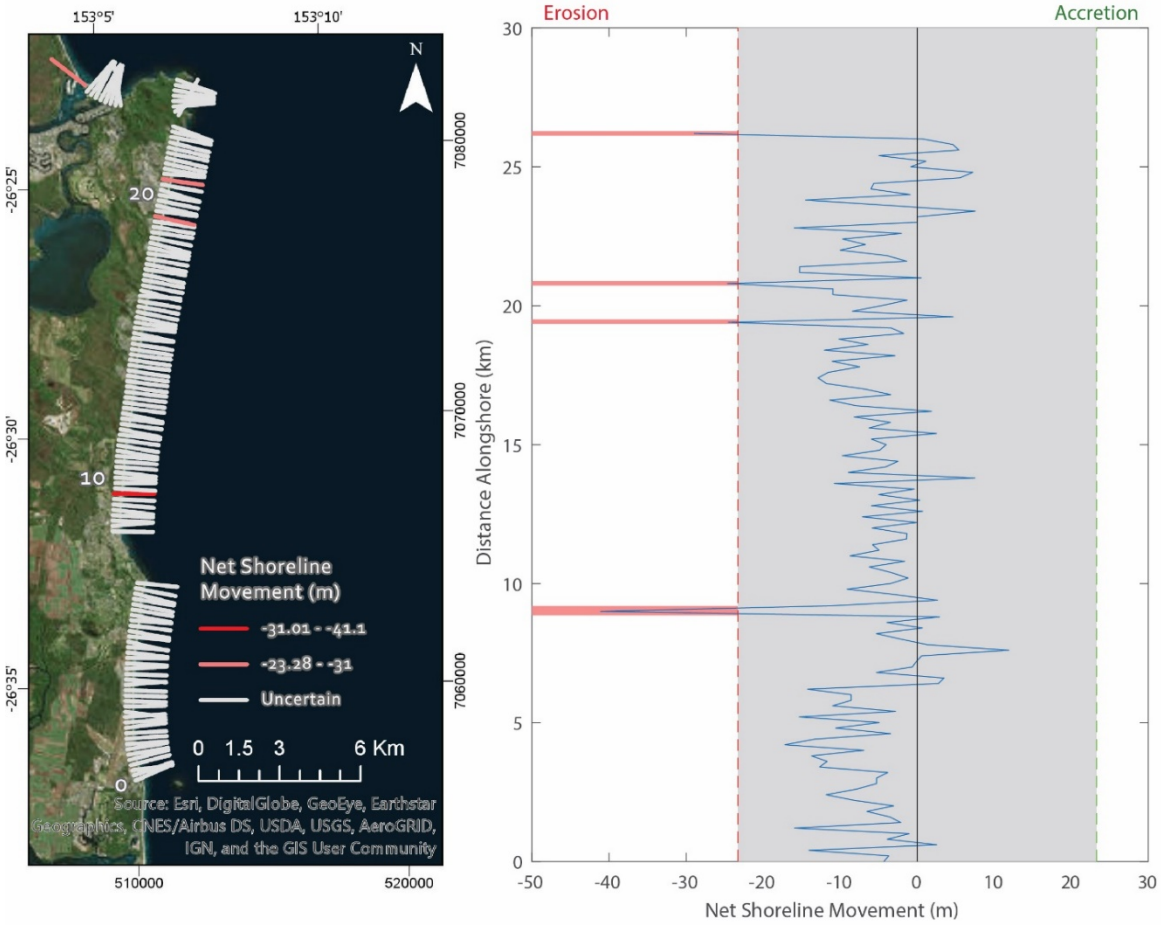

Figure **4.10**: Net Shoreline Movement across the Sunshine Coast (SC) study area (uncertainty = ±23.28 m).

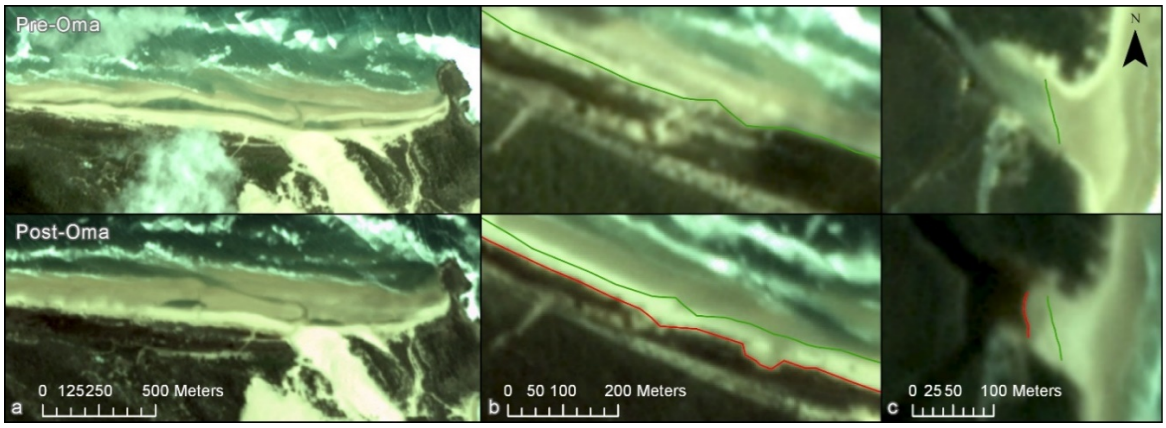

Figure **4.11**: Geomorphic indicators of shoreline erosion in pre- (2/15 and 2/19) and post-storm (2/27) PlanetScope imagery a. Submergence of a 2 km long spit and infilling of lagoon at Orchid Beach, FI b. Sediment migration over partially vegetated foredune ridges at Orchid Beach, FI c. Sediment migration into and blocking of the Stumers Creek tidal inlet at Coolum Beach, SC.

References

Almonacid-Caballer, J., Sanchez-Garcia, E., Pardo-Pascual, J.E., Balaguer-Beser, A.A., Palomar-Vazquez, J., 2016. Evaluation of annual mean shoreline position deduced from Landsat imagery as a mid-term coastal evolution indicator. Marine Geology, 372, 79-88.

Anders, F.J. and Byrnes, M.R., 1991. Accuracy of shoreline change rates as determined from maps and aerial photographs. Shore and Beach, 59(1), 17–26.

Andrade, F. and Ferriera, M.A., 2006. A simple method of measuring beach profiles. Journal of Coastal Research, 22(4), 995-999.

Barnie, T., Thrastarson, R., Jonsdottir, I., Moussallam, Y., 2018. The cubesat revolution in volcano monitoring – examples from PlanetScope. Proceedings of the 20th EGU General Assembly (Vienna, Austria), pp. 19580.

Bengtsson, L., Hodges, K.I., Roecker, E., 2006. Storm tracks and climate change. Journal of Climate, 19, 3518-3543.

Boak, E. and Turner, I., 2005. Shoreline definition and detection: a review. Journal of Coastal Research, 21(4), 688-703.

Boldt, K.V., Lane, P., Woodruff, J.D., Donnelly, J.P., 2010. Calibrating a sedimentary record of overwash from southeastern New England using modeled hurricane surges. Marine Geology, 275, 127-139.

Boyd, R., Ruming, K., Goodwin, I., Sandstrom, M., Schroder-Adams, C., 2008. Highstand transport of coastal sand to the deep ocean: A case study from Fraser Island, southeast Australia. Geology, 36(1), 15-18.

Bureau of Meteorology (BOM), 2019. http://www.bom.gov.au/.

Cenci, L., Disperati, L., Sousa, L.P., Phillips, M., Alve, F.L., 2013. Geomatics for Integrated Coastal Zone Management: multitemporal shoreline analysis and future regional perspective for the Portuguese Central Region. Journal of Coastal Research, Special Issue No. 65, 1349-1354.

Cisneros, M.A.H., Sarmiento, N.V.R., Delrieux, C.A., Piccolo, M.C., Perillo, G.M.E., 2016. Beach carrying capacity assessment through image processing tools for coastal management. Ocean & Coastal Management, 130, 138-147.

Colomina, I. and Molina, P., 2014. Unmanned aerial systems for photogrammetry and remote sensing: a review. ISPRS Journal of Photogrammetry and Remote Sensing, 92, 79-97.

Cook, D.E., 2019. Butzer 'Down Under': debates on anthropogenic erosion in early colonial Australia. Geomorphology, 331(15), 160-174.

Courier Mail, 2019a. Waves surge over seaside path as Cyclone Oma brings high tides to Queensland. https://www.couriermail.com.au/news/national/waves-surge-over-seaside-footpath-as-cyclone-oma-brings-high-tides-to-queensland/video/06dfbbf6cc37ee4681d8528d69ab2488

Courier Mail, 2019b. Fears Bribie Island may split in two as northern tip eroded. https://www.couriermail.com.au/news/queensland/fears-bribie-island-may-split-in-two-as-northern-tip-eroded/news-story/f29731b0c2f6d33c4aa48c0f1b5161cc

Delgado, I. and Lloyd, G., 2004. A simple low cost method for one person beach profiling. Journal of Coastal Research, 20(4), 1246-1252.

Dolan, R., Hayden, B.P., May, P., May, S.K., 1980. The reliability of shoreline change measurements from aerial photographs. Shore and Beach, 48(4), 22–29.

Dolan, R., Hayden, B.P., May, S., 1983. Erosion of the US shorelines. In: Komar, P.D. (ed.), CRC Handbook of Coastal Processes and Erosion (Boca Raton, Florida), CRC Press, pp. 285–29.

Ellerton, D., Rittenhour, T., Miot da Silva, G., Gontz, A., Shulmeister, J., Hesp, P., Santini, T., Welsh, K., 2018. Late Holocene cliff-top blowout activation and evolution in the Cooloola Sand Mass, southeast Queensland, Australia. The Holocene, 28(11), 1697-1711.

ESA, 2019. S2 MPC L1C Data Quality Report Ref. S2-PDGS-MPC-DQR, Issue: 36. Date: 05/03/2019. https://sentinel.esa.int/documents/247904/685211/Sentinel-2_L1C_Data_Quality_Report

Fellman, J.P., 2008. Visibility mapping in New York's coastal zone: a case study of alternative methods. Coastal Zone Management Journal, 9(3-4), 249-270.

Fisher, J.S. and Stauble, D.K., 1977. Impact of Hurricane Belle on Assateague Island washover. Geology, 5(12), 765-768.

FitzGerald, D.M. and Pendleton, E.P., 2002. Inlet formation and evolution of the sediment bypassing system: New Inlet, Cape Cod, Massachusetts. Journal of Coastal Research, Special Issue No. 36, 290-299.

Forsyth, A.J., Knott, J., Bateman, M.D., 2010. Beach ridge plain evidence of a variable late-Holocene tropical cyclone climate, North Queensland, Australia. Palaeogeography, Palaeoclimatology, Palaeoecology, 297(3-4), 707-716.

Gontz, A.M., Moss, P.T., Wagenknecht, E.K., 2013. Stratigraphic architecture of a regressive strand plain, Flinders Beach, North Stradbroke Island, Queensland, Australia. Journal of Coastal Research, 30(3), 575-585.

Gontz, A.M., Maio, C.V., Wagenknecht, E.K., Berkland, E.P., 2011. Assessing threatened coastal sites: applications of ground penetrating radar and geographic information systems. Journal of Cultural Heritage, 12(4), 451-458.

Gonclaves, J.A. and Henriques, R., 2015. UAV photogrammetry for topographic monitoring of coastal areas. ISPRS Journal of Photogrammetry and Remote Sensing, 104, 101-111.

Hagenaars, G., de Vries, S., Luijendijk, A.P., de Boer, W.P., Reniers, A.J.H.M., 2018. On the accuracy of automated shoreline detection derived from satellite imagery: A case study of the sand motor mega-scale nourishment. Coastal Engineering, 133, 113-125.

Hapke, C.J., Reid, D., Richmond, B.M., Ruggiero, P., List, J., 2006. National Assessment of Shoreline Change: Part 3: Historical Shoreline Changes and Associated Coastal Land Loss along the Sandy Shorelines of the California Coast. U.S. Geological Survey Open-file Report 2006-1219.

Harley, M.D., Turner, I.L., Short, A.D., Ranasinghe, R., 2010. Interannual variability and controls of the Sydney wave climate. International Journal of Climatology, 30(9), 1322-1335.

Harris, P.T., Heap, A.D., Bryce, S.M., Porter-Smith, R., Ryan, D.A., Heggie, D.T., 2002. Classification of Australian Clastic Coastal Depositional Environments Based Upon a Quantitative Analysis of Wave, Tidal, and River Power. Journal of Sedimentary Research, 72(6), 858-870.

Harvey, N. and Smithers, S., 2018. How close to the coast? Incorporating coastal expertise into decision-making on residential development in Australia. Ocean & Coastal Management, 157, 237-247.

Hemer, M.A., Church, J.A., Hunter, J.R., 2007. Waves and climate change on the Australian coast. Journal of Coastal Research, Special Issue No. 50, 432-437.

Hemer, M.A., McInnes, K.L., Ranasinghe, R., 2013. Projections of climate change-driven variations in the offshore wave climate off south eastern Australia. International Journal of Climatology, 33(7), 1615-1632.

Himmelstoss, E.A., 2009. DSAS 4.0—Installation Instructions and User Guide. In: Thieler, ER, Himmelstoss, EA, Zichichi, JL and Ergul, A. Eds., The Digital Shoreline Analysis System (DSAS) Version 4.0—An ArcGIS Extension for Calculating Shoreline Change. US Geological Survey Open-File Report 2008-1278, ver. 4.2. 81.

Houborg, R. and McCabe, M.F., 2018. Daily Retrieval of NDVI and LAI at 3 m Resolution via the Fusion of CubeSat, Landsat, and MODIS Data. Remote Sensing, 10(6), 890.

Hughes, M.G. and Heap, A.D., 2010. National-scale wave energy resource assessment for Australia. Renewable Energy, 35(8), 1783-1791.

IPCC, 2014. Climate Change 2014: Synthesis Report. Contribution of Working Groups I, II and III to the Fifth Assessment Report of the Intergovernmental Panel on Climate Change [Core Writing Team, R.K. Pachauri and L.A. Meyer (eds.)]. IPCC, Geneva, Switzerland, 151p.

Kelly, J.T. and Gontz, A.M., 2018. Using GPS-surveyed intertidal zones to determine the validity of shorelines automatically mapped by Landsat water indices. International Journal of Applied Earth Observation and Geoinformation, 65, 92-104.

Kelly, J.T., McSweeney, S., Shulmesiter, J., Gontz, A.M., Bimodal climate control of shoreline change influenced by Interdecadal Pacific Oscillation variability along the Cooloola Sand Mass, Queensland, Australia. Marine Geology, 415, 105971.

Kirschen, P., Watson, C., Douglas, E., Gontz, A., Lee, J., Tian, Y., 2008. Coastal flooding in the northeastern United States due to climate change. Mitigation and Adaptation for Global Change, 13(5-6), 437-451.

Knott, J., Smithers, S., Walsh, K., Rhodes, E., 2009. Sand beach ridges record 6000 year history of extreme cyclone activity in northeastern Australia. Quaternary Science Reviews, 28(15-16), 1511-1520.

Laska, S., Wooddell, G., Hangleman, R.M., Grammling, R.,Farris, M.T., 2005. At risk: the human community and infrastructure resources of coastal Louisiana. Journal of Coastal Research, Special Issue No. 44, 90-111.

Leatherman, S.P., Williams, A.T., Fisher, J.S., 1977. Overwash sedimentation associated with a large-scale northeaster. Marine Geology, 24(2), 109-121.

Levin, N., 2011. Climate-driven changes in tropical cyclone intensity shape dune activity of the Earth's largest sand island. Geomorphology, 125(1), 239-252.

Levin, N., Neil, D., Syktus, J., 2014. Spatial variability of dune form on Moreton Island, Australia and its correspondence with wind regime derived from observing stations and reanalysis. Aeolian Research, 15, 289-300.

Luijendijk, A., Hagenaars, G., Ranasinghe, R., Baart, F., Donchyts, G., Aarninkhof, S., 2018. The state of the world's beaches. Scientific Reports, 8, 1-11.

Maglione, P., Parente, C., Vallario, A., 2014. Coastline extraction using high resolution WorldView-2 satellite imagery. European Journal of Remote Sensing, 47(1), 685-699.

Maio, C.V., Gontz, A.M., Tenenbaoum, D.E., Berkland, E.P., 2012. Coastal hazard vulnerability assessment of sensitive historical sites on Rainsford Island, Boston Harbor, Massachusetts. Journal of Coastal Research, 28(1A), 20-33.

Maio, C.V., Gontz, A.M., Sullivan, R.M., Madsen, S.M., Weidman, C.R., and Donnelly, J.P., 2014. Subsurface evidence of storm-driven breaching along a transgressing barrier system, Cape Cod, USA. Journal of Coastal Research, 32(2), 264-279.

May, S.M., Brill, D., Leopold, M., Callow, N., Engel, M., Scheffers, A., Opitz, S., Norpoth, M., Bruckner, H., 2017. Chronostratigraphy and geomorphology of washover fans in the Exmouth Gulf (NW Australia) – a record of tropical cyclone activity during the late Holocene. Quaternary Science Reviews, 169, 65-84.

May, S.M., Gelhausen, H., Brill, D., Callow, J.N., Engel, M., Pitz, S., Scheffers, A., Joannes-Boyau, R., Leopold, M., Brukner, H., 2018. Chenier-type ridges in Giralia Bay (Exmouth Gulf, Western Australia) – Process, chronostratigraphy and significance for recording past tropical cyclones. Marine Geology, 396, 186-204.

McSweeney, S. and Shulmeister, J., 2018. Variations in wave climate as a driver of decadal scale shoreline change at the Inskip Peninsula, southeast Queensland, Australia. Estuarine, Coastal, and Shelf Science, 209, 56-69.

MHL, 2012. OEH NSW Tidal Planes Analysis: 1990-2010 Harmonic Analysis. Manly Hydraulics Laboratory, Report MHL2053, 18p.

Miner, M.D., Kulp, M.A., FitzGerald, D.M., Georgiou, I.Y., 2009. Hurricane-associated ebb-tidal delta sediment dynamics. Geology, 37(9), 851-854.

Moore, L.J., 2000. Shoreline mapping techniques. Journal of Coastal Research, 16(1), 111–124.

Moore, L.J., Ruggiero, P., List, J.H., 2006. Comparing mean high water and high water line shorelines: should proxy-datum offsets be incorporated into shoreline change analysis? Journal of Coastal Research, 22(4), 894-905.

Morton, R.A., Gibeaut, J.C., Paine, J.G., 1995. Meso-scale transfer of sand during and after storms: implications for prediction of shoreline movement. Marine Geology, 126(1-4), 161-179.

Morton, R.A., 1991. Accurate shoreline mapping: past, present, and future. Proceedings of the Coastal Sediments ’91 (Seattle, Washington), pp. 997-1010.

Overton, M.F. and Fisher, J.S., 1996. Shoreline analysis using digital photogrammetry. Proceedings of the 25th International Conference on Coastal Engineering (Orlando, Florida), pp. 3750-3761.

Pajak, M.J. and Leatherman, S.P., 2002. The high water line as shoreline indicator. Journal of Coastal Research, 18(2), 329–337.

Pardo-Pascual, J.E., Almonacid-Caballer, J., Ruiz, L.A., Palomar-Vazquez, J., Rodrigo-Alemany, R., 2014. Evaluation of storm impact on sandy beaches of the Gulf of Valencia using Landsat imagery series. Geomorphology, 214, 388-401.

Planet. 2017., Planet Imagery Product Specification. San Francisco, CA: Planet Labs.

Putgatch, T., 2019. Tropical storms and mortality under climate change. World Development, 117, 172-182.

Ranasinghe, R., McLoughlin, R., Short, A., Symonds, G., 2004. The Southern Oscillation Index, wave climate, and beach rotation. Marine Geology, 204(3-4), 273-287.

Roy et al. 2014. Landsat-8: Science and product vision for terrestrial global change research. Remote Sensing of Environment, 145, 154-172.

Ruggiero, P. and List, J.H., 2009. Improving Accuracy and Statistical Reliability of Shoreline Position and Change Rate Estimates. Journal of Coastal Research, 25(5), 1069-1081.

Sekovski, I., Stecchi, F., Mancini, F., Del Rio, L., 2014. Image classification methods applied to shoreline extraction on very high-resolution multispectral imagery. International Journal of Remote Sensing, 35(10), 3556-3578.

Short, A.D., Trembanis, A.C., Turner, I.L., 2000. Beach oscillation, rotation and the Southern Oscillation, Narrabeen Beach, Australia. In: Proceedings of the 27th

International Coastal Engineering Conference. ASCE (Sydney, Australia), pp. 2439-2452.

Smith, A.W.S. and Jackson, L.A., 1992. The variability in width of the visible beach. Shore and Beach, 60(2), 7-14.

Stockdon, H.F., Holman, R.A., Howd, P.A., Sallenger Jr., A.H., 2006. Empirical parameterization of setup, swash, and runup. Coastal Engineering, 53(7), 573-588.

Tejan-Kella, M.S., Chittleborough, D.J., Fitzpatrick, R.W., Thompson, C.H., Prescott, J.R., Hutton, J.T., 1990. Thermoluminescence dating of coastal sand dunes at Cooloola and North Stradbroke Island, Australia. Australian Journal of Soil Research, 28(4), 465-481.

Thieler, E.R. and Danforth, W.W., 1994. Historical shoreline mapping (I): improving techniques and reducing positioning errors. Journal of Coastal Research, 10(3), 549–563.

Thieler, E.R., Himmelstoss, E.A., Zichichi, J.L., Ergul, A., 2017. Digital Shoreline Analysis System (DSAS) version 4.0 - An ArcGIS extension for calculating shoreline change (ver. 4.4, July 2017), U.S Geological Survey Open-File Report 2008-1278.

Thompson, C., 1983. Development and weathering of large parabolic dune systems along the subtropical coast of eastern Australia. Zeitschrift fur Geomorphologie, Supplementband 45, 205–225.

Van der Werff, H.M.A., 2019. Mapping shoreline indicators on a sandy beach with supervised edge detection of soil moisture differences. International Journal of Applied Earth Observation and Geoinformation, 74, 231-238.

Vousdoukas, M.I., Velegrakis, A.F., Dimou, K., Zervakis, V., Conley, D.C., 2009. Wave run-up observations in microtidal, sediment-starved pocket beaches of the Eastern Mediterranean. Journal of Marine Systems, 78, S37-S47.

Walker, J., Lees, B., Olley, J., Thompson, C., 2018. Dating the Cooloola coastal dunes of South-Eastern Queensland, Australia. Marine Geology, 398, 73-85.

Wasantha, P. and Ranjith, P., 2014. Water-weakening behavior of Hawkesbury sandstone in brittle regime. Engineering Geology, 178, 91-101.

Williams, H.F.L., 2015. Contrasting styles of Hurricane Irene washover sedimentation on three east coast barrier islands: Cape Lookout, North Carolina, Assateague Island, Virginia, and Fire Island, New York. Geomorphology, 231, 182-192.

Xu, N., 2018. Detecting coastline change with all available Landsat data over 1986-2015: a case study for the state of Texas, USA. Atmosphere, 9(3), 107.

Yue, Y., Yu, K., Tao, S., Zhang, H., Liu, G., Wang, N., Jiang, W., Fan, T., Lin,W., Wang, Y., 2019. 3500-year western Pacific storm records warns of additional storm activity in a warm pool. Palaeogeography, Palaeoclimatology, Palaeoecology, 521, 57-71.

Zajic, B.N., Simmon, R., Mascaro, J., Kington, J.D., Jordahl, K.A., 2018. How Access to Daily Medium-Resolution Satellite Imagery Can Aid the Global Disaster Response Community. Presented at the American Geophysical Union Annual Meeting, 2018 Dec, Washington, D.C.

Zhang, K., Douglas, B.C., Leatherman, S.P., 2004. Global warming and coastal erosion. Climate Change, 64, 41-58.

Zhang, K., Huang, W., Douglas, B.C., Leatherman, S.P., 2002. Shoreline position variability and long-term trend analysis. Shore and Beach, 70(2), 31–35.

Zhang, K., Whitman, D., Leatherman, S., Robertson, W., 2005. Quantification of Beach Changes Caused by Hurricane Floyd Along Florida's Atlantic Coast Using Airborne Laser Surveys. Journal of Coastal Research, 21(1), 123-134.

Chapter 5

Summary

The spectral water indices using optimal thresholds determined by Fisher et al. (2016) mapped complete shoreline segments for five of the seven indices. TCW and $AWEI_{nsh}$ struggled to discriminate the shoreline boundary in mixed cloud pixel regions. In addition, only one index utilizing their threshold produced satisfactory results ($AWEI_{sh}$). MNDWI and NDVI both used a zero threshold value as suggested by their original authors with only MNDWI achieving accurate results. Jenks-Caspall classification improved the accuracy results of TCW and $AWEI_{nsh}$ by 17.5 and 37.5%. These mixed results point to underlying complication with spectral index classifications in that the threshold values optimized for use in a certain area may not be suitable at other locations. This could be due to a number of parameters such as variable water and land surface conditions, cloud coverage, among others. As such, an index that requires threshold calibration produce accurate results for every unique study area defeats the purpose of having a supposed "repeatable" method to be used globally. Therefore, MNDWI is the most suitable index for mapping Landsat-derived shorelines based on its superior accuracy (88.4%) and stable, repeatable threshold value (0).

Based on the previous results, MNDWI was used on a stack of Landsat 5, 7, and 8 images to derive a high temporal resolution shoreline change curve along the Cooloola Sand Mass in southeast Queensland, Australia. The 21 year horizontal shoreline position record was cross-correlated with climate index data for climate phenomena operating in the Australian region. Cross-correlations were split into two datasets corresponding to IPO

phase as determined by TPI data. During Negative IPO phases, ENSO is the strongest correlated index with a 2 month time lag, agreeing with previous studies that have suggested ENSO has a strong control on Australian wave and atmospheric climate during negative IPO phases. During the more recent positive IPO phase, STR-P and STR-L show the only significant correlation to the shoreline change curves at a 4 month time lag with ENSO showing no correlation at all. The relationships established in this study allow for prediction of future shoreline behavior based on global climate model outputs. Positive IPO is expected to remain for at least 8 more years and changes in the Subtropical Ridge will drive shoreline erosion and growth throughout SE Australia. Over the next century, the frequency and intensity of La Niña events are expected to increase, which will likely promote amplified erosion along SE Australia during negative IPO phases. The Subtropical Ridge is predicted to continue to migrate poleward under global warming scenarios, which will amplify erosion along SW-NE aligned coasts during positive IPO phases.

Revolutionary PlanetScope imagery was used here for the first time to map high water line shoreline positions for the purpose of assessing changes induced by Tropical Cyclone Oma, which struck SE Queensland in February 2019. Similar spatial patterns of progradation at the northern and erosion at the southern ends of the three distinct shoreline compartments was observed. This geomorphic change was likely a response to a rapid and significant clockwise wave rotation, which shifted the local mean direction of longshore transport to the north. The clockwise beach rotation observed along Fraser Island and the Cooloola Sand Mass is a known occurrence along many of New South Wales' and

Queensland's pocket beaches, except it's occurring at a timescale of days as opposed to years due to the storm wave climate. In addition, the total positional uncertainty of shorelines mapped using PlanetScope imagery was assessed using the proxy-offset bias technique. The total positional uncertainty was determined to be primarily due to the geometric accuracy of the PlanetScope data (10 m RMS) and secondarily due to the proxy-offset bias, or the horizontal error due to wave runup. Future studies using PlanetScope data to assess shoreline change should attempt to use imagery acquired at mid-to-low tide to minimize the proxy-offset bias and total uncertainty. This study shows that PlanetScope is a remarkably useful tool for providing rapid response surveys of storm damaged shorelines, particularly those that are inaccessible due to infrastructure damage.

Appendix

Data Sources

Chapter 2:

Landsat Surface Reflectance products were provided by the United States Geological Survey at earthexplorer.usgs.gov.

Chapter 3:

Landsat Surface Reflectance products were provided by the United States Geological Survey at earthexplorer.usgs.gov and earthengine.google.com.

Southern Oscillation Index data were acquired from NOAA at ncdc.noaa.gov/teleconnections/enso/indicators/soi/

Southern Annular Mode data were provided by NOAA at cpc.ncep.noaa.gov/products/precip/CWlink/daily_ao_index/aao/aao.shtml

NCEP/NCAR Reanalysis Monthly Mean Sea Level Pressure data were provided by NOAA at esrl.noaa.gov/psd/data/gridded/data.ncep.reanalysis

Tripole Index for the Interdecadal Pacific Oscillation data were provided by NOAA at esrl.noaa.gov/psd/data/timeseries/IPOTPI/

Pacific Decadal Oscillation data were provided by NOAA at esrl.noaa.gov/psd/gcos_wgsp/Timeseries/PDO/

Chapter 4:

PlanetScope image products were provided by Planet Labs, Inc. through their Education and Research program at planet.com/explorer

Wave and tide data were provided by the State of Queensland at qld.gov.au/waves

LiDAR data were provided by the New South Wales Government at elevation.fsdf.org.au

Google Earth Engine Script (Chapter 3)

```
var geometry = /* color: #0b4a8b */geometry;

// Define an example collection.
var collection = ee.ImageCollection('LANDSAT/LC08/C01/T1_SR')
                .filter(ee.Filter.eq('WRS_PATH', 89))
                .filter(ee.Filter.eq('WRS_ROW', 78))
                .filterDate('2015-01-01', '2015-12-31');

// Calculate MNDWI.
var calculateMNDWI = function(image) {
  // get a string representation of the date.
  var dateString = ee.Date(image.get('system:time_start')).format('yyyy-MM-dd');
  var mndwi = image.normalizedDifference(['B3', 'B6']);
  var area = mndwi.clip(geometry);
  return area.rename(dateString);
};
var MNDWIcollection = collection.map(calculateMNDWI);
print(MNDWIcollection)

var ExportCol = function(col, folder, scale, type,
                         nimg, maxPixels, region) {
    type = type || "float";
    nimg = nimg || 500;
    scale = scale || 1000;
    maxPixels = maxPixels || 1e10;

    var colList = col.toList(nimg);
    var n = colList.size().getInfo();

    for (var i = 0; i < n; i++) {
      var img = ee.Image(colList.get(i));
      var id = img.id().getInfo();
      region = region || img.geometry().bounds().getInfo()["coordinates"];

      var imgtype = {"float":img.toFloat(),
                     "byte":img.toByte(),
                     "int":img.toInt(),
                     "double":img.toDouble()
                    }

      Export.image.toDrive({
        image:imgtype[type],
        description: id,
        folder: folder,
        fileNamePrefix: id,
```

```
      region: region,
      scale: scale,
      maxPixels: maxPixels})
  }
 }
var col = MNDWIcollection
ExportCol(col, "GEE", 30);
```